

Investigation of perovskite-CIGSe tandem solar cells

vorgelegt von
Dipl.-Ing.
Yajie Wang
ORCID: 0000-0002-1771-7222

von der Fakultät IV Elektrotechnik und Informatik
Institut für Hochfrequenz- und Halbleiter-Systemtechnologien
der Technischen Universität Berlin
zur Erlangung des akademischen Grades

Doktor der Ingenieurwissenschaften
- Dr.-Ing. –

genehmigte Dissertation

Promotionsausschuss:

Vorsitzender: Prof. Dr. Steve Albrecht
Gutachter: Prof. Dr. rer. nat. Bernd Szyszka
Gutachter: Prof. Dr. Rutger Schlatmann
Gutachter: Prof. Dr. Bart Vermang

Tag der wissenschaftlichen Aussprache: 15. Mai 2019

Berlin 2019

Technische Universität Berlin

Fakultät IV Elektrotechnik und Informatik

Institut für Hochfrequenz- und Halbleiter-Systemtechnologien



Dissertation

Investigation of perovskite-CIGSe tandem solar cells

Yajie Wang

Supervised by

Prof. Dr. rer. nat. Bernd Szyszka

Prof. Dr. Rutger Schlatmann

2019

Contents

| | |
|---|-----------|
| Abstract | 9 |
| Kurzfassung | 11 |
| 1 Introduction | 13 |
| 1.1 Photovoltaics..... | 13 |
| 1.1.1 The status of photovoltaics | 13 |
| 1.1.2 Solar cell basics..... | 13 |
| 1.1.3 Tandem solar cells | 14 |
| 1.2 Bottom cell: Cu(In, Ga)Se ₂ thin film solar cells..... | 16 |
| 1.2.1 Basic structure | 16 |
| 1.2.2 Fabrication process..... | 17 |
| 1.2.3 Electronic properties | 19 |
| 1.3 Top cell: perovskite solar cells | 19 |
| 1.3.1 Basic structure | 20 |
| 1.3.2 Fabrication process..... | 21 |
| 1.3.3 Electronic properties | 22 |
| 1.4 Perovskite-CIGSe tandem solar cells..... | 23 |
| 1.4.1 Design of monolithic perovskite-CIGSe tandem solar cells..... | 23 |
| 1.4.2 Band alignment..... | 24 |
| 1.4.3 Current matching and optical management | 26 |
| 1.5 p-type semiconductor as part of the recombination junction..... | 27 |
| 1.5.1 Requirements for the intermediate layer | 27 |
| 1.5.2 Promising candidates..... | 28 |
| 1.6 Objectives and outline | 28 |
| 2 Experimental section | 31 |
| 2.1 Sample preparation..... | 31 |
| 2.1.1 Spin coating | 31 |
| 2.1.2 Sputtering | 32 |
| 2.2 Analytical methods..... | 34 |
| 2.2.1 XPS characterization | 35 |

| | | |
|----------|---|-----------|
| 2.2.2 | UPS characterization..... | 36 |
| 2.3 | The CISSY system..... | 37 |
| 2.4 | Simulation methods | 38 |
| 3 | Low band-gap CuIn(S, Se)₂ absorber deposition using molecular ink..... | 41 |
| 3.1 | Background | 41 |
| 3.2 | Results and discussion..... | 42 |
| 3.2.1 | EGBE solvent variation..... | 42 |
| 3.2.2 | Absorber thickness variation | 44 |
| 3.2.3 | Annealing treatment | 46 |
| 3.2.4 | The effect of Na in the precursor solution | 48 |
| 3.2.5 | Champion cell | 50 |
| 3.3 | Summary and outlook..... | 51 |
| 4 | P-type Cu₂O as an intermediate transparent conducting layer for monolithic perovskite-CIGSe tandem solar cells..... | 53 |
| 4.1 | Background | 53 |
| 4.2 | Results and discussion..... | 55 |
| 4.2.1 | Sputtering method with oxygen variation..... | 55 |
| 4.2.2 | Sputtering of nitrogen doped Cu ₂ O..... | 57 |
| 4.2.3 | Wet chemical deposition of Cu ₂ O..... | 61 |
| 4.2.4 | PVK cells..... | 63 |
| 4.3 | Summary and outlook..... | 65 |
| 5 | P-type CuGaO₂ as an intermediate transparent conducting layer for monolithic perovskite-CIGSe tandem solar cells..... | 67 |
| 5.1 | Background | 67 |
| 5.2 | Results and discussion..... | 69 |
| 5.2.1 | Sputtering method | 69 |
| 5.2.2 | Sputtering with additional oxygen supply..... | 72 |
| 5.2.3 | Sputtering with varied distance..... | 74 |
| 5.2.4 | Sodium doping..... | 76 |
| 5.3 | Summary and outlook..... | 78 |

| | | |
|----------|--|-----|
| 6 | Optical and electrical simulations for monolithic perovskite-CIGSe tandem solar cells | |
| | | 79 |
| 6.1 | Background | 79 |
| 6.2 | Results and discussion..... | 80 |
| 6.2.1 | Optical simulation..... | 80 |
| 6.2.2 | Electrical simulation | 83 |
| 6.3 | Summary and outlook..... | 85 |
| 7 | Summary | 87 |
| 8 | Outlook | 91 |
| 9 | Appendix | 93 |
| | List of Acronyms | 101 |
| | Reference | 105 |
| | List of publications..... | 123 |
| | Acknowledgements | 125 |

Abstract

Multi-junction photovoltaic devices have received much attention for a long time due to their potential performance beyond the Shockley-Queisser (S-Q) limit compared with the current (commercially available) single junction solar cells. Thin film solar cells based on polycrystalline $\text{Cu}(\text{In,Ga})(\text{S,Se})_2$ (CIGSe) absorbers and hybrid organic-inorganic perovskite solar cells have reached power conversion efficiencies over 22%. Therefore, combining these technologies to overcome the S-Q limit by constructing a completely thin-film perovskite-CIGSe tandem solar cells is a promising approach. However, to construct a monolithic perovskite-CIGSe tandem device is complicated and needs a sophisticated design, especially the compatibility between the top cell and the bottom cell, the choice of the intermediate layer, the specific fabrication process. Therefore, many critical questions about the monolithic perovskite-CIGSe tandem solar cells need to be discussed and solved.

First, in order to achieve the highest tandem efficiency, the band gaps of top cell and bottom cell should be adjusted in a way that the top semiconductor material or active layer absorbs the higher energy incident light and the bottom absorbs the remaining light. In principle, a tandem device consists of a bottom cell with a lower band gap and a top cell with a higher band gap. To fabricate a CIGSe solar cell with low band gap by a simple approach is the first task which needs to be investigated. Vacuum free and solution process based routes to the preparation of chalcopyrite absorbers for solar cells provide options in device design and manufacturing that are not available by the standard vacuum based approaches. Therefore, a non-vacuum, simple solution coating approach for $\text{CuIn}(\text{S,Se})_2$ thin film preparation was chosen. It is based on spin coating of an air stable molecular ink, containing metal chlorides and thiourea in organic solvents, and it was used to prepare low band gap bottom cells. Several key parameters directly influencing the performance of the solar cells were identified. Eventually, these optimizations aimed at high photo current led to an efficiency of 9.5% with a low band gap of 1.02 eV.

Secondly, looking for a suitable p-type intermediate layer for the monolithic perovskite-CIGSe tandem solar cells is also a key factor for obtaining working tandem devices with high efficiency. In order to fabricate an efficient tandem solar cell, this intermediate layer should meet some requirements, such as transparency, good conductivity, stability, low-temperature preparation, and suitable valence and conduction band positions. Cuprous oxide (Cu_2O) and copper gallium oxide (CuGaO_2) can be deposited at room temperature with high transparency and an appropriate band structure compatible with the perovskite layer. A Cu_2O film prepared by a wet chemical approach was applied to the single junction perovskite solar cells and achieved over 9% photoconversion efficiency. CuGaO_2 as a p-type semiconductor was prepared at room temperature by sputtering to be the hole conductor in the top perovskite cell and one of components of the intermediate tunnel junction. Several parameters were adjusted to optimize the band structure of CuGaO_2 films to make them compatible with the perovskite layer. The resulting properties of Cu_2O and

CuGaO₂ films indicated that they are suitable materials as hole conductors and could qualify as one of the components of the intermediate tunnel junction of monolithic perovskite-CIGSe tandem solar cells.

Thirdly, in order to predict the photovoltaic performance and analyze the recombination losses of monolithic tandem solar cells, a model of a monolithic perovskite-CIGSe tandem solar cell based on Cu₂O and CuGaO₂ as intermediate layers was used for optical and electrical simulations. From the optical simulation and a series of calculations of the equivalent electrical circuit of the monolithic tandem solar cells, the highest matched current of 20.8 mA/cm² was calculated using a CuGaO₂-based perovskite-CIGSe tandem device. A modeled power conversion efficiency of 30.3%, a V_{oc} of 1.75 V and a fill factor of 0.83 were obtained.

Kurzfassung

Tandemsolarzellen, d.h. photovoltaische Bauelemente mit mehreren p-n-Übergängen haben das Potential, Wirkungsgrade zu erreichen, die über der so genannten Schockley-Queisser (S-Q)-Grenze für Einzelsolarzellen liegen. Sie sind daher seit längerem Gegenstand intensiver Forschung. Dünnschichtsolarzellen auf der Basis von polykristallinen Cu(In,Ga)(S,Se)_2 (CIGSe) -Absorbern und hybriden organisch-anorganischen Perowskit-Solarzellen haben Wirkungsgrade von über 22% erreicht. Die Kombination dieser Technologien eröffnet die vielversprechende Möglichkeit, die S-Q-Grenze durch die Entwicklung von Perowskit-CIGSe-Tandemsolarzellen zu übertreffen. Die Konstruktion eines monolithischen Perowskit-CIGSe-Tandembaulements ist jedoch kompliziert und erfordert ein ausgeklügeltes Design, um insbesondere die Kompatibilität zwischen der oberen Zelle und der unteren Zelle zu gewährleisten. Daneben müssen die Fragen nach einer geeigneten Rekombinationschicht und dem spezifischen Herstellungsprozess diskutiert und gelöst werden.

Um die höchste Tandemeffizienz zu erzielen, sollten zuerst die Bandlücken der oberen, dem Licht zugewandten Zelle und der unteren Zelle unter Berücksichtigung des oberen Halbleitermaterials so gewählt werden, dass in der oberen Zelle das kurzwellige und in der unteren das langwellige Licht absorbiert wird. Daher besteht ein photovoltaisches Tandem-Bauelement aus einer unteren Zelle mit einer kleineren Bandlücke und einer oberen Zelle mit einer größeren Bandlücke. Die Herstellung und Optimierung einer CIGSe-Solarzelle mit kleiner Bandlücke ist die erste zu lösende Aufgabe. Vakuumfreie und nasschemische Ansätze zur Herstellung von Chalkopyrit-Absorbern für Solarzellen bieten Optionen bei der Gerätekonstruktion und -herstellung, die mit den herkömmlichen vakuumbasierten Ansätzen nicht möglich sind. Daher wurde ein einfaches Verfahren für die CuIn(S,Se)_2 -Dünnschichtherstellung entwickelt. Dabei wird eine luftstabile Tinte, die Metallchloride und Thioharnstoff in organischen Lösungsmitteln enthält, in einer Rotationsbeschichtungsanlage definiert auf geeignete Substrate aufgeschleudert. Mehrere Schlüsselparameter, die die Leistungsfähigkeit der Solarzellen direkt beeinflussen, wurden identifiziert. Letztendlich führten diese Optimierungen, die auf hohe Photoströme abzielten, zu einem Material mit einer niedrigen Bandlücke von 1,02 eV bei einem Solarzellenwirkungsgrad von 9.5%.

Zweitens ist die Suche nach einem geeigneten ladungsträgerselektiven, p- dotierten Material zum Einsatz als Zwischenschicht zwischen unterer und oberer Teilzelle für die monolithischen Perowskit-CIGSe-Tandems auch ein Schlüsselfaktor. Um eine effiziente Tandemsolarzelle herzustellen, sollte diese Zwischenschicht einige Anforderungen erfüllen: Transparenz für langwelliges Licht, gute Leitfähigkeit, chemische Stabilität, die Möglichkeit zur Präparation bei niedrigen Temperaturen und geeignete Bandlagen. Die Zwischenschicht dient einerseits als Lochleiter in der oberen Perowskit-Zelle, sollte aber andererseits auch eine der Komponenten des Rekombinationsübergangs zwischen den beiden Teilzellen sein. Kupfer-(I)-oxid (Cu_2O)

und Kupfer-Galliumoxid (CuGaO_2) können bei Raumtemperatur mit hoher Transparenz und einer geeigneten Bandstruktur, die mit dem Perowskit-Material kompatibel ist, abgeschieden werden. Ein mit einem nasschemischen Ansatz hergestelltes Cu_2O wurde in Perowskit-Einzelsolarzellen mit verwendet und erzielte einen Wirkungsgrad von über 9%. p-CuGaO_2 wurde bei Raumtemperatur durch Sputtern hergestellt. Mehrere Parameter wurden angepasst, um die Bandstruktur von CuGaO_2 -Filmen zu optimieren, um sie mit der Perowskitschicht kompatibel zu machen. Die resultierenden Ergebnisse von Cu_2O - und CuGaO_2 -Filmen zeigten, dass sie geeignete Materialien als Lochleiter und als Komponente des intermediären Rekombinations/Tunnelübergangs monolithischer Perowskit-CIGSe-Tandemsolarzellen sein können.

Drittens wurde ein Modell einer monolithischen Perowskit-CIGSe-Tandemsolarzelle mit jeweils Cu_2O und CuGaO_2 als Zwischenschichten entwickelt, um optische und elektrische Simulationen durchzuführen. Damit konnten die photovoltaische Leistung vorhergesagt und Rekombinationsverluste in monolithischen Tandemsolarzellen analysiert werden. Durch optische Simulation einer CuGaO_2 -basierten Perowskit-CIGSe-Tandemsolarzelle unter Annahme eines bestimmten Ersatzschaltbildes wurde eine maximale angepasste Stromdichte von $20,8 \text{ mA/cm}^2$ ermittelt. Dabei wurde ein Wirkungsgrad von 30,3% mit einer Leerlaufspannung von 1,75 V und einem Füllfaktor von 0,83 errechnet.

1 Introduction

1.1 Photovoltaics

1.1.1 The status of photovoltaics

Since the beginning of the 21st century, global-scale energy and environmental issues have become increasingly prominent [1]. Solar energy has the advantages of inexhaustible and clean energy, thus it is an effective solution to the energy shortages, environmental pollution and the greenhouse effect [2]. Photovoltaic devices demonstrate that they are promising for the commercial market as the portable renewable-energy conversion technology, which is a direct conversion of sunlight into electricity without any heat engine to interfere [3, 4].

Today, the photovoltaic market is dominated by crystalline silicon solar cells (Si) in its multi-crystalline and monocrystalline forms. So far, the crystalline silicon solar cells have achieved beyond 25% efficiency [5, 6]. Cu(In,Ga)(S, Se)₂ (CIGSe) as one of the most competitive thin film solar cells has achieved a conversion efficiency up to 23.35% [7]. Additionally, perovskite solar cells (PVK) have recently emerged, showing rapid development and opening new directions in the photovoltaics field. The record efficiency of PVK devices is now beyond 22% [8].

1.1.2 Solar cell basics

The conversion of solar radiation into electricity by the photovoltaic effect was first observed by Becquerel [9]. Generally, solar cells are defined as systems that convert sunlight into electric energy [10]. In practice, most photovoltaic devices consist of one or several semiconductor p-n junctions. Figure 1.1 shows a typical solar cell structure, consisting of a base, an emitter, an anti-reflection layer and contacts. The base semiconductor is able to absorb the sunlight. The absorption region of the solar spectrum is dependent on the properties of the semiconductor, such as band gap. The electron-hole pairs are generated when the absorption occurs. As shown in figure 1.2, upon formation of the junction between an n-doped and a p-doped semiconductor, electrons from the n region near the p-n interface will diffuse into the p region and will recombine with holes, leaving behind positively charged ions in the n region. Likewise, holes from the p-type region begin to diffuse into the n region, leaving behind negatively charged ions in the p region and recombining with electrons. This diffusion process creates the space charge region near the p-n interface, resulting in an electric field. On the one hand, the diffusion process forces electrons to the p region and holes to the n region. On the other hand, the resulting electric field tends to counteract the diffusion. These two concurrent phenomena tend to establish an equilibrium. When light of sufficient energy is absorbed by the base material, electrons are excited from the valence band to the conduction band of

the semiconductor. Depending on their lifetime they can diffuse in the material until they reach the junction. The electric field in the space charge region separates electrons and holes, and they are collected at the thin emitter layer and the back contact, respectively, leading to a voltage difference over the solar cell [11, 12].

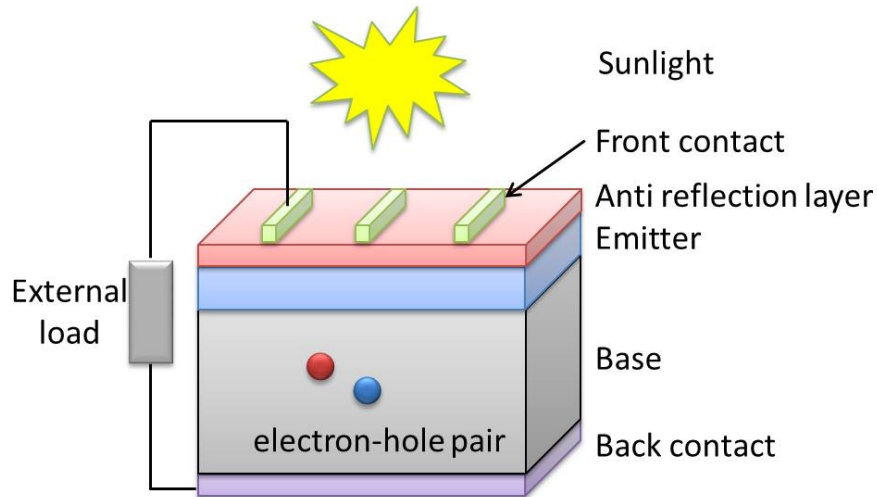


Figure 1.1 Typical solar cell structure.

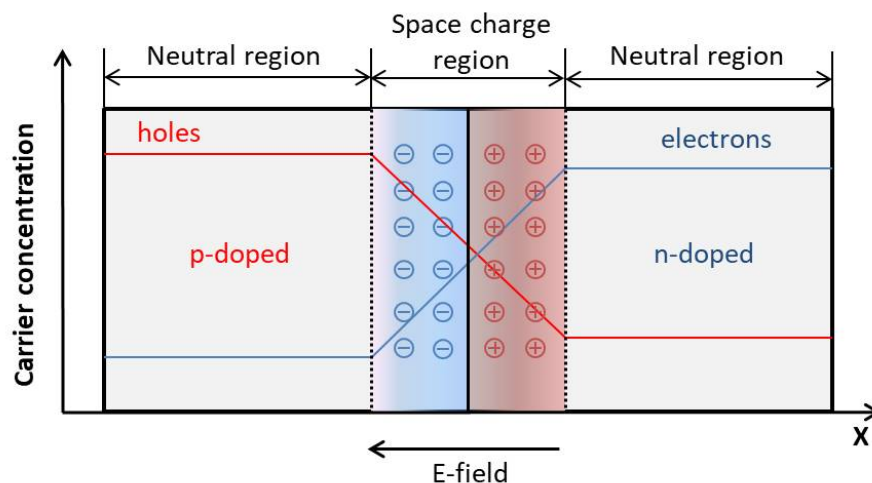


Figure 1.2 A p-n junction in thermal equilibrium with zero-bias voltage applied.

1.1.3 Tandem solar cells

The fundamental efficiency of a single junction semiconductor material is limited by many factors. Theoretically, photons with energies below the band gap are not absorbed, while photons with energies above the band gap are not fully converted to electrical energy due to the thermalization of charge carriers [13]. Even in an ideal structure, the open circuit voltage (V_{oc}) is always lower than the band gap of the material due to the thermodynamic balance between the device and the environment, leading to emission losses from the device. Additionally, carrier recombination occurs in the semiconductor, which also reduces the efficiency.

Therefore, for a single junction solar cell, there is a maximum power conversion efficiency. According to calculations by Shockley and Queisser in 1961 (S-Q) a maximum of 33.7% efficiency for a band-gap of 1.34 eV by taking all these factors into account, was calculated [14].

In order to overcome the theoretical S-Q limitation, De Vos investigated the tandem solar cell model by taking solar irradiation and also the irradiation by the electroluminescence of the individual cells of the device into account [15]. In the multi-junction devices, higher-energy photons are absorbed by the top cell with higher band gap, while lower-energy photons pass through the high band gap top cell and are absorbed by the lower band gap bottom cell. Hence, tandem solar cells exhibit a higher efficiency than single junction solar cells by extending the usable range of the solar spectrum and reducing spectral losses [16, 17]. Two sub-cells tandem devices can achieve a power conversion efficiency of 42%, those with three sub-cells even 49%, which outperforms single junction solar cells that only reach around 30% efficiency due to the S-Q limit.

Tandem solar cells devices with two sub-cells can be configured in two different ways: as four-terminal or two-terminal devices as shown in figure 1.3. Four-terminal tandem solar cells consist of independent top and bottom cells which retain their own anode and cathode, which are connected electrically through an external circuit. Two terminal or monolithic tandem solar cells have one common anode and cathode and the entire tandem device is deposited layer by layer as a monolithic stack [18]. Since a monolithic tandem solar cell requires fewer electrodes, less auxiliary circuitry, and fewer interconnects such as transparent conducting layers and electric wires, in principle, it can be manufactured with lower costs, maintaining the high photovoltaic performance [19].

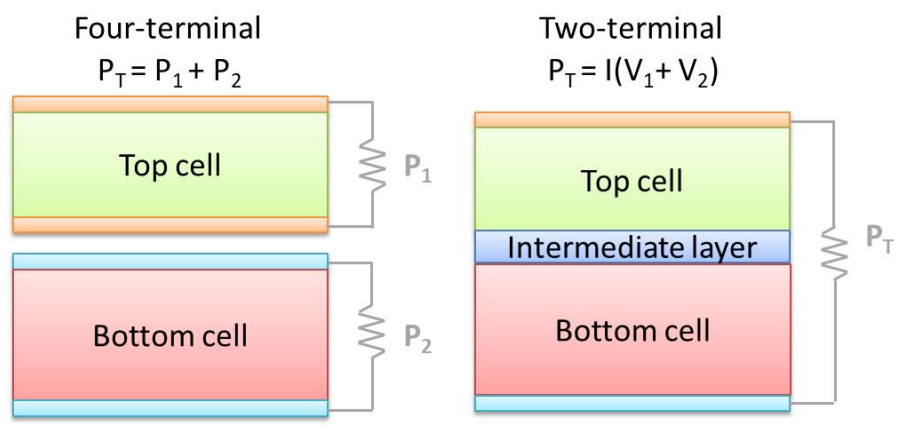


Figure 1.3 Four-terminal tandem with independent electrical connection and two-terminal series-connected tandem.

Therefore, many attempts were directed towards developing low-cost, integrated two-terminal tandem solar cells for pushing the photoconversion efficiency to higher values [15, 20, 21]. Among them, monolithic perovskite-CIGSe tandem solar cells are promising because of the low cost of the chalcopyrite CIGSe thin film and their

tunable band gap. A detailed introduction to perovskite-CIGSe tandem solar cells will be given in the next section.

1.2 Bottom cell: Cu(In, Ga)Se₂ thin film solar cells

Copper indium gallium selenide (CIGSe) based thin film solar cells have drawn worldwide attention for many years due to their high efficiency, which is comparable to Si wafer based solar cells. In general, CIGSe solar cells are fabricated by a high temperature deposition process. By changing the Ga-to-In ratio, the bandgap of the absorber can be adjusted, and the CIGSe film stoichiometry needs to be precisely controlled to achieve the maximum efficiency. The optimal bandgap gradient in chalcopyrite solar cells can be achieved by controlled incorporation of Ga or S. Although CIGSe has many advantages in the solar power generation, such as adjustable stoichiometry and high efficiency, low-production cost, high reproducibility, high-throughput and process tolerance, the complexity of the deposition process has slowed down its development and lags behind that of cadmium telluride (CdTe) based solar cells [22]. In order to make CIGSe based solar cells superior to c-Si and CdTe solar cells in the industrial production, more efforts are needed. Making multi-junction photovoltaic devices is one option to overcome the S-Q theoretical efficiency limitation. In the chalcopyrite Cu(In, Ga, Al)(S, Se)₂ alloy system, the band gap can be varied from 1.04 eV (CuInSe₂) to about 3.5 eV (CuAlS₂) [22]. The two junction tandem with the maximum theoretical efficiency would need a top cell with a bandgap of 1.63 eV and a bottom cell with a bandgap of 0.96 eV [23, 24]. Therefore, a CIGSe based solar cell is an appropriate choice as the bottom cell of a tandem device due to its tunable bandgap and low-cost deposition.

1.2.1 Basic structure

The schematic diagram of the CIGSe based solar cell structure is shown in figure 1.4, consisting of soda-lime glass as substrate, molybdenum as back contact, p-type CIGSe film as absorber, n-type CdS as buffer layer, intrinsic ZnO (i-ZnO) and Al doped ZnO (AZO) as windows layers. The CIGSe absorber film with a thickness of typically 1-3 μm is deposited on the Mo-coated glass substrate. The p-n junction is formed at the interface between the CIGSe layer and a CdS layer with a thickness of 40-80 nm. 100 nm thick i-ZnO and 300 nm thick AZO as window layers are deposited on top of the CdS buffer layer [3].

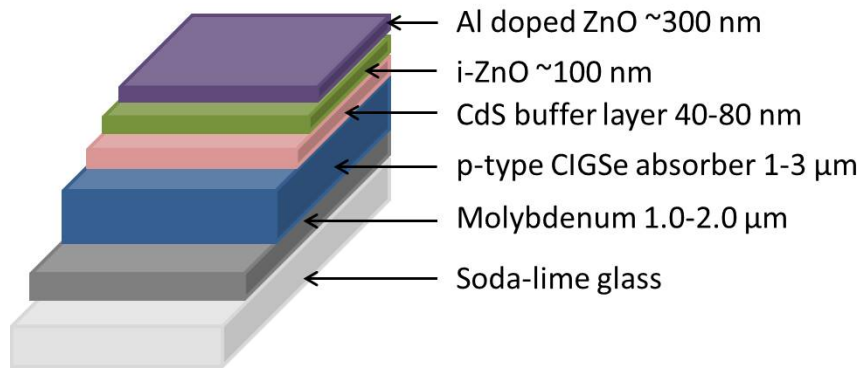


Figure 1.4 Schematic cross-section of CIGSe based thin film solar cell.

When the incident light enters the cell through the transparent ZnO window, the n-type CdS buffer layer with a bandgap of 2.4 eV transmits light up to 2.4 eV to the CIGSe absorber ($E_g \sim 1.2$ eV), where electron-hole pairs are mainly generated. The photons with higher energy are absorbed by the buffer layer. Since they do not contribute to the photocurrent of the device, the CdS layer is usually kept as thin as possible. As shown in figure 1.5, electron-hole pairs are generated in the absorber layer. According to the description in the section 1.1.2 [11, 12, 25], the charge carrier recombination occurs with a high possibility in the space charge region (SCR) next to the p-n junction interface. Electrons generated from the p-type absorber diffuse to the n-type buffer layer and are collected by the n-type front electrode. Simultaneously, holes diffuse inside the p-type layer and are collected by the p-type back electrode [26].

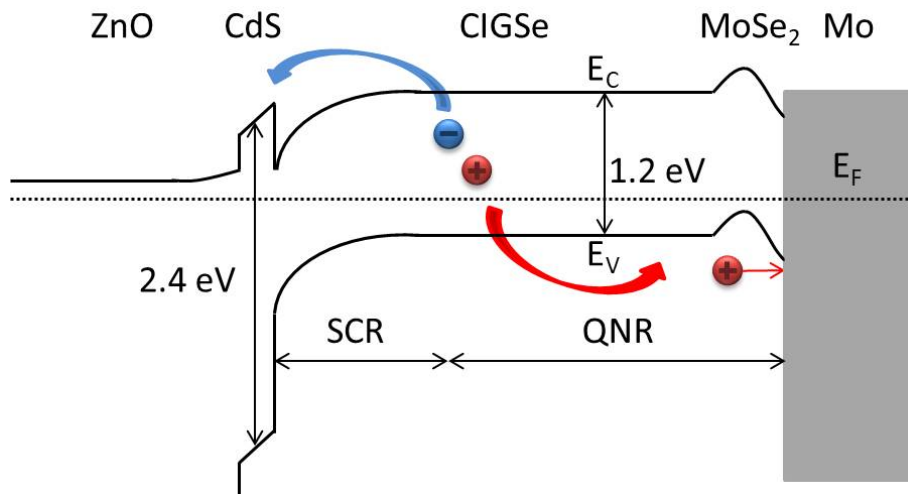


Figure 1.5 Schematic band profile of a typical CIGSe solar cell under zero-bias voltage.

1.2.2 Fabrication process

The fabrication process of the CIGSe based thin film solar cells consists of several steps: a molybdenum layer is deposited by sputtering on the soda-lime glass substrate, the CIGSe absorber layer can be prepared by different methods, a

chemical bath deposition (CBD) process is used to deposit the CdS buffer layer, and window layers are prepared by a sputtering method.

For the CIGSe absorber, the deposition methods for lab-scale and industrial-scale production can be divided into three categories: (a) co-evaporation, (b) sequential selenization/sulfurization of the precursor metal films, and (c) non-vacuum techniques by printing suitable inks on a substrate and subsequent annealing. Each of them has its advantages. The selection among different deposition methods can be dependent on the objective of the CIGSe solar cells production, for lab-scale or industrial-scale. For the lab-scale, precisely controlling the CIGSe film composition to reach high efficiency is one of the first considerations. However, for the industrial-scale, compared to the efficiency, production cost, output capacity and reproducibility are also very important. Table 1.1 shows a short summary of various preparation methods for CIGSe absorber films, and their advantages and disadvantages.

The co-evaporation process for making CIGSe films is applied mainly in research and development because the elemental composition can be precisely controlled during a multi-stage deposition process [27]. During the multi-stage deposition process, the individual elements are deposited under vacuum at different deposition rates and temperatures to form high quality thin films [28, 29]. The big advantage of the co-evaporation process is that the Cu-poor absorber ($Cu/(In+Ga) < 1$) can be prepared more easily compared to other methods. Cu-poor absorbers are known to achieve higher efficiencies in CIGSe solar cells than Cu-rich films, most likely because of the reduced recombination at the interface between the absorber and the buffer layer [30, 31]. However, the co-evaporation process requires costly conditions like high vacuum. In addition, the positions and flux of the individual evaporation sources need to be carefully controlled and have a strong impact on the composition and uniformity of the absorber film.

The sequential deposition mainly consists of two steps: first, the precursor metal film is deposited by sputtering on large area substrates; second, a CIGSe film is formed by annealing or rapid thermal processing (RTP) in an atmosphere consisting of hydride gases (hydrogen selenide (H_2Se)/ hydrogen sulphide (H_2S)) [32]. However, the hydride gases are toxic and environmentally harmful. Although the toxic gases can be replaced by the elemental Se and S in the RTP process, the reproducibility is difficult to maintain due to the uncontrollability of the amount of Se and S.

Non-vacuum, solution-based coating techniques can reduce material cost and instrument investment compared with vacuum deposition. They mainly involve electrochemical techniques, particle-based solution coating and molecular ink based printing or coating. The non-vacuum technique is basically a two-step process, which involves precursor deposition at low temperature followed by a high-temperature annealing step in a chalcogen atmosphere [33-35]. Seeking an air stable molecular ink and simple absorber operation is an important issue in order to achieve high efficiency and low-cost chalcopyrite thin film solar cells [36].

Table 1.1 List of various preparation methods for CIGSe absorber films, and their advantages and disadvantages.

| Methods | Advantages | Disadvantages |
|----------------------------|----------------------------------|--------------------------------|
| Co-evaporation [37, 38] | Precisely controlled composition | High vacuum |
| Sequential deposition [32] | Large area deposition | Toxic gases |
| Printing [33] | Low-cost, high throughput | Air stable ink, low efficiency |

1.2.3 Electronic properties

The power conversion efficiency of CIGSe thin film solar cells is affected by several factors, such as elemental stoichiometry, grain size, surface morphology, defects in the absorber and at interfaces with back contact and buffer layer [22]. In general, the Ga gradient as a function of depth can influence open circuit voltage (V_{oc}), short circuit current density (J_{sc}), and efficiency. Reducing the contact resistance and series resistance can improve the fill factor of the device. Also, the inhomogeneity of the absorber film is a key factor for the efficiency limitation [39]. In order to analyze these factors that influence efficiency, many characterization methods can be applied to chalcopyrite solar cells. For example, majority carrier density and mobility in different materials used in the device can be analyzed by Hall effect, conductivity, and Seebeck coefficient measurements. From the quantum efficiency and electron beam induced current measurements, the minority carrier diffusion length and interface recombination can be investigated. In addition, the dominant recombination mechanism and barrier height information are extracted from J-V curves of the chalcopyrite solar cells [40]. The temperature (T) dependence of the V_{oc} of solar cells can be described as follows:

$$V_{oc} \approx \frac{AkT}{q} \ln \left(\frac{j_{sc}}{j_0} \right) = \frac{E_a}{q} - \frac{AkT}{q} \ln \left(\frac{j_{00}}{j_{sc}} \right) \quad 1.1$$

Where E_a , A, k, j_{00} and j_{sc} are the activation energy of the dominant recombination mechanism, diode ideality factor, Boltzmann constant, reverse saturation current pre-factor and the photocurrent, respectively. The activation energy E_a is the intercept ($T= 0$ K) of the linear part of the temperature dependent open circuit voltages curve. In general, if the value of E_a equals the band gap of the absorber, then the dominating recombination pathway is in the bulk of the absorber; while if the value of E_a is smaller than the band gap of the absorber, the dominating recombination is located at the interface of the heterojunction [41, 42]. The detailed characterization and analysis of CIGSe solar cells will be discussed in the chapter 3.

1.3 Top cell: perovskite solar cells

Hybrid organic-inorganic perovskite solar cells have recently attracted the attention

of the PV research community, with efficiencies above 22% achieved after only a few years of substantial work. The long history of research on halide perovskites was started in 1893 by Wells [43], while the first organic-inorganic hybrid perovskite was introduced with the methylammonium (MA) cation (CH_3NH_3^+) and lead (Pb) [44] or Tin (Sn) [45] in 1978. The organic-inorganic hybrid perovskite materials have the general formula ABX_3 , where A is an organic cation (CH_3NH_3 is one of the most commonly used materials), B is an inorganic cation (usually Pb), and X is a halide (typically iodine (I), often with a small fraction of chlorine (Cl) or bromine (Br)). The band gap of these perovskites can be continuously tuned from 1.5 eV to 3.2 eV by adjusting the ratio between different halides [46]. In 2009, A. Kojima *et al.* used two organolead halide perovskite nanocrystalline materials $\text{CH}_3\text{NH}_3\text{PbBr}_3$ and $\text{CH}_3\text{NH}_3\text{PbI}_3$ to sensitize TiO_2 in dye sensitized solar cells (DSCs), yielding a solar energy conversion efficiency of 3.8% [47]. In 2011, the Nam-Gyu Park group studied $\text{CH}_3\text{NH}_3\text{PbI}_3$ quantum dots on the surface of TiO_2 and improved the photoconversion efficiency to 6.5% [48]. Recently, a record value of a PVK device was demonstrated with efficiencies above 22% in small cells and 19.7% in 1-square-centimeter cells, which is competitive with other thin film PV technologies [8].

1.3.1 Basic structure

As shown in figure 1.6, most perovskite solar cells have one of two different structures: the so-called standard structure and the inverted structure [49-52]. Both structures consist of five parts: the transparent conducting substrate, one or more electron transport materials (ETM), the perovskite layer, the hole transport materials (HTM), and a back contact electrode (such as Au or Ag). The difference between the standard and the inverted structure is that the incident light passes the ETM first in the standard structure (n-i-p), while in the inverted structure (p-i-n) the HTM is facing the incoming light. In the active perovskite, charge carriers are generated upon illumination. The generated electrons and holes are transported to ETM and HTM, respectively and are collected by the top and back contacts. Obviously, the perovskite layer as well as ETM and HTM are the critical components in PVK devices. Consequently, numerous publications on hole transport materials [53, 54], optimization of the fabrication process and architectures [55-57], electron transport materials [54, 58] and the chemical management of the perovskite composition [59-62] were published rapidly [19].

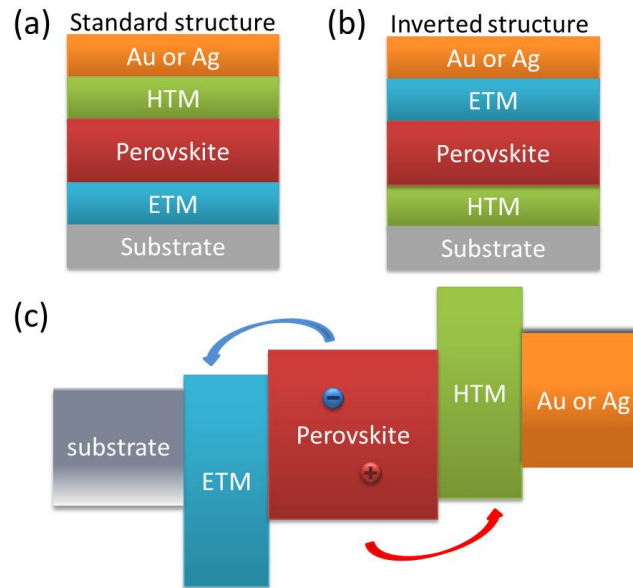


Figure 1.6 Schematic structures of the perovskite solar cells: (a) standard structure; (b) inverted structure; (c) energy level diagram of standard configuration showing charge carrier transport.

1.3.2 Fabrication process

Typically, for the standard structure, the electron transport material is coated on an FTO-coated glass substrate. Subsequently, the perovskite is deposited by two different methods. A low-temperature annealing process ($<150^{\circ}\text{C}$) often helps to improve crystallinity, film morphology, and device performance. Finally, the hole transport material is spin-coated on top, and the back contact (usually gold) is evaporated to finish the device [13].

The fabrication process of the perovskite absorber material ($\text{CH}_3\text{NH}_3\text{PbI}_3$ as an example) can be divided into two categories: a solution-based method using spin-coating of the dissolved precursors and a vacuum-based film deposition method where the constituents are evaporated [63]. As shown in figure 1.7 a and b, the solution-based method can be divided in two different processes, one is spin coating a solution of $\text{CH}_3\text{NH}_3\text{I}$ (MAI) and PbI_2 in one-step on the substrate (figure 1.7 a), another one is by spin coating PbI_2 and MAI separately in two steps on the substrate (figure 1.7 b). The most preferred process is the one-step coating method. In addition to the solution-based method, the vapor deposition technique is also extensively used to prepare perovskite layers. Figure 1.7 c shows a dual-source evaporation technique where $\text{CH}_3\text{NH}_3\text{I}$ and PbI_2 are pre-heated to a certain temperature and simultaneously deposited on the substrate under high vacuum. The method requires very high temperatures and high vacuum conditions to deposit crystalline perovskite films.

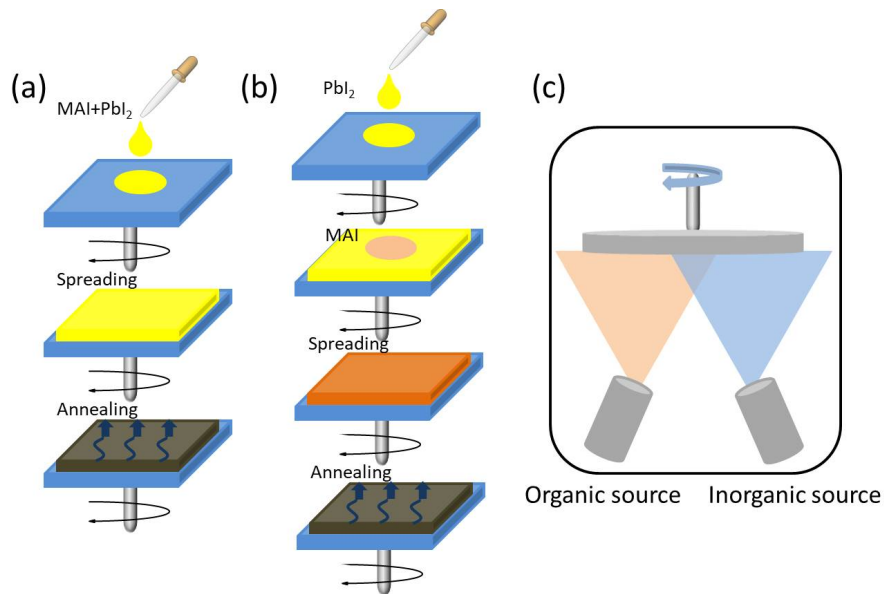


Figure 1.7 $\text{CH}_3\text{NH}_3\text{PbI}_3$ layer preparing techniques: (a) precursor deposition in one-step; (b) sequential deposition technique in two-step; (c) vapor deposition in dual-source [64].

1.3.3 Electronic properties

Compared to the other PV devices, the perovskite solar cells have some inherent advantages and superior properties that allow to achieve high efficiencies. They have excellent light harvesting properties and they also serve as very efficient hole transporting medium [65]. They can be made using a simple, low-cost and low-temperature fabrication process, allowing new applications, such as solar cells on flexible substrates. Due to its high absorption coefficient, the absorber thickness can be reduced compared to other photovoltaic materials [66, 67]. However, even though the absorption spectrum of perovskites shows a very sharp onset, comparable to that of the best inorganic semiconductor absorbers (CdTe and GaAs), in current devices the photocurrent loss is still substantial because of the parasitic absorption in the hole conducting layer and the back reflector [13]. The fill factor of perovskite solar cells is generally lower than that of other cells with over 20% efficiency, probably because the solution-based deposition method leads to the non-uniformity of the active layer with pinholes and resulting carrier shunting. In addition, the stability of PVK devices is also an important issue that currently limits the wide application. Although it has excellent initial performance, the perovskite layer probably degrades within a few hours and the performance dramatically decreases. The reasons for the perovskite degradation are one of the most important research topics in the PVK field, of which the photodegradation by ultraviolet light and humidity are the most likely reasons [13]. Also, the hysteresis during J-V measurements is another obvious character of PVK devices and the origin of the hysteresis is still unclear. Due to the toxicity of Pb, the encapsulation of devices and their recycling are also very important issues for commercial application of PVK devices.

1.4 Perovskite-CIGSe tandem solar cells

As introduced previously, the monolithic (two terminal) tandem solar cell is promising to overcome the S-Q efficiency limitation. Multi-junction solar cells fabricated from III-V semiconductor compounds and alloys such as two-terminal GaInP/GaAs tandem solar cells achieve over 30% efficiency [68, 69]. The higher efficiencies and radiation resistance of III-V cells have made them attractive as replacements for silicon cells on many satellites and space vehicles [70]. However, their slow fabrication by methods such as molecular beam epitaxy (MBE) or metalorganic chemical vapor deposition (MOCVD) and the high cost due to the complex structure and the high price of materials have precluded their adoption in other applications. On the other hand, the hybrid organic-inorganic perovskite breaks new ground in the development of monolithic tandem devices, having excellent photoconversion performance, high absorption, good charge transport characteristics and adjustable band gap [71]. A monolithic tandem solar cell typically consists of a top cell with a wider band gap and a bottom cell with a narrower band gap. For the top cell, perovskite solar cells are suitable candidates due to their large, tunable band gap. For the bottom cell, there is a wide variety of options, such as crystalline Si [72-78], CIGSe [72, 79-81], $\text{Cu}_2\text{ZnSn}(\text{S}, \text{Se})_4$ (CZTS) [82], polymers [83, 84], or narrow band gap perovskites [85-90], for example $\text{CH}_3\text{NH}_3(\text{Sn}, \text{Pb})\text{I}_3$. However, up to now only silicon and CIGSe solar cells have been applied as bottom components in monolithic tandem solar cells combined with a perovskite-based device. Owing to their tunable band gap and the low cost manufacturing process, thin film chalcopyrite CIGSe solar cells can be a good choice for use as bottom cells integrated with PVK. However, to date the performance of monolithic perovskite-CIGSe tandem solar cells is still inferior to that of perovskite-silicon tandem devices, which have been in the focus of the recent research and development efforts [19, 20].

1.4.1 Design of monolithic perovskite-CIGSe tandem solar cells

The monolithic perovskite-CIGSe tandem solar cell consists of a perovskite top cell and a CIGSe bottom cell as shown in figure 1.8. The reason why the perovskite needs to be deposited on top of the CIGSe bottom cell is that typical CIGSe solar cells require a high temperature preparation process for the absorber crystallization. Reversing the order would destroy the subjacent perovskite solar cells. Therefore, the monolithic perovskite-CIGSe tandem solar cells need perovskite as a top cell and CIGSe as a bottom cell, where the incident light passes through the semi-transparent perovskite top cell to the CIGSe bottom cell. The top cell consists of an ETM such as [6,6]-phenyl-C61-butyric acid methyl ester (PCBM), the perovskite materials such as MAPI_3 as the light-harvesting active layer and inorganic conductors as HTM. As introduced in the previous section, the top cell structure is not a typical standard structure of PVK, where the ETM is facing the incoming light and deposited on the substrate first. In the tandem structure, we need to deposit the ETM on top of the perovskite/HTM layers and the incident light passes through the ETM first. This

configuration is called a reversed standard structure. For the bottom cell, a standard CIGSe structure consisting of Mo/CIGSe/CdS/ZnO/AZO is used, in which the CIGSe is the absorber, CdS the buffer layer, and i-ZnO and AZO are window layers. A transparent electron conducting layer is placed on the top of PCBM and a Ni/Al contact grid is placed on top of the entire solar cell. An additional buffer layer between the PCBM layer and the ITO layer can be used to protect the PCBM layer from sputtering damage [19].

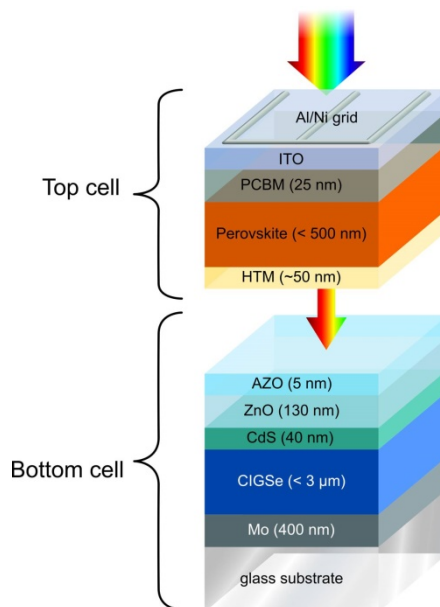


Figure 1.8 Structure of two-terminal perovskite-CIGSe tandem solar cells.

The methods to prepare bottom cell CIGSe was described previously. However, the preparation of the perovskite top cell has to be done by “soft” techniques in order not to destroy the bottom cell. The subsequently deposited inorganic conductors should be made at temperatures below 200°C and satisfy several requirements which will be discussed in the following section. One-step spin coating is used to deposit perovskite layers [91-93]. After spin coating a perovskite precursor on the substrate, the perovskite film is crystallized at 100°C annealing temperature. Analogously, a thin PCBM layer acting as ETM is also deposited by the spin coating method [94]. The ITO and Ni/Al contact grids on top of the entire solar cell are deposited on the top of the PCBM layer or an additional buffer layer by sputtering and thermal evaporation, respectively [18, 95, 96]. The optional additional buffer layer might be needed protect the PCBM layer against high power sputtering damage.

1.4.2 Band alignment

Proper band alignment is crucial for tandem solar cells, directly influencing the conversion efficiency of solar photons and the effective separation of excited charge carriers [97]. As described in the previous section, the photogeneration in a multijunction device is more complicated than in single junction solar cells,

considering the top semiconductor material or active layer absorbs the higher energy incident light and the bottom absorbs the remaining light. As a result, the respective band gaps of the top and bottom absorbers determine the value of the photovoltage and influence the individual photogeneration currents by determining the respectively accessible parts of the solar spectrum. The band gaps of the window layers and the intermediate layers should be selected such that the absorptive losses do not affect parts of the spectrum accessible to the absorber(s) below. Therefore, in principle, large band gap materials as intermediate inorganic hole conductors are preferable to narrow band gap materials [19].

Figure 1.9 shows a schematic energy-level and band alignment of perovskite-CIGSe tandem solar cells. The left part is the bottom cell, including CIGSe absorber, CdS buffer layer and zinc oxide window layer. On the right, the top cell is shown, consisting of perovskite acting as an intrinsic material (i) and light absorber, PCBM as ETM and NiO_x exemplifying the HTM. The tunnel junction is visible in the middle, composed of highly doped n-type AZO and a p-type semiconductor. When the perovskite and CIGSe layers absorb incident light and generate charge carriers, the electrons will drift to the front (ETM) contact while holes drift to the hole-conducting back contact. As a result, the band alignment becomes a very crucial factor for the charge carrier separation in the tandem device, especially the p-type intermediate layer that serves two significant purposes: (i) blocking electron transfer to the back contact and separating the holes from the perovskite layer to avoid charge recombination at the interfaces; (ii) as a component of the tunnel junction ensuring the recombination of holes from the top cell with electrons from the bottom cell [19].

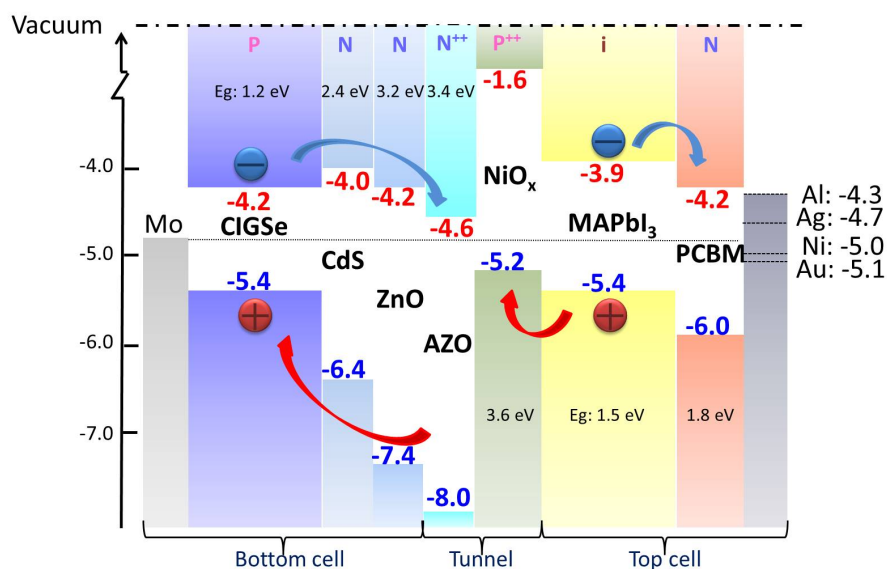


Figure 1.9 Schematic energy-level and band alignment of perovskite-CIGSe tandem solar cells [93, 94, 98-102].

Effective band alignment for tandem solar cells is needed for the charge separation process, which means photogenerated electron-hole pairs are separated, with

electrons drifting to the lower conduction band and holes drifting to the higher valence band. For this process, the valence band edge of the intermediate inorganic hole transport layer needs to be higher than the highest occupied molecular orbital (HOMO) energy level of the $\text{CH}_3\text{NH}_3\text{PbI}_3$ layer, thus leading to the extraction of holes at the interface between the intermediate inorganic hole transporters and the $\text{CH}_3\text{NH}_3\text{PbI}_3$ film. In addition, the conduction band edge of the ETM film should be lower than the lowest unoccupied molecular orbital (LUMO) of the $\text{CH}_3\text{NH}_3\text{PbI}_3$ layer, which prevents electrons from reaching the perovskite and avoids recombination at the interface. Therefore, the HOMO and LUMO energy level of the perovskite layer relate to the choice of valence band edge and conduction band edge for intermediate inorganic hole transporters. Figure 1.10 shows the energy-level diagrams of several typical lead-based perovskites. The band gap of perovskites can be tuned between 1.4-2.9 eV and most of them have a valence band energy around -5.4 eV, which means the valence band edge of HTM should be higher than -5.4 eV [19].

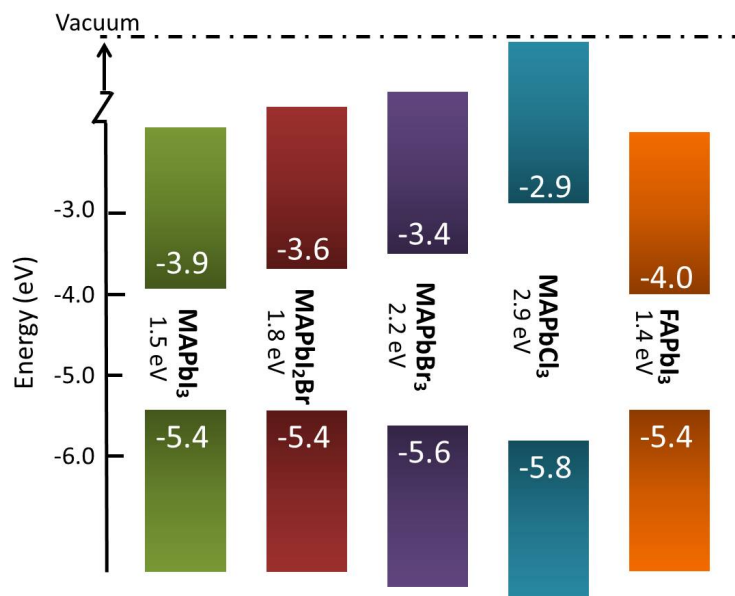


Figure 1.10 Schematic energy-level diagrams of several typical perovskites relative to vacuum level.

1.4.3 Current matching and optical management

As the band alignment for the entire monolithic perovskite-CIGSe tandem solar cell is completed, another large challenge to the fabrication of efficient monolithic tandem solar cells is current matching and optical management between the top and bottom cell [17]. For monolithic tandem devices, the best efficiencies are achieved when the short circuit current density of the top cell (J_{topsc}) matches that of the bottom one (J_{botsc}) [103, 104]. In order to achieve the highest matched current density J_{matchsc} that directly influences the power conversion efficiency of tandem devices, an elaborate optical design of the integrated configuration and accurate control of absorption layer thicknesses are paramount. Current matching is usually achieved by careful

adjustment of the layer thicknesses allowing partial transmission of below-band-gap light to the bottom cell [105, 106], and optical management is employed to optimize the distribution of short wavelength and long wavelength light through the top cell and the bottom cell in order to better utilize the broad solar spectrum [19]. The detailed description of current matching and optical management will be discussed in the chapter 6.

1.5 p-type semiconductor as part of the recombination junction

The intermediate recombination junction of perovskite-CIGSe tandem devices includes a p-type semiconductor as HTM for top PVK and an n-type semiconductor as window layer for bottom CIGSe. The conducting window layer, n-type AZO on CIGSe devices with good electrical conductivity and high transparency in the visible spectrum is being extensively used in thin film CIGSe technologies [97]. However, a good p-type semiconductor with low-resistance contact to the device and high transmission of most of the long wavelength incident light to the bottom CIGSe absorber layer is still waiting to be found. The reason for the slow progress in finding appropriate materials appears to be a lack of research efforts on this topic which deserves more attention from the tandem community. Therefore, in the following section I will put forward some potential p-type semiconductors as potential intermediate layers for the monolithic perovskite-CIGSe tandem solar cells.

1.5.1 Requirements for the intermediate layer

As one of the components of the tunnel junction for tandem devices and at the same time a hole selective contact for the top perovskite cell, the intermediate inorganic hole transport material (IIHTM) of perovskite-CIGSe tandem solar cells needs to meet some basic requirements: (i) be sufficiently transparent, so that the bottom CIGSe layer can absorb as much long-wavelength light as possible, (ii) good conductivity, which depends on the carrier concentration and mobility, while the high carrier concentration may lead to increasing free carrier absorption that can reduce the transparency [107], (iii) appropriate band structure, which is compatible with the perovskite layer in the top cell and with the n-type transparent conductors below as one of the components of the tunnel junction, (iv) high mobility, effectively extracting and transferring holes from the HOMO energy level of the light absorber, (v) be chemically compatible with the perovskite layer, avoiding a chemical reaction and possible degradation of the active layer of the top PVK, (vi) use a simple deposition process at low temperature by soft techniques, preventing degradation of the bottom cell layers. Besides these necessary conditions, the optoelectronic properties, the thermal stability and interface are also important to be taken into account [19].

1.5.2 Promising candidates

Figure 1.11 shows a comparison of the schematic energy-levels relative to the vacuum level of several representative inorganic materials as IHTM, such as nickel oxide, copper-based compounds, some transition metal oxides like molybdenum oxide and vanadium pentoxide. Among these inorganic materials, the valence band edges of the copper-based compounds and nickel oxide match best with $\text{CH}_3\text{NH}_3\text{PbI}_3$ at -5.4 eV. Cu_2O and CuGaO_2 as promising candidates will be discussed in chapters 4 and 5.

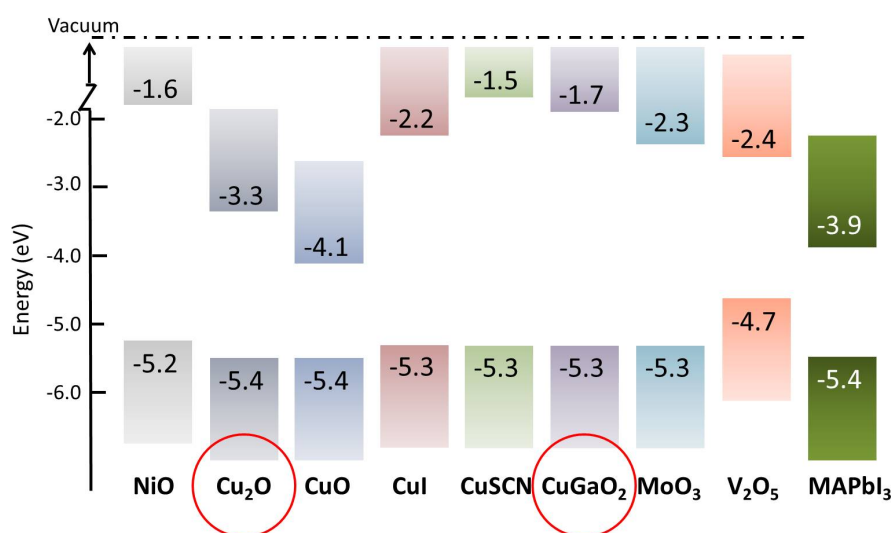


Figure 1.11 Schematic valence and conduction band energy-levels of several representative inorganic materials relative to the vacuum level compared with $\text{CH}_3\text{NH}_3\text{PbI}_3$ [93, 108-112].

1.6 Objectives and outline

In order to understand the conditions for high performance photovoltaic devices, a theoretical model of a monolithic perovskite-CIGSe tandem solar cell with Cu_2O and CuGaO_2 as intermediate layers and a low band gap bottom cell deposited using a molecular ink was constructed and investigated. The optical and electrical simulations were conducted to show the performance limitation of Cu_2O or CuGaO_2 based tandem devices.

This thesis is mainly separated into 8 chapters.

Chapter 1 is an introduction for the solar cell basics and backgrounds of monolithic perovskite-CIGSe tandem solar cells.

Chapter 2 is an experimental section, including sample preparation and characterization.

Chapter 3 is describing the low band-gap $\text{CuIn}(\text{S}, \text{Se})_2$ absorber deposition using molecular ink.

Chapter 4 is showing Cu_2O as an intermediate transparent conducting oxide layer for

monolithic perovskite-CIGSe tandem solar cells.

Chapter 5 is discussing the p-type semiconductor CuGaO_2 for monolithic perovskite-CIGSe tandem solar cells.

Chapter 6 shows optical and electrical simulations for monolithic perovskite-CIGSe tandem solar cells.

Chapter 7 is the conclusion part.

Chapter 8 is an outlook of future work on monolithic perovskite-CIGSe tandem solar cells.

2 Experimental section

2.1 Sample preparation

In this section, only the preparatory methods are introduced which were essential for the materials and devices of this thesis. For all other deposition methods, the reader is referred to general text books (e.g. Poortmans/Luque/Smets etc.)

2.1.1 Spin coating

Ink preparation: first, 0.3M copper (II) chloride (Alfa-Aesar, 98%), 0.33M indium chloride (Alfa-Aesar, 99.99%) and 1.32M thiourea (ACS, Reag. Ph Eur, 99%) were added to the mixed solution of ethanol (Sigma-Aldrich, 99.8 %), ethylene glycol (Sigma-Aldrich, 99.8 %) and ethylene glycol butyl ether (Sigma-Aldrich, 99 %) (volume ratio is 3:2:x) [34]. Every time after adding one reagent the precursor solution should be homogenized by means of ultrasonic treatment and stirring for 10 min. For the Na treatment samples, the precursor solution would add 0.1M NaCl based on this ink.

Spin-coating and pre-heating: Before the spin-coating process, the ink was filtered by using a pore size 800 nm polytetrafluoroethylene filter. Then the ink was spin-coated at 2000 rpm for 60 sec on a molybdenum (800 nm) coated glass substrate, which is cleaned for 10 min each by acetone, ethanol, and finally water. Each sample size is 2.5 cm×2.5 cm. The sample was pre-heated on a hot plate at 250°C for 5 min in order to remove the solvent. The spin-coating and preheating process should be repeated several times so that the film can reach the desired thickness.

Annealing process: The samples were placed in a quartz tube furnace with 0.4 g selenium (Aldrich, 99.5 %) and annealed under ambient pressure at 400°C for 20 min, followed by another 20 min at 560°C under Argon atmosphere to grow the crystal grains of the CISSe absorber. Some samples would continue another 5 min at 580°C under Argon or Ar/H₂S atmosphere.

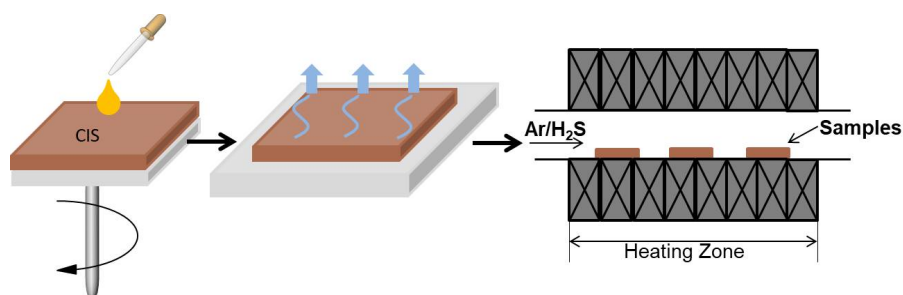


Figure 2.1 The schematic diagram of thin film process consisting of ink formulation, spin coating, pre-heating and annealing.

The following nomenclature is used to indicate the preparation parameters:

TABLE ON NEW PAGE

Table 1 List of sample preparation parameters.

| Sample name | Volume ratio | Layers | Annealing process | | |
|----------------------------|--------------|--------|-------------------|------------|-----------------------------|
| | | | 560°C (Ar) | 580°C (Ar) | 580°C (Ar/H ₂ S) |
| V0-3-560(Ar) | 3:2:0 | 3 | √ | | |
| V1-5-580(Ar) | 3:2:1 | 5 | √ | √ | |
| V3-7-580(H ₂ S) | 3:2:3 | 7 | √ | | √ |
| V5-9-580(H ₂ S) | 3:2:5 | 9 | √ | | √ |

Cell fabrication: the CuIn(S, Se)₂ (CISSe) absorbers were etched in 10% KCN solution for 3 min to remove Cu_x(S, Se) phases [113]. A CdS buffer layer was deposited on the film by chemical bath deposition [114], and i-ZnO and aluminum doped ZnO (AZO) window layers by sputtering [115, 116]. A Ni/Al contact grid on top of the solar cell was deposited by evaporation using a shadow mask [37, 96, 117]. The solar cell area was defined by mechanical scribing to 0.5 cm². There is no antireflection layer on the cell.

Preparation of wet chemical samples of Cu₂O films: the preparation process of Cu₂O films was developed from the procedure reported previously [118]. The glass substrates, 2.0 mm thick, 2.5 cm × 2.5 cm, were cleaned ultrasonically in a detergent, deionized water, acetone, and isopropanol sequentially. A solution of CuI in acetonitrile (5~10 mg/mL) was spin coated onto glass substrates at 4000 rpm for 60 sec. The substrate was immersed in 10 mg/mL aqueous NaOH solution for 5 sec, rinsed with distilled water and dried by N₂. Then the substrate was heated at 120°C for 20 min. In order to improve the surface cleaning process, some samples were spin coated with 10 mg/mL aqueous NaOH solution and distilled water at 4000 rpm for 60 sec three times, respectively, instead of being immersed in NaOH solution and rinsed with distilled water. Then the substrate was heated at 100°C for 20 min.

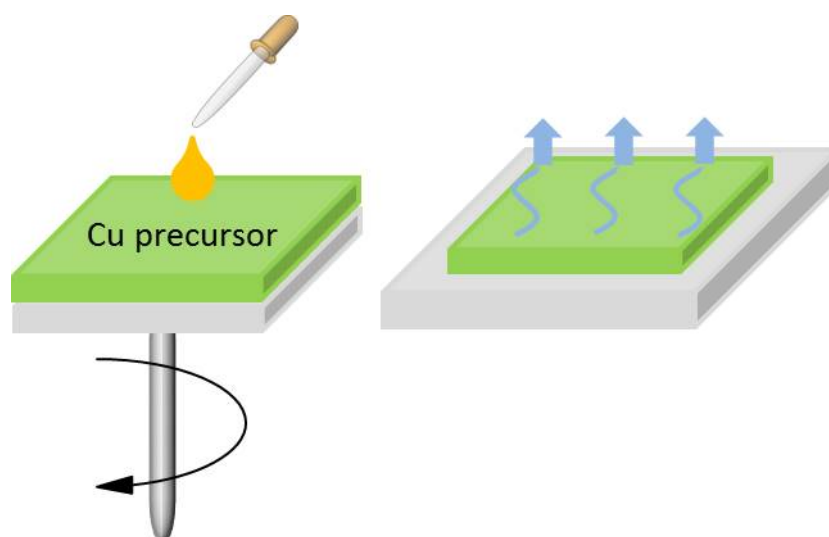


Figure 2.2 The schematic diagram of the wet chemical approach.

2.1.2 Sputtering

Preparation of samples by sputtering: Cu₂O films were deposited on glass substrates by sputtering from a Cu or CuO target (FHR Anlagenbau GmbH, 99.99%, purity,) with a reactive rf magnetron sputtering system using O₂/Ar and N₂/Ar as working gases, respectively. The glass substrates, 2.0 mm thick, 2.5 cm × 2.5 cm, were cleaned by ultrasonic in detergent, deionized water, acetone, and isopropanol sequentially. The target-to-substrate distance was about 7.0 cm. The substrate was not intentionally heated and rf sputtering power was 60 W. Prior to the deposition, both Cu and CuO targets were pre-sputtered for 15 min to remove surface contaminations. The base vacuum level was 1×10⁻⁷ mbar, and the pressure during the deposition was kept at 4×10⁻³ mbar. In order to control the oxygen flow during the whole deposition, the concentration of oxygen in the O₂/Ar mixture was 5% and the O₂/Ar mixture flow rate was varied between 20 sccm and 100 sccm. In order to control the nitrogen-doping concentration in the films, the flow rate of the N₂/Ar mixture was fixed at 50 sccm and the content of nitrogen in N₂/Ar mixture was varied between 0% and 50%. The deposition time was 5 min [103].

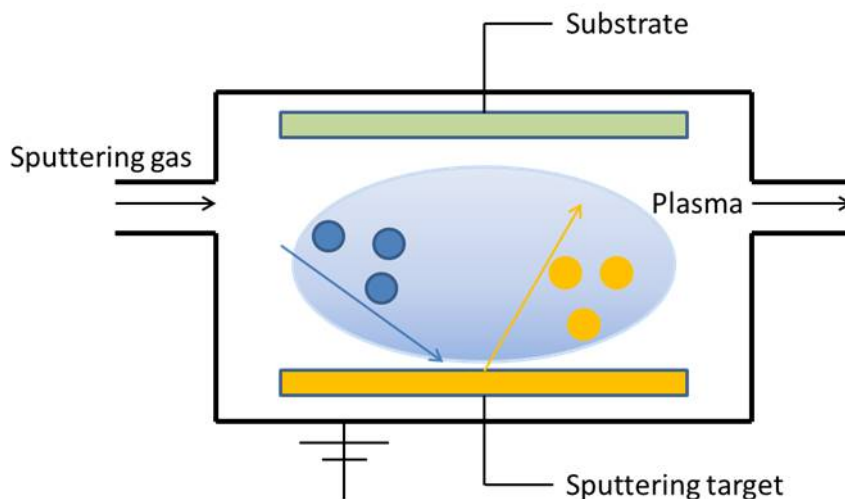


Figure 2.3 The schematic diagram of reactive rf magnetron sputtering approach.

Preparation of sputtering samples: CuGaO₂ films were deposited on glass or molybdenum substrates by sputtering from a CuGaO₂ target (FHR Anlagenbau GmbH, 99.99%, purity, diameter 125 mm) with a reactive rf magnetron sputtering system using argon or O₂/Ar as working gases. The substrates, 2.0 mm thick, 2.5 cm×2.5 cm, were cleaned in acetone and ethanol. The target-to-substrate distance was varied from 5 cm to 9 cm. The substrate was not intentionally heated and the rf sputtering power was 60 W. Prior to the deposition, the target was pre-sputtered for 15 min to remove surface contaminations. The base vacuum level was 1×10⁻⁷ mbar, and the pressure during the deposition was kept at 4×10⁻³ mbar. In order to control the oxygen flow during the whole deposition, the concentration of oxygen in the O₂/Ar mixture was 1% and the O₂/Ar mixture flow rate was fixed at 25 sccm. The deposition time was varied from 45 sec to 12 min.

Sodium doping: A sodium metal dispenser was used as source of sodium doping on

the sputtered CuGaO₂ sample. An AC or DC electric current was used to heat this sodium dispenser, for this reason the pre-cut length of dispenser is normally provided with special terminals to make it use easier and also guarantee a homogeneous heating. Generally, the metal dispenser is heated to a certain temperature and the temperature corresponds to the evaporation rate of the metal. Before the evaporation, the MBE chamber and metal dispenser need a typical bake-out process to avoid contaminations. When the current was stabilized at 7.0 A, the sample was turned towards the sodium dispenser and the evaporation of sodium on the sputtered CuGaO₂ sample was started. After 6 min of Na deposition, the sample was immediately transferred to the analysis chamber of the CISSY system to measure XPS and UPS, attempting to minimize the sodium diffusion to the bulk.

2.2 Analytical methods

Characterization: X-ray diffraction (XRD) measurements were conducted on a Bruker D8-Advance X-ray diffractometer with Cu K α radiation. The transmittance (T) and reflectance (R) were measured in the wavelength range of 350–1500 nm by an ultraviolet–visible spectrophotometer (PerkinElmer Lambda-950). The square resistance (Ω/sq) was measured by four point probe resistivity measurements (4PP). X-ray photoelectron spectroscopy (XPS) was performed without breaking the vacuum between deposition and analysis in a combined system CISSY [119] which will be introduced in section 2.3 with a VG Clam IV analyzer using Mg K α ($h\nu = 1253.6$ eV) as the excitation energy from a SPECS XR 50 source to investigate the chemical and electronic states at the surface. For ultraviolet photoelectron spectroscopy (UPS), a helium lamp providing the He I line at $h\nu = 21.21$ eV and the He II line at $h\nu = 40.81$ eV was used and the secondary electron cut-off region was recorded with a sample bias at -15 V. X-ray reflectometry (XRR) was measured by a Panalytical X'Pert MPD to determine the layer thickness, surface roughness and density. Scanning electron microscopy (SEM) measurements were undertaken by a LEO 1530 GEMINI SEM of Zeiss. The contact angle was measured by using the “contact angle system OCA” obtained from Data Physics Instruments GmbH, Germany. The photovoltaic performance of CuIn(S, Se)₂ was measured under a solar simulator using standard test conditions (AM 1.5G, 100 mWcm⁻², and 23°C). The quantum efficiency was measured by using an illumination system with two sources (halogen and xenon lamps) and a Bentham TM300 monochromator (Bentham Instruments, Berkshire, UK). Reference measurements were performed on calibrated Si and Ge detectors. In order to measure temperature dependent open circuit voltages and evolution of efficiencies with temperature in the range of 150 to 300 K in steps of 10 K, samples were illuminated by a single halogen lamp which is not a standard test condition (the light intensity less than 100 mWcm⁻²) and there is a shutter to switch from dark to illuminated conditions. X-ray reflectometry (XRR) which is a surface-sensitive analytical technique was used to characterize surfaces, thin films and multilayers [120]. The basic principle of XRR measurement is that a flat surface and each of the underlying interfaces reflects x-rays and the detector collects the intensity of the

reflected x-rays in the specular direction (equal to the incident angle). The measured data is fitted to a simulated curve, e.g. calculated by the recursive Parratt's formalism [121], combined with an analytical term accounting for interface roughness (usually Debye-Waller) to analyze layer thickness and interfacial roughness.

2.2.1 XPS characterization

X-ray photoelectron spectroscopy (XPS) as a widely used approach to study the chemical composition of surfaces has shown powerful ability to explore the first few atomic layers and assign their chemical states [122]. The surface analysis by XPS is investigated by irradiating a sample under vacuum with soft x-rays and analyzing the emitted photoelectrons. The obtained spectrum is constructed by plotting the detected photoelectrons per energy interval versus their kinetic energy, which is unique for each element. Therefore, the peak position indicates the chemical state of element. Additionally, the peak height and peak area are used for quantitative analysis, i.e. for determining the concentration of the elements on the sample surface. Generally, Mg K α (1253.6 eV) and Al K α (1486.6 eV) x-ray sources are used. The x-rays emitted by these anodes interact with atoms of the sample surface, resulting in the emitting of the photoelectrons, which is the photoelectric effect as shown in figure 2.4. The photoelectrons emitting process is described as following equation [123]:

$$E_{binding} = E_{photon} - (E_{kinetic} + \Phi) \quad (2.1)$$

Where $E_{binding}$ is the binding energy of the electron, E_{photon} is the energy of the X-ray photons being used (1253.6 eV for Mg K α and 1486.6 eV for Al K α), $E_{kinetic}$ is the kinetic energy of the electron as measured by the XPS instrument and Φ is the work function of the spectrometer.

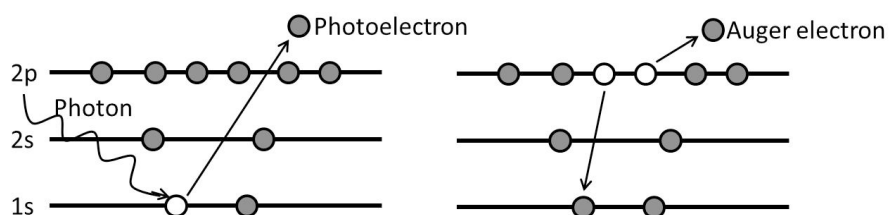


Figure 2.4 The XPS emission process (left) and Auger process (right).

Besides the photoelectrons emission process, Auger electrons are emitted due to the relaxation of the excited ions remaining after the photoelectron emission process as shown in figure 2.4 right, in which an outer electron fills the inner vacancy resulted from photoelectron emission and the second electron is emitted with the excess energy. The Auger electron emission is a rather fast process in 10^{-14} sec after the photoelectron emission. The kinetic energy of the Auger electron does, unlike that of the photoelectron, not depend on the energy of the absorbed photon but only on energy differences between the initial and final ion energies. Thus, the ionizing photons from the anode lead to emission of a photoelectron and (an) Auger

electron(s).

In fact, the mean free path of the photons on the order of micrometers is much higher than that of the photoelectrons on the order of tens of angstroms. Therefore, only those of the photoelectrons that originate from tens of angstroms below the sample surface can escape the sample surface without energy loss, which are captured and analyzed by the Electron Spectrometer and can be plotted as useful peaks. On the other hand, some photoelectrons can suffer energy losses on their way to the sample surface due to the inelastic scattering, which cannot produce useful peaks but the signal background. The background increases dramatically in a small kinetic energies window (10-100 eV) due to these energy loss photoelectrons, which are also called secondary electrons.

2.2.2 UPS characterization

In order to obtain a better energy resolution and make use of a higher photoionization cross section, UV light can be used for photoelectron spectroscopy. The photoelectron spectroscopy by UV light is named as ultraviolet photoelectron spectroscopy (UPS), operating on the same principles as XPS. The excitation sources for UPS measurement are normally He I (21.22 eV) and He II (40.81 eV). The excitation energy can be tuned by varying the pressure of helium in the discharge lamp. The energy of photons used in the UPS is much lower than that in the XPS, therefore, most core level photoemissions are not accessible using UPS and the spectral acquisition is limited to the valence band region as shown in figure 2.5. The UPS measurement is mainly used to calculate valence band edge and work function of materials, which is very useful for my research topic, determining the band structure of semiconductors and investigating the band alignment for perovskite-CIGSe tandem solar cells.

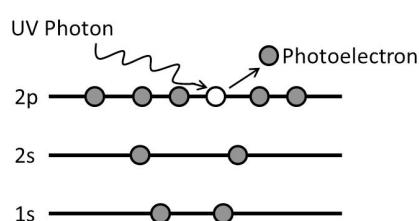


Figure 2.5 UPS emission process: valence photoelectrons are ejected by the UV photons.

Figure 2.6 shows a survey spectrum of a material measured by UPS. Normally, a bias voltage -15V is applied to the UPS measurement to separate sample and analyzer spectral cutoffs, and to increase the secondary electron yield. The position of the valence band maximum (VBM) is determined by the linear extrapolation of the valence band, which is the intersection of the leading edge with the base line. The work function is the difference energy between the Fermi level and vacuum level. As a surface property, the work function is strongly influenced by variation in composition or structure at the surface, such as atmospheric contamination. The work function is obtained by measuring the difference energy between the Fermi

level and the secondary electron edge, and subtracting this value from the incident UV photo energy (He I=21.22 eV).

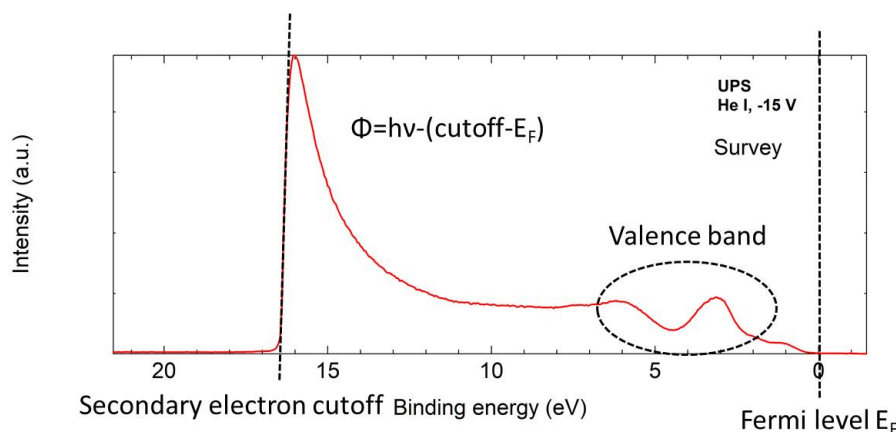


Figure 2.6 A survey spectrum of a material measured by the UPS.

2.3 The CISSY system

The CISSY is a combined instrument system for thin film deposition and surface/interface analysis of materials and devices, which was constructed as a laboratory surface analysis system using commercial x-ray and UV sources or as beamline end station at the BESSY II synchrotron facility and its name is short for CIS and Synchrotron [119]. As shown in figure 2.7 and 2.8, the CISSY system mainly consists of four parts, which are XPS and UPS measurements, magnetron sputtering chamber, surface photovoltage (SPV) and molecular beam epitaxy (MBE) analysis, and a glove box for chemical deposition. The sample substrate can be introduced to the system via glove box and load-locks, one is directly connected with the preparation chamber, and another one is located at the side of the sputter chamber. After chemical deposition in the glove box or preparation by magnetron sputtering, samples are transferred directly to the preparation chamber and transported to the analysis chamber for XPS and UPS measurements by a programmed manipulator, in which entire process samples are under vacuum all the time and potential contaminations can be avoided. The benefit of this special feature is making XPS and UPS characterizations more precise and reliable, especially for metal oxides deposited by magnetron sputtering, which are easily contaminated in air. The MBE and SPV section allow the deposition of thin films using metal dispensers and MBE sources and measures surface photovoltage of devices under UHV in the spectral or time resolved mode.

The preparation chamber and analysis chamber of the CISSY system are maintained under high vacuum of $<10^{-8}$ mbar and other chambers are also kept around $<10^{-7}$ mbar. In order to prevent unintentional leaks or wrong operations, all the chambers are equipped with safe shutters to be separated. For the XPS analysis, it is rather sensitive to the surface of target samples and requires extremely low pressure to avoid sample surface from contamination. Generally, assuming a sticking coefficient

of 1, the surface of the target sample is contaminated with a 1.0 monolayer by gas molecules in 10 sec under a pressure of 10^{-7} mbar, while in 100 sec for 10^{-8} mbar. Therefore, it is necessary to keep the preparation chamber and analysis chamber under ultra-high vacuum for accurate XPS measurement.

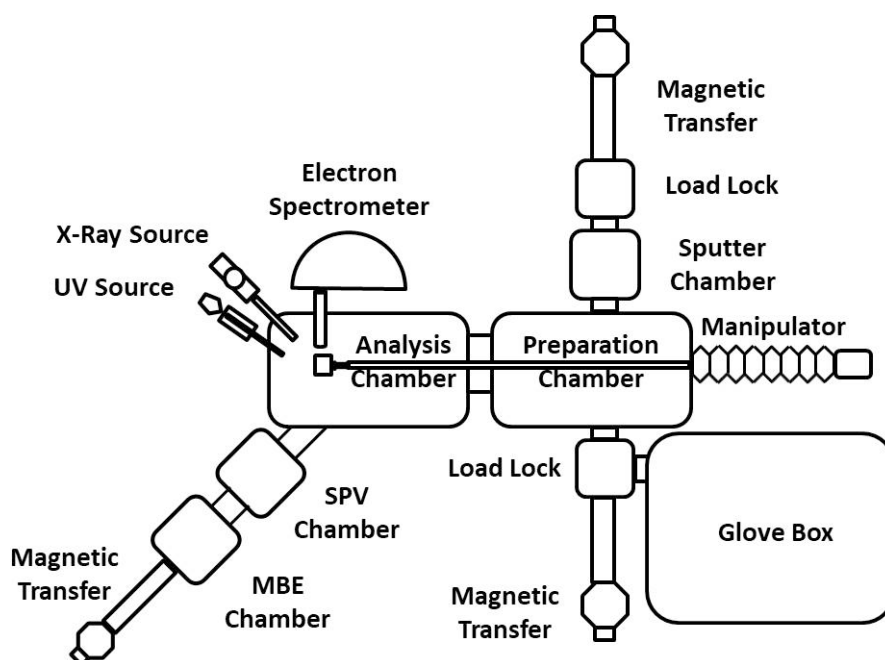


Figure 2.7 The schematic diagram of the CISSY system.

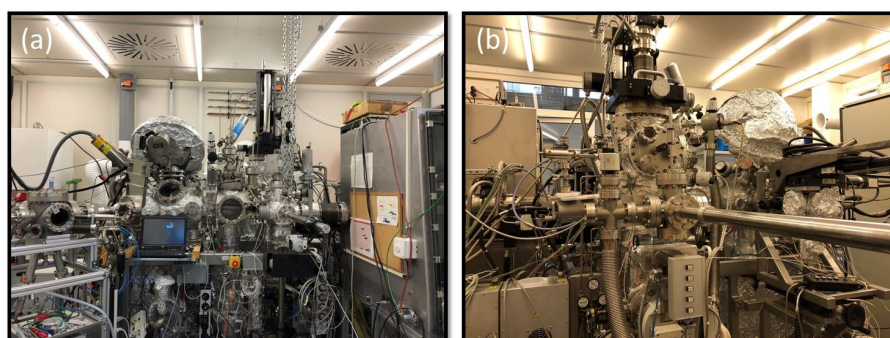


Figure 2.8 Photos of the CISSY system: (a) front side (glove box partly visible on the right side); (b) back side (sputtering part).

2.4 Simulation methods

Optical simulation: The optical simulation was performed by the in-house software RefDex based on the transfer matrix method [124]. The RefDex is mainly divided into four parts: nk calculator, stack data, optical data and RT calculator. Part 1 is a calculator for the optical constants of thin film samples, which are extracted from measured UV-Vis reflection and transmission data. Part 2, 3 and 4 are used to import each layer's optical constants and calculate the reflection/transmission/absorption (R/T/Abs). To build a perovskite-CIGSe tandem solar cell structure, all the layers' optical constants are imported to the part 4, which is consisting of Mo/ CIGSe/ CdS/

ZnO/ AZO/ p-type-semiconductor/ CH₃NH₃PbI₃/ PCBM/ ITO/ glass. Parameters are set in the part 3 and 4. The thickness of each layer is varied to optimize the matched current density and R/T/Abs values of tandem solar cells.

Electrical simulation: electrical simulation was performed by SCAPS. SCAPS (a Solar Cell Capacitance Simulator) is a one dimensional solar cell simulation program developed at the Department of Electronics and Information Systems (ELIS) of the University of Gent, Belgium [125]. SCAPS was originally developed for the CuInSe₂ and CdTe solar cells. Now its application extends for many other solar cells such as Si and GaAs family. The program includes many parameters setting, i.e. band gap (E_g), electron affinity (χ), dielectric permittivity (ϵ), CB effective density of states (N_C), VB effective density of states (N_V), electron thermal velocity (v_{thn}), hole thermal velocity (v_{thp}), electron mobility (μ_n), hole mobility (μ_p), acceptor density (N_A), donor density (N_D), all traps (defects) (N_t). In addition, defects in bulk or at interface can be graded. A description of the program, and the algorithms it uses, is found in the literature [126]. The electrical simulation of perovskite-CIGSe tandem solar cells is obtained by connecting top perovskite cell and bottom CIGSe cell optically and electrically. All the detailed parameters will be shown in chapter 6 and Appendix. The tandem cell is considered to be illuminated under AM1.5G solar spectrum with 100 mW/cm² incident power density.

3 Low band-gap $\text{CuIn}(\text{S}, \text{Se})_2$ absorber deposition using molecular ink

This chapter is mainly based on the following publication:

Wang, Y., Lin, X., Wang, L., Köhler, T., Lux - Steiner, M. C., & Klenk, R. (2017). Low band-gap $\text{CuIn}(\text{S}, \text{Se})_2$ thin film solar cells using molecular ink with 9.5% efficiency. *physica status solidi (c)*, 14(6).

3.1 Background

$\text{Cu}(\text{In,Ga})(\text{S}, \text{Se})_2$ as one of the most competitive thin film solar cells has achieved conversion efficiency up to 22.9% [127]. In order to achieve low band-gap thin film solar cells which can play an important role in tandem solar cells combined with perovskite solar cells [18, 63, 72, 128, 129], adjusting Ga/In or S/Se atomic ratios can be an effective method [130]. Non-vacuum solution-based coating techniques can reduce material cost and instrument investment compared with vacuum deposition. Examples of solution-based coating includes electrochemical techniques, particle-based solution coating and molecular ink based printing or coating (see Chapter 2).

For example, Ahn et al. prepared a precursor solution mixed from metal acetates, ethanol, and ethanolamine and showed a conversion efficiency of as high as 7.72% [131]. In 2015, Oh et al. used water-based Cu-In-S and Se inks to fabricate $\text{CuIn}(\text{S}, \text{Se})_2$ thin film solar cells with 4.55% efficiency [132]. Recently, Uhl et al. prepared a stable dimethyl sulfoxide (DMSO)-based ink consisting of a copper–thiourea–chloride complex and an indium–DMSO–chloride complex to fabricate $\text{CuIn}(\text{S}, \text{Se})_2$ solar cells and achieved up to 13.0% efficiency [36]. But the whole process, including the ink preparation, deposition, and annealing was carried out in a glove box, which limited the applicability to industrial processes. Hence, seeking an air stable molecular ink and simple absorber operation becomes an important issue to prepare high efficiency and low cost $\text{CuIn}(\text{S}, \text{Se})_2$ thin film solar cell. Figure 3.1 shows the schematic structure of the CIGSe solar cells.

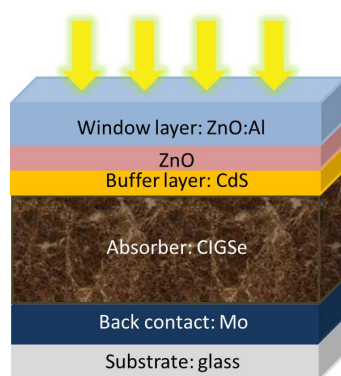


Figure 3.1 Schematic structure of the CIGSe solar cells.

Vacuum free and solution process based routes to the preparation of chalcopyrite absorbers for solar cells provide more options in device design and manufacturing that are not available by the standard vacuum based approaches. In order to fully exploit these options, the precursor should contain neither nanoparticles nor hazardous chemicals, and it should be stable under ambient conditions. In this chapter, a non-vacuum, simple solution coating approach for $\text{CuIn}(\text{S}, \text{Se})_2$ thin film preparation based on spin coating of an air stable molecular ink containing metal chlorides and thiourea in organic solvents was investigated. Several key parameters directly influencing the performance of the resulting solar cells have been identified. Wetting of the glass/Mo substrate has been adjusted by varying the concentration of ethylene glycol butyl ether in the ink. Before annealing in Ar/Se at atmospheric pressure, several cycles of ink deposition and drying can be used to increase the thickness of the precursor stack. Careful balancing of ink concentration, number of precursor deposition cycles, and annealing temperature profile will transform the multilayer precursor into a sufficiently thick, continuous, large grained film as required for high quantum efficiency, and good red response of the cells. These optimizations aimed at high photo current have already led to an efficiency of 9.5% with a small band-gap of 1.02 eV.

3.2 Results and discussion

3.2.1 EGBE solvent variation

Figure 3.2 (a) shows the clear green precursor solution containing copper and indium salts. A stable clear yellow molecular ink in Figure 3.2 (b) is formed with copper chloride, indium chloride and thiourea. The molecular ink is stable in air at least for a few hours. The three-solvent solution is a mixed solution of ethanol and ethylene glycol which are for dissolving the metal salts, and ethylene glycol butyl ether which is for the viscosity of ink. When the percentage of ethylene glycol butyl ether in the solvent mixture increases from 0% to 58.3% (three solvents volume ratio from 3:2:0 to 3:2:7), the viscosity of molecular ink is changed, while the indium chloride cannot completely dissolve in the solvent by increasing the ratio of ethylene glycol butyl ether in mixed solvents (volume ratio up to 3:2:7). Because the viscosity will influence the wetting behavior between the ink and the substrate, the quality and homogeneity of the CISSe solar cells films maybe related to the content of ethylene glycol butyl ether in the mixed solution. One way to examine the wetting behavior is to measure the contact angle of the ink on the substrate. From Figure 3.2 (c) and (d), the contact angle of the molecular ink with volume ratio 3:2:0 is 32° , higher than the 23° of the molecular ink with volume ratio 3:2:5, showing adding ethylene glycol butyl ether as solvent can indeed improve the wetting behavior of the molecular ink on the substrate.

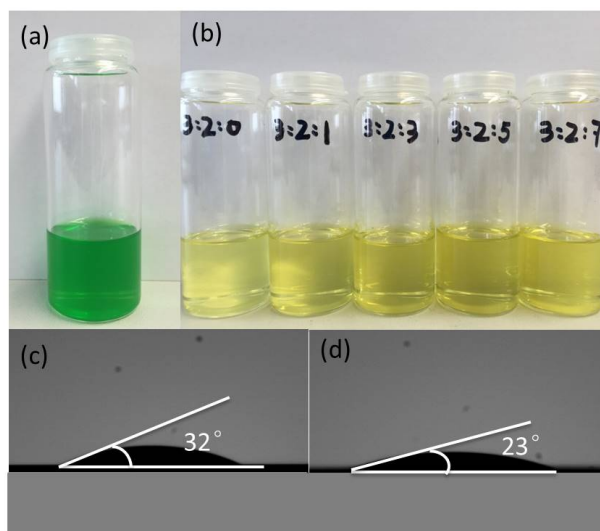


Figure 3.2 (a) precursor solution with copper and indium; (b) molecular ink with copper, indium and thiourea; (c) contact angle between the molecular ink (three solvents volume ratio is 3:2:0) and Mo substrate; (d) contact angle between the molecular ink (three solvents volume ratio is 3:2:5) and Mo substrate.

Figure 3.3 shows the XRD patterns of the resulting CISSe solar cells made with different content of ethylene glycol butyl ether in the precursor solvent. Both of them have the CuInSe_2 structure with lattice constants of $a = 5.782 \text{ \AA}$ and $c = 11.619 \text{ \AA}$ (JCPDS card 40-1487), which suggests using a different content of ethylene glycol butyl ether in the mixed solvent has no impact on the effective formation of the CuInSe_2 structure. The main peaks including (112), (204), (220) orientation can be observed. As the detected samples are completed solar cells, some peaks related to the ZnO layer, Mo substrate, indium contact and aluminum grids also can be observed.

As shown in Table 3.1 and Figure 3.4, even at optimized annealing conditions (see 3.2.3), the beneficial influence of the EGBE addition which improves wetting behavior of ink on the substrate and homogeneity of the CISSe film can be seen in the cell performance. The photoconversion efficiency of sample V3-9-580(H_2S) is 8.15%, with an increase of 127% from the photoconversion efficiency of sample V0-9-580(H_2S) with 3.58%. Not only the fill factor, which is closely related to the homogeneity of the CISSe film has greatly increased from 49.5% to 62.5%, but also the open-circuit photovoltage and the short-circuit photocurrent density have been improved from 384.9mV to 485.2mV and from 18.78 mA/cm^2 to 26.90 mA/cm^2 , respectively. Furthermore, the external quantum efficiency (EQE) reaches up to 85% at 640nm wavelength and then gradually decreases towards higher wavelengths, implying there is a small loss of charge carriers generated. The blue response around 400–500 nm (in the region of the CdS band gap) is a complex function of the buffer and TCO properties and may also depend on the microstructure (roughness) and effective doping of the absorber. Moreover, the thickness of CdS from the chemical bath may be influenced by the absorber surface properties. At this point there is no sufficient data to further clarify the relationship the quantum efficiency and ink

properties.

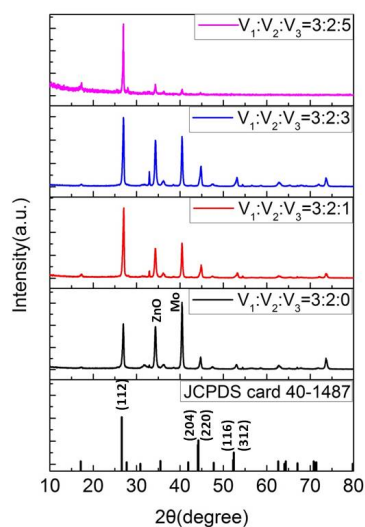


Figure 3.3 The XRD patterns of the CISSe solar cells with different content of ethylene glycol butyl ether in the mixed precursor solvent.

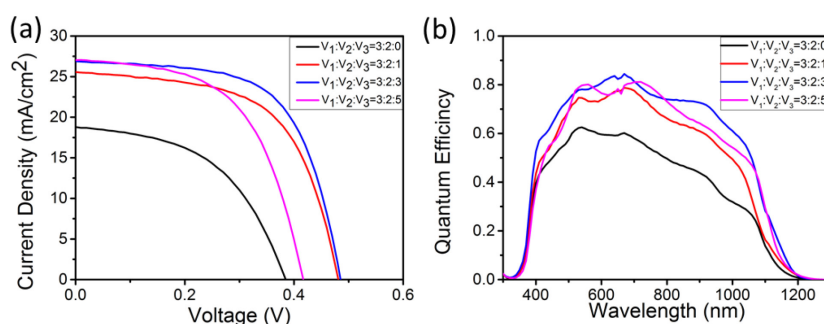


Figure 3.4 (a) the J-V curves and (b) external quantum efficiency characteristics of the CISSe solar cells with different content of ethylene glycol butyl ether in mixed solvent.

Table 3.1 Comparison of Open-Circuit Photovoltage (V_{oc}), Short-Circuit Photocurrent Density (J_{sc}), Fill Factor (FF), and Photoconversion Efficiency (η) for samples with different content of ethylene glycol butyl ether in molecular ink.

| Cell(Cu:In=0.9) | V_{oc} (mV) | J_{sc} (mA/cm ²) | FF (%) | η (%) |
|-----------------------------------|---------------|--------------------------------|--------|------------|
| CISSe(V0-9-580(H ₂ S)) | 384.9 | 18.78 | 49.5 | 3.58 |
| CISSe(V1-9-580(H ₂ S)) | 481.1 | 25.57 | 59.4 | 7.31 |
| CISSe(V3-9-580(H ₂ S)) | 485.2 | 26.90 | 62.5 | 8.15 |
| CISSe(V5-9-580(H ₂ S)) | 416.9 | 27.02 | 56.0 | 6.31 |

3.2.2 Absorber thickness variation

Although the solvent ethylene glycol butyl ether have positive effect on increasing the wetting behavior between the molecular ink and substrate and improving the homogeneity of the film in CISSe solar cells, the thickness of CISSe absorber films that is related to the absorption of solar spectrum also can influence the photoconversion performance of CISSe solar cells. In order to achieve highly short

circuit current, the absorber layer should be prepared with a certain thickness, which requires repeating the cycles of spin-coating and pre-heating treatment. The morphologies of the annealed CISSe thin films were studied by scanning electron microscope (SEM). From the SEM cross section image of sample V5-5-560(Ar) with a Mo/CISSe/CdS/i-ZnO/Al:ZnO structure showed in Figure 3.5 (a), the absorber shows a fine grains structure with 580nm thickness. Figure 3.5 (b) shows the spin-coating absorber layers with different thickness of in V5-X-560(Ar) series samples. An attempt was made by using different numbers of spin-coating runs from 3 layers to 9 layers and it shows a linear dependence between the number of spin-coating runs and the thickness of the absorber after the annealing process. Extrapolating from the results, the thickness of each layer is approximately 100-120 nm.

Table 3.2 and Figure 3.6 show the detailed information about the photoconversion performance of samples with different spin-coated layers, the J-V curves and external quantum efficiency characteristics. The best efficiency is 8.57% with 5 spin-coating layers, much higher than that of the other samples. Among the most notably, the short-circuit current density of sample with 5 layers reaches up to 33.81 mA/cm^2 . If the absorber of CISSe solar cells is too thin, it will directly bring the loss of the short-circuit current, although the loss was not only due to a reduced absorbance [133]. By contrast, much more defects can exist in a thick absorber, which leads to increased recombination of charge carriers. As a result, there is an optimum thickness of the absorber in CISSe thin film solar cells. However, the grain growth at 560°C is still insufficient to transform the layered structure of the precursor induced by repeated cycles of spin-coating and pre-heating treatment to a sufficiently thick, continuous and large grained absorber film. Therefore, we still need to increase the efficiency by optimizing the annealing temperature profile.

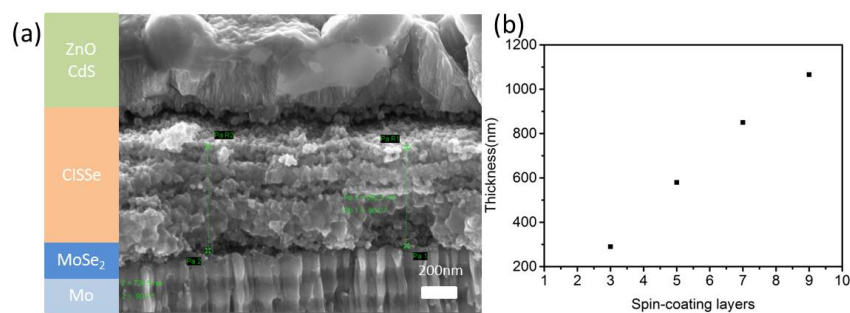


Figure 3.5 (a) SEM cross section image of sample V5-5-560(Ar); (b) spin-coating layers dependent thickness of the absorber in V5-X-560(Ar) series samples.

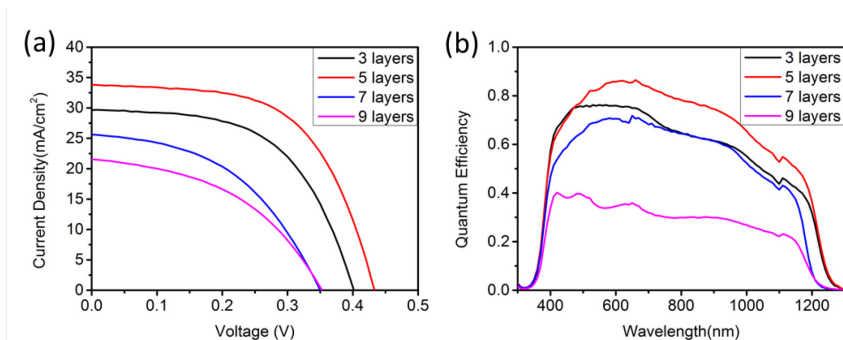


Figure 3.6 (a) the J-V curves and (b) external quantum efficiency characteristics of the CISSe solar cells with different spin-coating layers.

Table 3.2 Comparison of Open-Circuit Photovoltage (V_{oc}), Short-Circuit Photocurrent Density (J_{sc}), Fill Factor (FF), and Photoconversion Efficiency (η) for samples with different spin-coating layers.

| Cell(Cu:In=0.9) | V_{oc} (mV) | J_{sc} (mA/cm ²) | FF (%) | η (%) |
|---------------------|---------------|--------------------------------|--------|------------|
| CISSe(V5-3-560(Ar)) | 401.6 | 29.66 | 56.2 | 6.69 |
| CISSe(V5-5-560(Ar)) | 433.4 | 33.81 | 58.5 | 8.57 |
| CISSe(V5-7-560(Ar)) | 350.1 | 25.65 | 46.3 | 4.16 |
| CISSe(V5-9-560(Ar)) | 352.8 | 21.56 | 44.9 | 3.41 |

3.2.3 Annealing treatment

On the one hand, in order to reduce the defects existing in the fine grains of the absorber layer and insufficient selenization, changing the annealing process by introducing the additional annealing step at 580°C can be an effective method for enlarging grains. On the other hand, it should be discussed whether sulfur from thiourea in molecular ink introduced in films or annealing with H₂S gas can enhance this process. Figure 3.7 (a) and (b) show the XRD patterns of the completed CISSe solar cells with different annealing treatment. Both samples experience a heating program: 400°C for 20 min under argon atmosphere, 560°C for 20 min under argon atmosphere. Sample V5-6-580(Ar) (red line) continue another 5min at 580°C under argon atmosphere, while sample V5-6-580(H₂S) (black line) 5min at 580°C under H₂S atmosphere. From the XRD patterns, both of them have the CuInSe₂ structure with lattice constants of $a = 5.782 \text{ \AA}$ and $c = 11.619 \text{ \AA}$ (JCPDS card 40-1487). The maximum intensity peak located at 26.68° of sample V5-6-580(Ar) corresponds to the CISSe (112) plane, while the pure CuInSe₂ (112) orientation peak is located at 26.578°. The reason why the peak position is shifted to a higher degree is that sulfur was incorporated into the crystal lattice. The pure CuInS₂ (112) orientation peak is located at 27.902° (JCPDS card 47-1372). This phenomenon is more pronounced for sample V5-6-580(H₂S) with the (112) orientation peak at 26.98° between pure CuInSe₂ and pure CuInS₂ because of the presence of H₂S during the annealing process. From the SEM cross section images of 580°C annealing samples in Figure 3.7

(c) and (d), it can be seen that under high temperature the grains now grew across the precursor layer boundaries and it formed larger grains in the absorber layers than the 560°C annealing samples, which can reduce defects between the fine grains surface.

Table 3.3 and Figure 3.8 display the detailed photoconversion performance of samples treated by different annealing processes. It can be seen that both samples have similar open-circuit voltage, but the short-circuit current density of sample V5-6-580(Ar) with $35.43\text{mA}/\text{cm}^2$ is much higher than sample V5-6-580(H₂S) with $25.79\text{mA}/\text{cm}^2$. Owing to the annealing process with H₂S, the current density was reduced. Also from the external quantum efficiency characteristics, the sample V5-6-580(Ar) reaches up to 94% at 650nm wavelength, much higher than sample V5-6-580(H₂S) with 82%. Furthermore, the external quantum efficiency spectrum of the Ar sample is wider than that of the H₂S sample; the band gap of the Ar sample absorber is estimated to be 1.02 eV, lower than the 1.15 eV of H₂S sample. To make low band-gap CuIn(S, Se)₂ thin film solar cells is very important for applying them as bottom cells in tandem devices. This is especially important for current matching between perovskite solar cells as top cells and chalcopyrite thin film solar cell with a low band-gap of 1.0 eV as bottom cells [128].

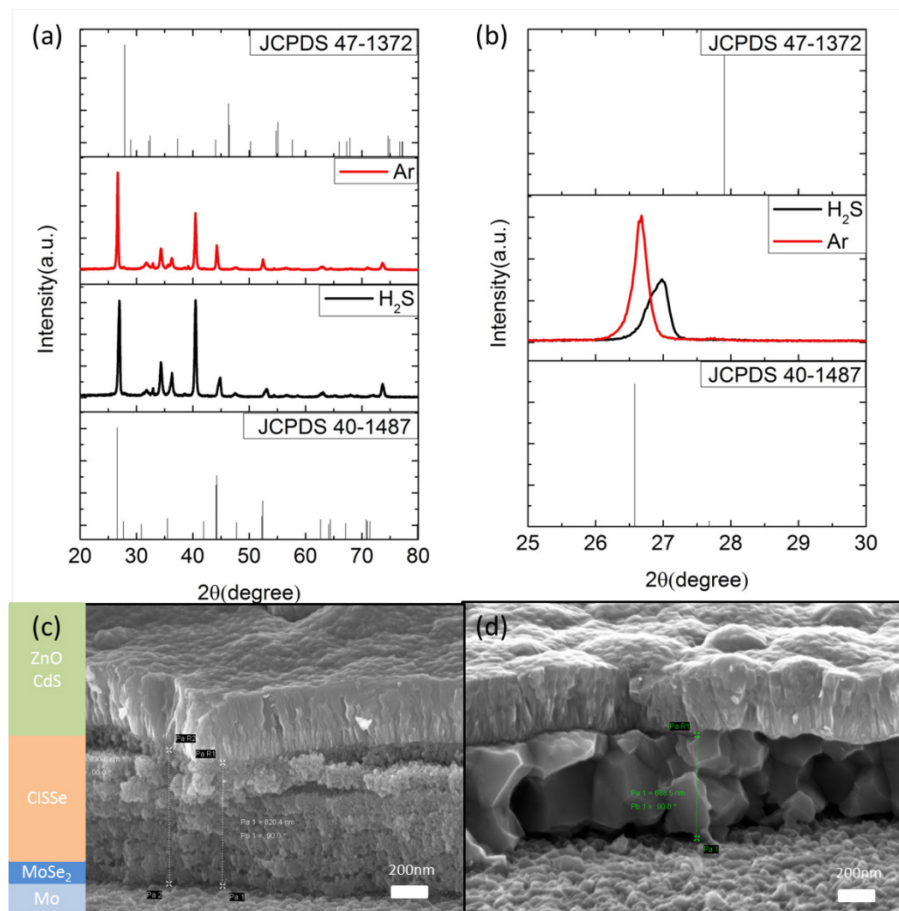


Figure 3.7 (a) the XRD patterns and (b) detailed XRD patterns of the CISSe solar cells with different annealing process: sample V5-6-580(Ar) (red line) and V5-6-580(H₂S) (black line). SEM cross section images of (c) sample V5-7-560(Ar) and (d) sample V5-7-580(H₂S).

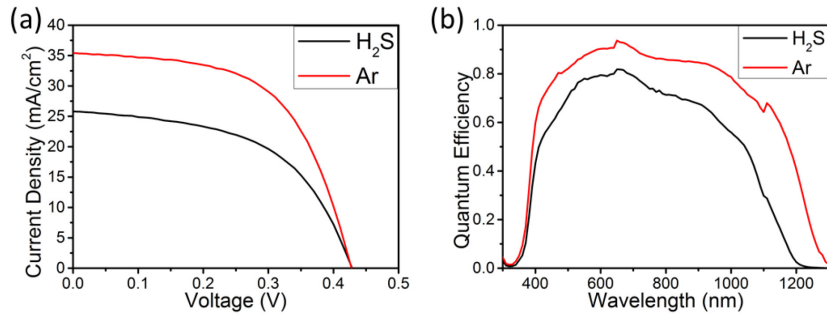


Figure 3.8 (a) the J-V curves and (b) external quantum efficiency characteristics of the CISSe solar cells with different annealing process.

Table 3.3 Comparison of Open-Circuit Photovoltage (V_{oc}), Short-Circuit Photocurrent Density (J_{sc}), Fill Factor (FF), and Photoconversion Efficiency (η) for samples with different annealing process.

| Cell(Cu:In=0.9) | V_{oc} (mV) | J_{sc} (mA/cm ²) | FF (%) | η (%) |
|-----------------------------------|---------------|--------------------------------|--------|------------|
| CISSe(V5-6-580(H ₂ S)) | 428.7 | 25.79 | 53.3 | 5.89 |
| CISSe(V5-6-580(Ar)) | 427.8 | 35.43 | 57.5 | 8.71 |

3.2.4 The effect of Na in the precursor solution

It is well known that introducing sodium into CIGSe thin-film photovoltaic devices can boost the efficiency of the device [134-136]. However, the mechanism of Na improving the performance of CIGSe solar cells is still not clear. Some authors fabricated devices on a glass substrate containing Na, claiming that Na only acts during the growth of the CIGSe [137]. Others found a similar improvement using a post-treatment of Na [138]. So adding Na in the precursor solution was also tried to see whether it can enhance the efficiency.

Figure 3.9 shows the J-V curves and external quantum efficiency characteristics of the CISSe solar cells with Na under the same treatment conditions. Na in the precursor solution can increase current density and open-circuit voltage greatly. Compared to the sample without Na, the CISSe solar cell with Na treatment achieves 8.86% efficiency with 496.1 mV of V_{oc} and 29.86 mA/cm² of J_{sc} , which is four times higher than 2.11% efficiency of the sample without Na treatment. As shown in Figure 3.9 (b), the external quantum efficiency reaches up to 88% at 650nm wavelength.

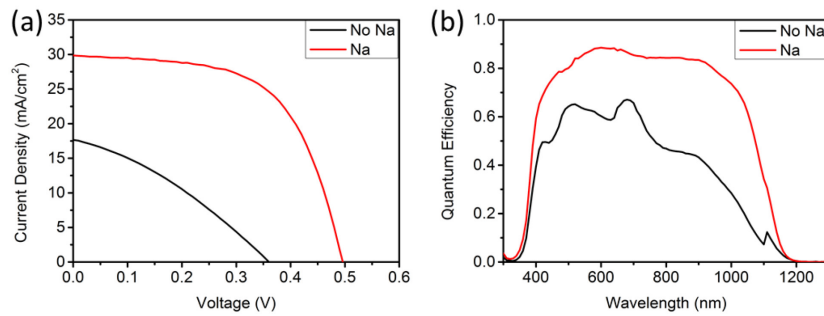


Figure 3.9 (a) J-V curves, (b) external quantum efficiency characteristics of the CISSe solar cells with Na treatment.

In order to know whether a Na treatment can increase the efficiency of the cell with the best optimization including solvent, absorber thickness and annealing process, the absorber thickness of samples with Na in the precursor was varied. From figure 3.10 and table 3.4, which is the detailed information about photoconversion performance of Na treatment samples with different spin-coating layers, the best efficiency is 9.54% with 9 spin-coating layers, much higher than other samples. As we discussed in 3.2.2, if the absorber of CISSe solar cells is too thin, it will directly bring the loss of the short-circuit current. By contrast, much more defects exist in the thick absorber, increasing the recombination of charge carriers. As a result, there is an optimum layer thickness for spin-coated CISSe thin film solar cells. But the best efficiency of absorber thickness variation is quite similar to the champion cell without Na treatment (see below 3.2.5), indicating Na couldn't enhance efficiency greatly when the solar cell optimized. Figure 3.10 (b) shows the XRD patterns of the CISSe solar cells with Na treatment with different numbers of spin-coated layers. All of them have the CuInSe_2 structure with lattice constants of $a = 5.782 \text{ \AA}$ and $c = 11.619 \text{ \AA}$ (JCPDS card 40-1487), which suggests that adding Na in the precursor solution does not change the CuInSe_2 structure. The main peaks including (112), (204), (220) orientation can be observed.

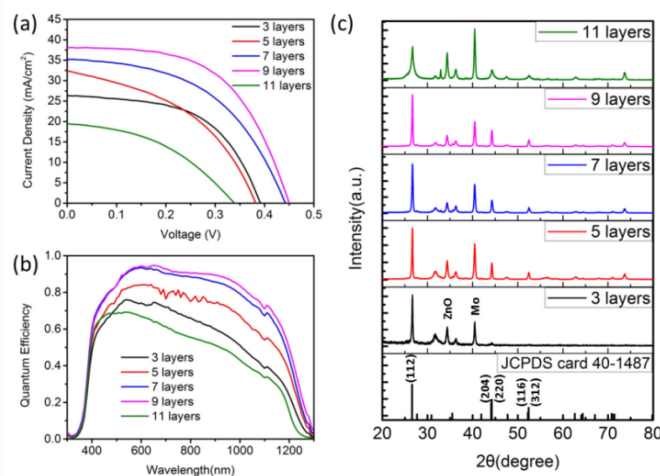


Figure 3.10 (a) the J-V curves, (b) external quantum efficiency characteristics and (c) the XRD patterns of the CISSe solar cells with Na varied by absorber thickness.

Table 3.4 Comparison of Open-Circuit Photovoltage (V_{oc}), Short-Circuit Photocurrent Density (J_{sc}), Fill Factor (FF), and Photoconversion Efficiency (η) for samples with Na varied by absorber thickness.

| Cell(Cu:In=0.9) | V_{oc} (mV) | J_{sc} (mA/cm ²) | FF(%) | η (%) |
|-----------------|---------------|--------------------------------|-------|------------|
| CISSe(3) | 391.4 | 26.34 | 54.8 | 5.65 |
| CISSe(5) | 382.2 | 32.40 | 43.7 | 5.42 |
| CISSe(7) | 442.2 | 35.17 | 49.6 | 7.71 |
| CISSe(9) | 449.9 | 38.06 | 55.7 | 9.54 |
| CISSe(11) | 339.4 | 19.50 | 42.0 | 2.78 |

Figure 3.11 (a) shows temperature dependent open circuit voltages. The sample is the device with the best efficiency, while the PCE and V_{oc} shown in the figure are lower at room temperature because it is not a standard test condition (the light intensity less than 100 mWcm⁻²). As we discussed in the previous chapter (section 1.2.3), the activation energy E_a is 0.75 eV, which is much lower than the observed band gap of 1.02 eV. In this case, the value of E_a is smaller than the band gap of the absorber, indicating that the dominant recombination is located at the interface of the heterojunction [41, 42]. Figure 3.11 (b) shows the evolution efficiencies with temperature. The efficiency greatly increases until a temperature of 150 K.

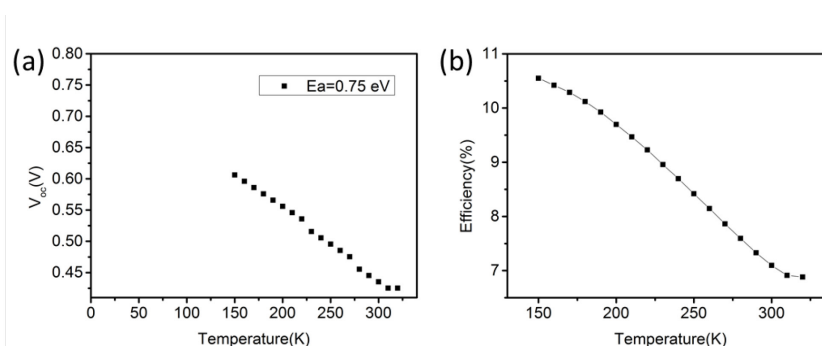


Figure 3.11 The best efficiency of CISSe thin film solar cell with Na treatment (a) temperature dependent open circuit voltages; (b) evolution of efficiencies with temperature (not a standard test condition: the light intensity less than 100 mWcm⁻²).

3.2.5 Champion cell

In the previous sections the impact of different factors on the efficiency of the resulting devices was shown. In this part the optimization of the CIGSe was described to achieve the maximum efficiency. From what has been discussed above, first, when adding the solvent ethylene glycol butyl ether into the precursor solution, it can enhance the wetting behavior of the molecular ink on the substrate and make films of CISSe solar cells more homogeneous. Second, varying the thickness of the absorber layer generates more charge carriers in terms of theory and increases short-circuit current density directly. Third, thiourea from molecular ink can

introduce sulfur into CISE solar cell by replacing Se with S. It is a simple way to introduce sulfur instead of annealing under H_2S atmosphere which is toxic and dangerous on operation. To sum up, the photoconversion performance of champion cell is showed in Figure 3.12. The best solar cell with 9.49% efficiency is achieved with higher short-circuit current density 38.77 mA/cm^2 and open-circuit voltage 442.1mV. As shown in Figure 3.12 (b), the external quantum efficiency reaches up to 92% at 650nm wavelength. From the SEM cross section image, inset, large grains layer with approximately 500nm thickness can be seen. Figure 3.12 (c) shows temperature dependent open circuit voltages. The sample is champion cell, while the PCE and V_{oc} shown in the figure are lower at room temperature because it is not a standard test condition (the light intensity less than 100 mWcm^{-2}). From this curve, it can be seen the activation energy E_a is 0.94 eV, which is slightly lower than the observed band gap of 1.02 eV for the champion cell. In a general sense, if the value of E_a equals to the band gap of the absorber, then the dominated recombination pathways is situated in the bulk of the absorber; while the value of E_a is smaller than the band gap of the absorber, the dominated recombination is located at the interface of the heterojunction [41, 42]. Figure 3.12 (d) shows the evolution of the efficiencies with temperature. The efficiency greatly increases until a temperature of 190 K. When the temperature is under 190 K, the efficiency is decreasing owing to the high series resistance at low temperature [42].

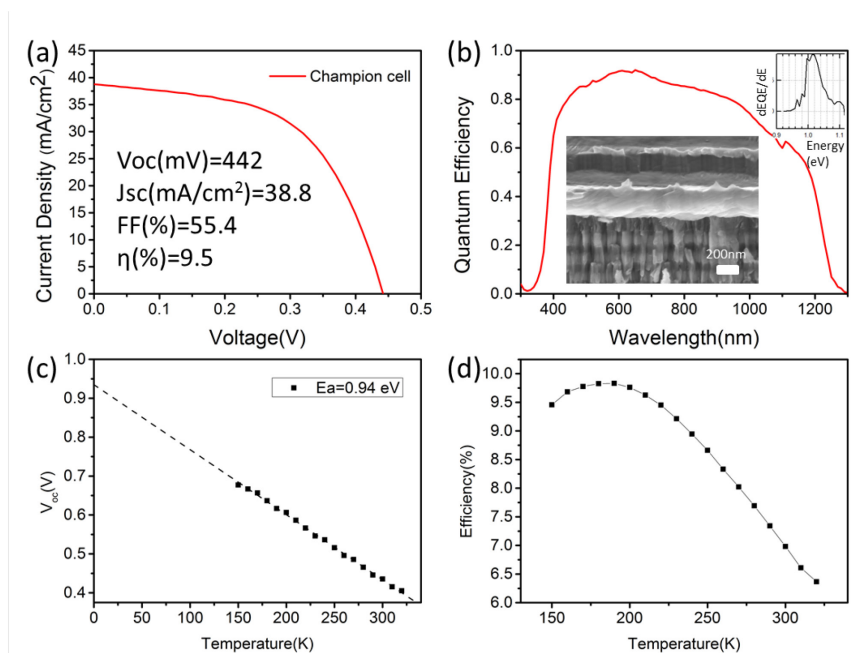


Figure 3.12 The best efficiency of CISSe thin film solar cell (a) J-V curve; (b) external quantum efficiency characteristics and SEM cross section image (inset); (c) temperature dependent open circuit voltages; (d) evolution of efficiencies with temperature (not a standard test condition: the light intensity less than 100 mWcm^{-2}).

3.3 Summary and outlook

A non-vacuum simple direct solution coating approach for $CuIn(S, Se)_2$ absorber thin

film solar cell was investigated, introducing a low cost and environmentally friendly molecular ink containing copper chloride, indium chloride, thiourea as precursors, and ethanol, ethylene glycol and ethylene glycol butyl ether as solvents. On the one hand, the ethylene glycol butyl ether as solvent contributed to improve the homogeneity of the absorber film. On the other hand, thiourea from the molecular ink can introduce sulfur into CISE solar cell by replacing Se with S without using toxic and hazardous H₂S gas. By means of varying the thickness of the absorber, it can directly increase short-circuit current density. Adding Na in the precursor solution was also tried to improve champion cell efficiency, but the effect is not prominent. Finally, a low band-gap (1.02 eV) CuIn(S, Se)₂ thin film solar cell fabricated by the absorber film prepared by this route was reported and exhibited an efficiency of 9.5% under AM 1.5 illumination. The dominant recombination mechanism in the solar cell is the absorber bulk recombination.

As bottom cell for tandem devices CuIn(S, Se)₂ prepared by molecular ink exhibits appropriate narrow band gap, low cost and simple fabricating process, however, the photoconversion efficiency is insufficient to match with perovskite top cell which has a PCE over 15%. In order to reach a higher efficiency, there are more possible improvements we can make efforts. First, in the above operations, spin-coating with pre-heating and repeated cycles several times were used. During every step, much more impurities would be introduced by man-made operations, which have influence on the quality of absorber films. Using inkjet printing method by printer can reduce this kind of human error and more easily form homogeneous absorber films, reaching high efficiency [33]. Another possibility to improve device performance is the optimization of the precursor properties (composition, structure). The copper and indium ratio was fixed at 0.9, which means copper poor. The atom ratio of CuIn(S, Se)₂ has a significant impact on the device performance [139]. Adjusting annealing steps is also one way to enhance photovoltaic efficiency. The grain growth and defects generation are strongly dominated by annealing steps. A higher temperature annealing step was added to grow large grains, while more complicated multistage annealing process can be applied to the fabrication according to the need of grain growth model. Therefore, there is still room for improving solar cell efficiency and performance.

4 P-type Cu_2O as an intermediate transparent conducting layer for monolithic perovskite-CIGSe tandem solar cells

This chapter is mainly based on the following publication:

Wang, Y., Steigert, A., Yin, G., Parvan, V., Klenk, R., Schlatmann, R., & Lauermaun, I. (2017). Cu_2O as a Potential Intermediate Transparent Conducting Oxide Layer for Monolithic Perovskite-CIGSe Tandem Solar Cells. *physica status solidi (c)*, 14(10).

4.1 Background

Photovoltaics have achieved great progress in obtaining high efficiency with diverse materials, e.g., silicon solar cells [140, 141], thin film chalcopyrite solar cells [33, 34, 142, 143], or perovskite solar cells [55, 129, 144]. According to the Shockley-Queisser (S-Q) efficiency limit of 33.7% for an optimum semiconductor band gap of 1.34 eV [13], much work has been devoted to approach the S-Q theoretical limit [14]. The S-Q limit is optimal compromise between current and voltage for single-junction photovoltaic devices, which the efficiency loss is mainly attributed to transmission and thermalization losses [14] caused by fundamental optical responses of semiconducting absorbers [16]. In order to enhance light harvesting and reduce thermalization losses, using two or more absorbers with different band gaps is an effective way to improve photovoltaic device performance [16, 145].

As described in the introduction chapter, a tandem solar cell normally consists of a bottom cell based on prevailing solar cell techniques e.g., silicon (Si) or $\text{Cu}(\text{In}, \text{Ga})(\text{Se}, \text{S})_2$ (CIGSe) with narrow band gap, and a top cell with a wider band gap absorber [63]. Manufacturing a two-terminal tandem device was found to be a more environmentally friendly option than four-terminal tandem solar cells and can reduce the environmental impacts by 30% due to the exclusion of extra glass, encapsulation, front contact and back contact layers [21]. In the monolithic or 2-terminal configuration, which is electrically connected in series, the current of the device is limited by the cell with the lower photocurrent.

So far, except for a-Si/ $\mu\text{c-Si}$ devices with a maximum efficiency around 14%, monolithic tandem solar cells have not been successfully manufactured using amorphous or polycrystalline thin film materials because of the absence of suitable top cell candidates which generate high photocurrents compatible with the bottom cell [18]. This situation has been changed by the advent of the so-called perovskite solar cells (PVK) [55, 57, 146] based on methyl ammonium lead halides. However, to realize the monolithic tandem concept using a CIGSe bottom cell and a PVK top cell, an intermediate transparent conducting layer that also serves as one component of the tunnel junction connecting the two single devices and as inorganic hole transport

layer for the PVK solar cell is important [103]. Figure 4.1 shows a schematic structure of two-terminal perovskite-CIGSe tandem solar cells.

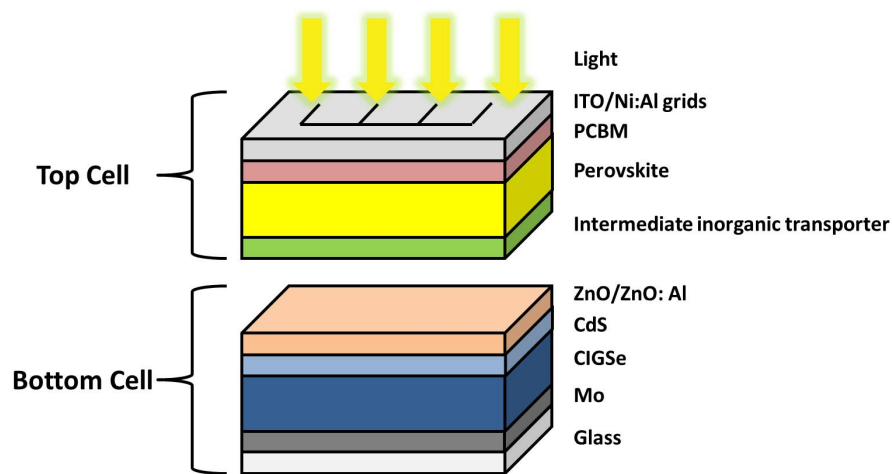


Figure 4.1 Structure of two-terminal perovskite-CIGSe tandem solar cells.

Cuprous oxide (Cu_2O), which is a low cost, nontoxic, abundant material is a p-type semiconductor with a direct band gap of ~ 2.1 eV and a work function of -5.4 eV and it exhibits a Hall mobility exceeding $100 \text{ cm}^2\text{V}^{-1}\text{s}^{-1}$ [147-149]. Cu_2O was used as a hole transport layer (HTL) in perovskite solar cells, on account of its good energy level alignment with methyl ammonium lead halides [150].

Remarkably, Liming Ding *et al.* [118] developed a novel chemical method to prepare Cu_2O films at low temperature, which was used in perovskite solar cells as HTL and achieved 13.4% efficiency. Also Cu_2O -based perovskite solar cells present better device stability than standard PVK with organic HTL. Based on the solution method, Zuqiang Bian and his co-workers [98] used a facile solution-processing method to introduce a CuO_x layer into a planar inverted perovskite solar cell and achieved a PCE over 17%. A higher efficiency of 19.0% was obtained by their group with CuO_x -based inverted $\text{CH}_3\text{NH}_3\text{PbI}_{3-x}\text{Cl}_x$ solar cells with an effective Cl doping method [151]. Apart from the low temperature solution method, Nejang *et al.* [152] prepared Cu_2O as a HTL in perovskite solar cells by magnetron sputtering, reaching a PCE of 8.93%. To understand potentials of various inorganic semiconductors applied to perovskite solar cells, M. I. Hossain *et al.* [153] used wxAMPS and SCAPS software to compute the photovoltaic performance of perovskite solar cells with various HTL layers including spiro-OMeTAD, NiO, Cu_2O , CuI and CuSCN, the results of which showed that Cu_2O -based solar cells outperform all other devices with organic or inorganic hole transporters hitherto tested, exceeding 24% efficiency.

However, there are only few publications on applying Cu_2O to combine perovskite and CIGSe solar cells [103]. Therefore, considering that the properties of Cu_2O satisfy the requirements of being an intermediate layer for monolithic perovskite-CIGSe tandem solar cells, p-type Cu_2O is a very promising intermediate material to achieve high efficiency perovskite-CIGSe tandem device. In this chapter, first Cu_2O films were prepared at room temperature by magnetron sputtering. A metallic Cu target was

used to deposit thin films by reactive sputtering in an oxygen-containing gas mixture with varying oxygen content. However, the conductivity of the resulting Cu_2O thin films was not very good. In order to achieve Cu_2O thin films with high conductivity, Cu_2O films were deposited from a CuO target in the presence of nitrogen to achieve p-doping. They were investigated by UPS to determine the band positions with respect to that of methyl ammonium lead halides. Unfortunately, the sputtered Cu_2O sample showed a bad wetting behavior in combination with perovskite precursor layers and also led to the degradation of the deposited perovskite. Therefore, a wet-chemical method was tried to prepare Cu_2O films and apply those to the single junction PVK solar cells, obtaining over 9% PCE.

4.2 Results and discussion

4.2.1 Sputtering method with oxygen variation

First, Cu_2O films were deposited on glass substrates using reactive sputtering, from a Cu metal target with O_2/Ar as working gas. In order to control the oxygen flow during the whole deposition, the concentration of oxygen in the O_2/Ar mixture was 5% and the O_2/Ar mixture flow rate was varied between 20 sccm and 100 sccm. Figure 4.2 shows XRD patterns of the Cu_xO samples varied by different working gas flow rates. The Cu_xO sample prepared with 50 sccm O_2/Ar mixture flow has the cubic Cu_2O structure with lattice constants of $a = b = c = 4.269 \text{ \AA}$ (JCPDS card 99-0041). The main peaks with (111), (200), (220), (311) orientations can be observed. The Cu_xO sample with 60 sccm O_2/Ar mixture flow exhibits a Cu_4O_3 structure (JCPDS card 83-1665) and the 70 sccm sample shows a transition phase from Cu_4O_3 to CuO , respectively. Both the Cu_4O_3 (202) and (220) diffraction peaks and the CuO (111) diffraction peak can be observed. These results suggest that using a lower oxygen flow can effectively form a high purity Cu_2O cubic structure. Increasing the oxygen flow, the Cu_xO film transforms to copper oxide compounds with higher oxygen/copper atomic ratio.

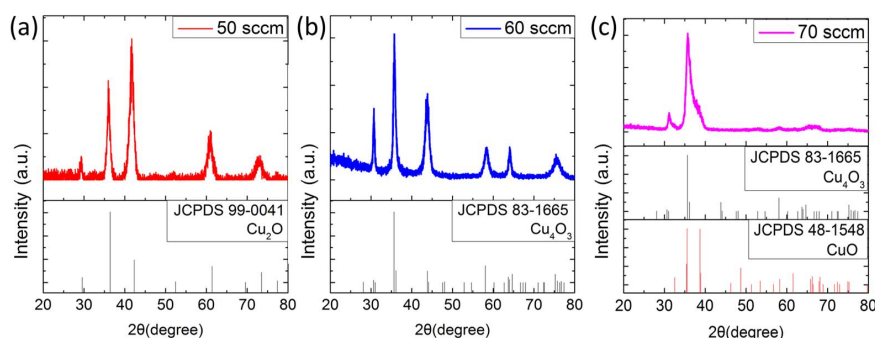


Figure 4.2 XRD patterns of Cu_xO samples with different O_2/Ar mixture flow rates: (a) 50 sccm; (b) 60 sccm; (c) 70 sccm.

Figure 4.3 shows UV-Vis transmission, reflection, and absorption spectra of the Cu_2O sample with 50 sccm O_2/Ar mixture flow, which is around 200nm thick. It presents around 70% transparency in a large wavelength range (500–1500 nm), which will be

higher for thinner Cu_2O films. It presents good optical properties as intermediate layer in tandem applications, since it allows more low energy photons to pass through to the CIGSe bottom cell. It also shows an appropriate optical band gap.

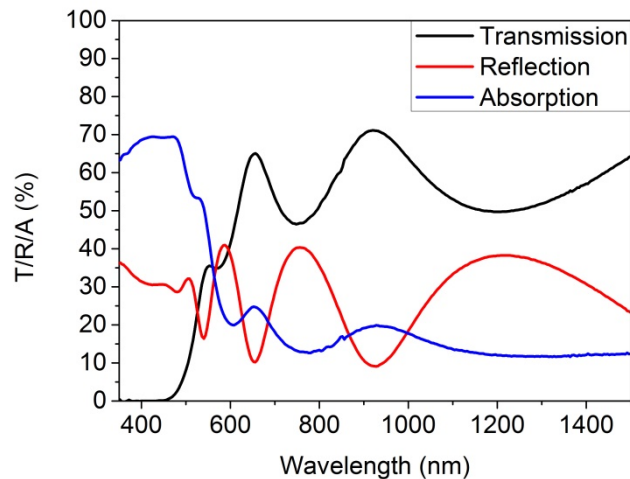


Figure 4.3 UV-Vis transmission spectra, reflection spectra and absorption spectra of the 200 nm thick Cu_2O sample with 50 sccm O_2/Ar mixture flow.

In order to determine the electrical properties of the Cu_2O films, which are important parameter for a hole transport material and tunnel junction component in tandem solar cells, the sheet resistance (Ω/sq) of Cu_xO films in dependence on the oxygen flow was investigated. From Figure 4.4, we can see the variation of electrical properties that could be divided into three stages with the increase of oxygen flow. During the first stage, the square resistance of the Cu_xO film increases strongly from 3 to $9.4 \times 10^9 \Omega/\text{sq}$ with the increase of oxygen flow because below 45 sccm the film includes well-conducting copper metal and Cu_2O phases. After the film completely transforms to the Cu_2O phase above 50 sccm, the electrical properties saturate and the square resistance is around $3.6 \times 10^6 \Omega/\text{sq}$. In the literature, similar resistivity of Cu_2O was reported around $10^2 \sim 10^4 \Omega \cdot \text{cm}$ [154], which equals the square resistance of $5 \times 10^6 \sim 5 \times 10^8 \Omega/\text{sq}$ for the 200 nm thick films. With continually increasing the oxygen flow, the film totally transforms to CuO and the square resistance continues to increase again. The sheet resistance is not an immediate concern as current is not transported laterally in the intermediate contact layers of a tandem cell. It does, however, indicate low effective doping which may make it difficult to make a quasi-ohmic contact to the underlying AZO film. Therefore, the study was extended to include doped films.

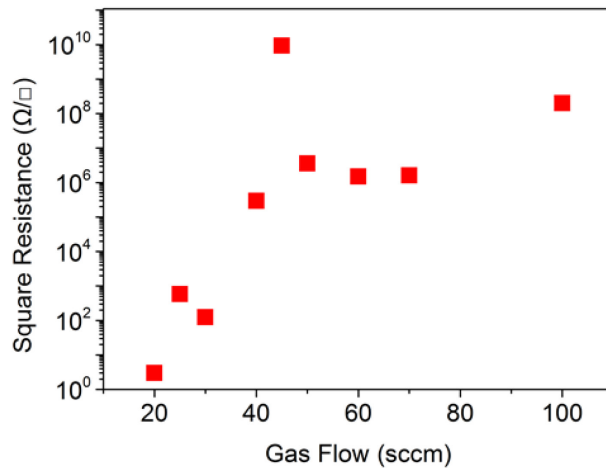


Figure 4.4 O₂/Ar mixture flow dependent square resistance of Cu_xO samples.

4.2.2 Sputtering of nitrogen doped Cu₂O

N-doped Cu₂O films were deposited on glass substrates with a ceramic CuO target and N₂/Ar as working gas by magnetron sputtering system. The N₂/Ar mixture flow was fixed at 50 sccm and varied the N₂ content in the gas mixture. XRD patterns of Cu_xO samples deposited with different nitrogen concentration in the flow gas are shown in Figure 4.5. With the increase of the N₂ content, the pure Cu₂O film shows a highly oriented (111) plane and a (200) peak appears gradually. Cu_xO samples with 20 and 50% N₂ have the cubic Cu₂O structure with lattice constants of $a = b = c = 4.269\text{\AA}$ (JCPDS card 99-0041). Cu₂O:N films retain the crystalline structure of single phase Cu₂O and no Cu₃N phase appears. It should be noted that the XPS overview spectrum, which will be explained in the following section shows no nitrogen signal, which limits the amount on nitrogen to a maximum of about 1 at.%. Therefore, the lattice is not expected to show any deviation from the pure Cu₂O lattice.

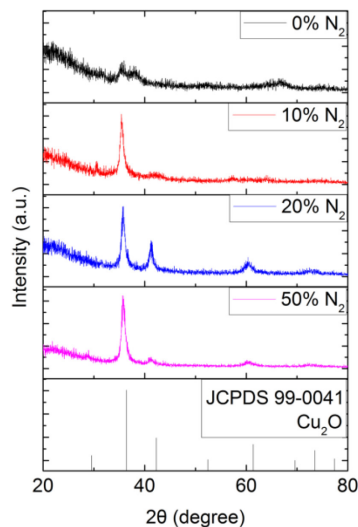


Figure 4.5 XRD patterns of Cu_xO samples with different N₂ content from 0% to 50% N₂ in the sputtering gas mixture.

Figure 4.6a–c show UV-Vis transmission, reflection, and absorption spectra of Cu_xO samples prepared with different N_2 percentages with around 100nm thickness. Cu_2O samples with 20% N_2 and 50% N_2 show better transparency in a large wavelength range (400–1500 nm) compared with other samples and an appropriate band gap. Figure 4.6 d shows the square resistance of Cu_xO samples dependent on N_2 percentage. The square resistance of the Cu_2O sample with 50% N_2 is $4.3 \times 10^5 \Omega/\text{sq}$, which is nearly one order of magnitude lower than that of the Cu_2O sample without N_2 doping ($3.6 \times 10^6 \Omega/\text{sq}$, shown in Figure 4.4), indicating that N_2 doping can effectively increase the conductivity of Cu_xO samples.

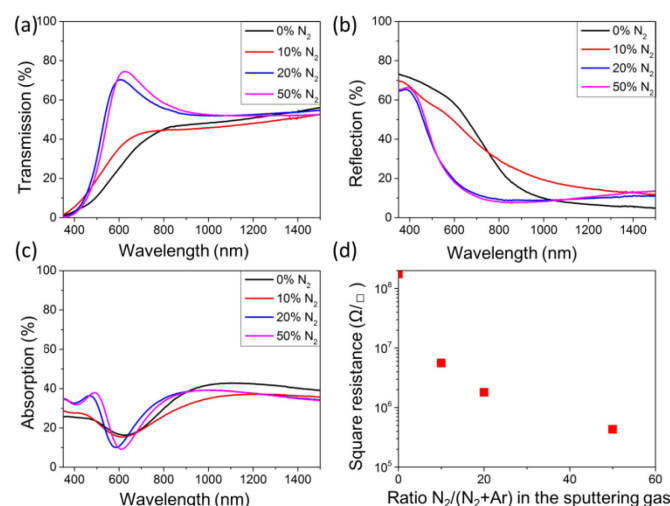


Figure 4.6 Cu_xO samples with different N_2 percentage content: (a) UV-Vis transmission spectra; (b) UV-Vis reflection spectra; (c) UV-Vis absorption spectra; (d) N_2 in N_2/Ar mixture content dependent square resistance.

To obtain the optical properties of Cu_2O , the in house software RefDex based on the transfer matrix method was applied and extracted optical constants n and k of our Cu_2O -50% N_2 sample from the measured reflection and transmission curves [104]. Figure 4.7 a and b show refractive index n and extinction coefficient k of the Cu_2O sample with 50% N_2 flow compared with a Cu_2O reference [155] and a perovskite reference [156]. It shows a high refractive index and low absorption. From the extinction coefficient k , the Cu_2O -50% N_2 sample exhibits a slightly increasing absorption in the infrared range. This is due to the N doping, which results in inter-band absorption [157]. The optical absorption coefficients can be calculated by [157]:

$$\alpha = 4\pi k/\lambda \quad (4.1)$$

According to the theory of energy bands, the value of E_g should be determined with the relationship by [158]:

$$\alpha^2 = hv - E_g \quad (4.2)$$

where hv is the incident photon energy. The E_g value of the Cu_2O -50% N_2 sample is

determined to be 2.45 eV as shown in Figure 4.7 c.

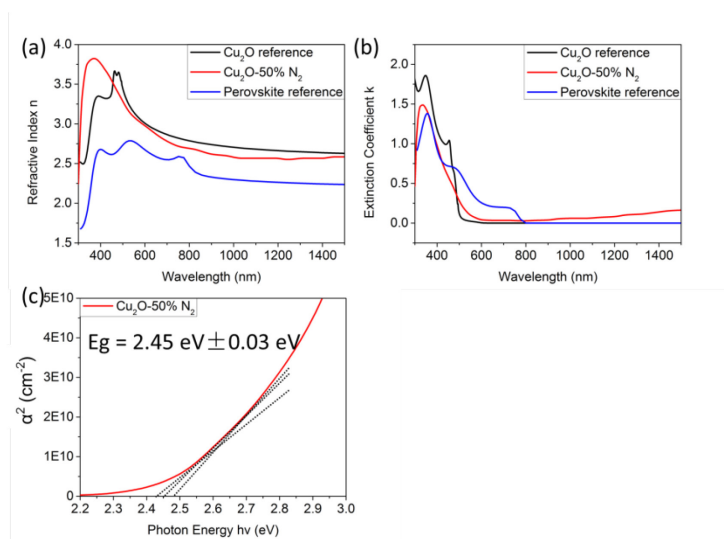


Figure 4.7 (a) Refractive index n ; (b) extinction coefficient k of the Cu_2O sample with 50% N_2 flow compared with the Cu_2O reference and the perovskite reference; (c) relationship of $\alpha^2 \propto (h\nu - E_g)$ for the Cu_2O sample with 50% N_2 flow.

X-ray photoelectron spectroscopy (XPS) was used to characterize the Cu oxidation state of the Cu_2O sample with 50% N_2 . As shown in Figure 4.8 b, the Cu spectra for the Cu_2O film shows a Cu $2p_{3/2}$ peak located at 932.2 eV, corresponding to the Cu^+ cation, while there is no Cu^{2+} peak located at 934.4 eV, [98] indicating that the 50% N_2 sample is pure Cu_2O . The O 1s peak located at 530.4 eV corresponds to the O^{2-} anion in Cu_2O . These values suggest the successful synthesis of a Cu_2O film. During the preparation process, we want to refrain from synthesizing CuO because its band gap (1.2 eV) is too narrow for perovskite-CIGSe tandem solar cells, as it would absorb part of the long-wavelength light before reaching the CIGSe bottom cell.

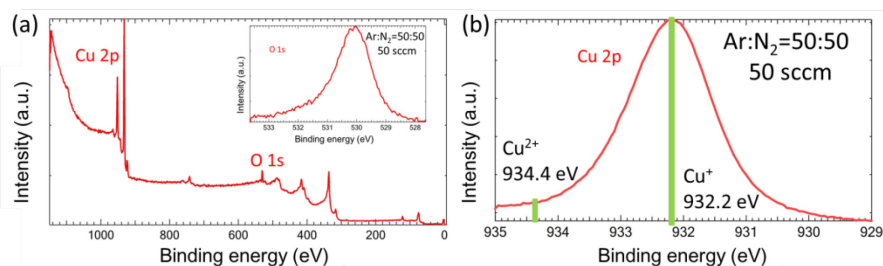


Figure 4.8 Cu_2O sample with 50% nitrogen: (a) XPS survey spectra (inset: high resolution XPS spectra of O 1s); (b) high resolution XPS spectra of Cu $2p_{3/2}$.

Figure 4.9a-c show the survey spectra, the valence band (VB) maximum and secondary electron edge of Cu_2O measured by ultraviolet photoelectron spectroscopy (UPS). The work function (WF) derived from the secondary electron edge (4.67 eV) was calculated and the valence band (VB) maximum has been determined to be 5.05 eV below the vacuum level. The band gap (E_g) was also calculated from optical constants, and used this value to calculate the conduction band (CB) minimum. The resulting energy diagram of the Cu_2O film is shown in Figure

4.9 d. As for the N-doped Cu_2O sample, N would substitute for O and create an ionized acceptor or defect between ECB and EVB; moreover, the p states of N could contribute to narrow down the band gap by mixing with O 2p states, which could enhance the electrical properties of Cu_2O films [159, 160].

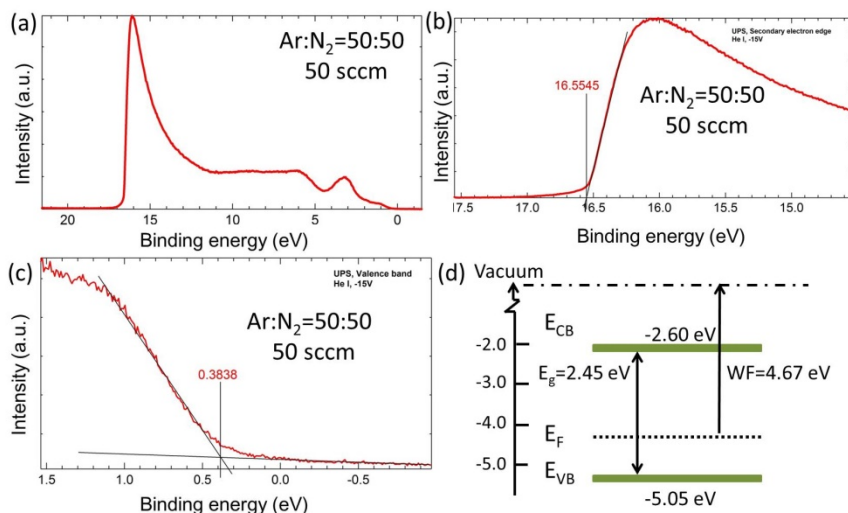


Figure 4.9 Cu_2O sample with 50% nitrogen: (a) UPS survey spectra; (b) secondary electron edge; (c) valence band maximum; (d) energy diagram relative to vacuum level.

In order to know whether our sputtered Cu_2O sample energy level matches with the other layers in a perovskite-CIGSe tandem solar cell device, a schematic architecture of the whole tandem device was investigated. Figure 4.10 a shows the schematic architecture of a perovskite-CIGSe tandem solar cell, consisting of Mo/CIGSe/CdS/ZnO/AZO/ Cu_2O / $\text{CH}_3\text{NH}_3\text{PbI}_3$ /PCBM/ITO/glass. $\text{CuInGa}(\text{S}, \text{Se})_2$ is used as absorber, CdS as buffer layer, i-ZnO and aluminum doped ZnO as window layers for the bottom CIGSe cell. For the top perovskite solar cell, Cu_2O and PCBM are applied as hole and electron transport layers, respectively. The intermediate tunnel junction consists of highly doped n^{++} aluminum zinc oxide (AZO) and p-type Cu_2O . A schematic energy diagram of the material in the device is presented in Figure 4.10 b. The valence band edge of the Cu_2O film is -5.05 eV, which is a little higher than the highest occupied molecular orbital (HOMO) energy level of the $\text{CH}_3\text{NH}_3\text{PbI}_3$ layer (-5.5 eV), thus leading to the extraction of holes at the interface between the Cu_2O and the $\text{CH}_3\text{NH}_3\text{PbI}_3$ film. In addition, the conduction band edge of the Cu_2O film (-2.60 eV) is much higher than the lowest unoccupied molecular orbital (LUMO) of the $\text{CH}_3\text{NH}_3\text{PbI}_3$ layer (-3.9 eV), which prevents electrons from reaching the perovskite effectively.

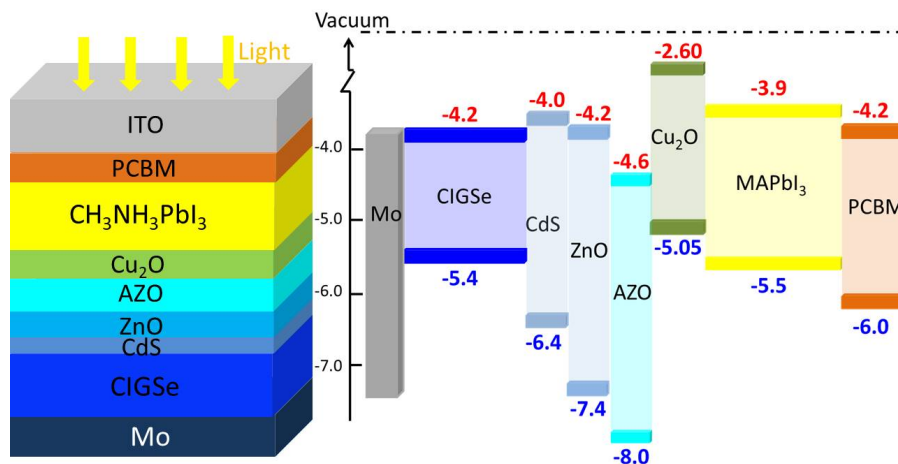


Figure 4.10 (a) Schematic of the device architecture of a monolithic perovskite-CIGSe tandem solar cell; (b) energy-level and structure diagrams of a perovskite-CIGSe tandem solar cell relative to vacuum level, values in red are conduction band minima, while values in blue are valence band maxima [98, 100-102, 161, 162].

In order to investigate the wetting behavior between a sputtered Cu_2O sample and a perovskite layer ($\text{CH}_3\text{NH}_3\text{PbI}_3$), perovskites were spin coated on the Cu_2O thin film. As shown in Figure 4.11 a, a very obvious degradation of the perovskite film after heating and the non-spreading behavior indicate that a chemical reaction between Cu_2O and perovskite takes place. This is probably because there are some active sites on the sputtered Cu_2O surface, easily reacting with perovskite, which results in the decomposition into lead iodide and methyl ammonium iodide.

4.2.3 Wet chemical deposition of Cu_2O

To avoid the degradation of the applied perovskite, a wet chemical deposition method was used to prepare Cu_2O thin films. In fact, considering that perovskite layers are normally prepared in a one-step solution process, preparing Cu_2O films also with a wet chemical approach makes it more compatible with the perovskite deposition. Figure 4.11 b shows the simple schematic diagram of the wet chemical approach, which consists of spin-coating a Cu precursor and subsequent evaporation of the solvent at a temperature of 80-120°C (detailed experimental description see chapter 2.1.1).

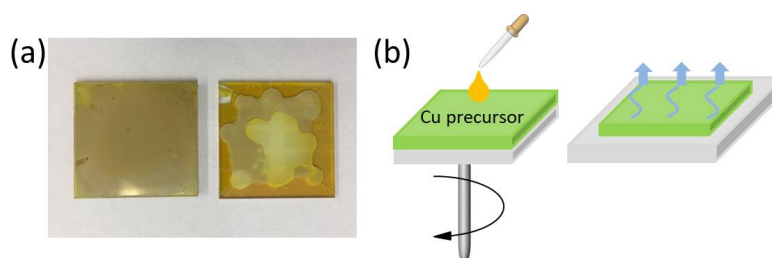


Figure 4.11 (a) Photograph of a spin-coated perovskite solution on the sputtered Cu_2O thin film (left: before spin-coating; right: after spin-coating); (b) schematic diagram of the wet chemical approach.

Figure 4.12 shows the X-ray photoelectron spectroscopy (XPS) of the Cu_2O sample deposited by the wet chemical approach. In Figure 4.12 c, the Cu spectra of the Cu_2O film shows Cu $2p_{3/2}$ and Cu $2p_{1/2}$ peaks, accompanied by shake-up satellites, which typically appear in Cu(II) compounds like CuO. Figure 4.12 d shows the detailed Cu $2p_{3/2}$ spectrum, which has maxima located at 932.2 eV and 934.4 eV, corresponding to the Cu^+ cation and Cu^{2+} , respectively [98]. It demonstrates that both CuO and Cu_2O are formed by the wet chemical approach, but fortunately the CuO appears only in a small concentration. The O 1s peak located at 530.4 eV corresponds to the O^{2-} anion in Cu_2O and CuO. The heating process after spin-coating mainly leads to the formation of CuO. High temperatures cause the oxidization of Cu_2O to CuO, while solvent evaporation and crystallization are not completed at lower heating temperature like below 80°C.

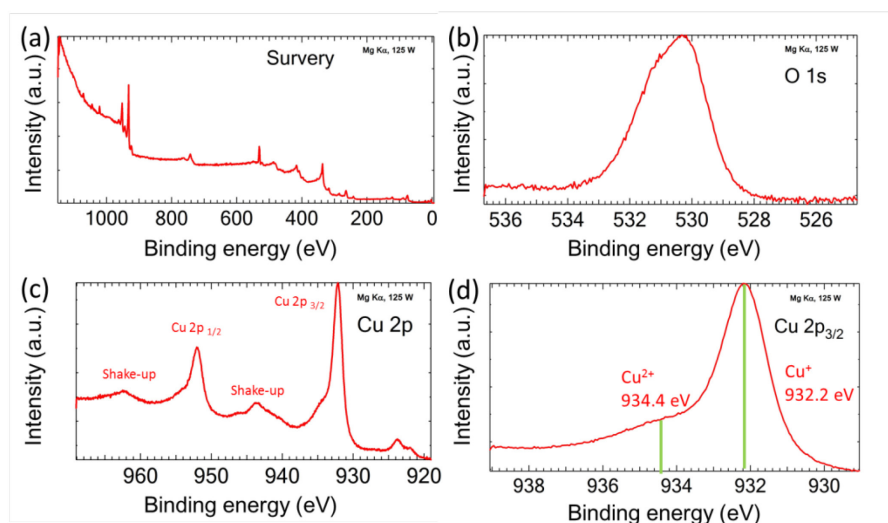


Figure 4.12 Cu_2O sample made by a wet chemical approach: (a) XPS survey spectra; (b) high resolution XPS spectra of O 1s; (c) high resolution XPS spectra of Cu 2p; (d) high resolution XPS spectra of Cu $2p_{3/2}$.

Optical properties were characterized by a ultraviolet–visible spectrophotometer (UV-Vis). Compared with glass, the Cu_2O sample made by the wet chemical approach shows similar high transparency and low reflection in a large wavelength range (300–1500 nm) as shown in Figure 4.13. The average transmission of wet chemical samples is 85%, much better than that of sputtered Cu_2O samples (55%).

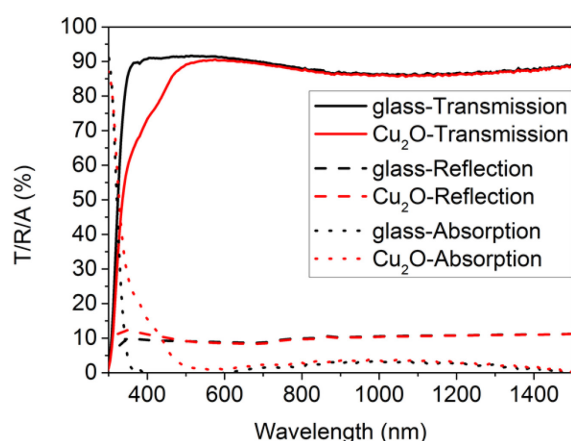


Figure 4.13 UV-Vis transmission spectra, reflection spectra and absorption spectra of the Cu_2O sample by wet chemical approach.

Owing to the thinness of Cu_2O film, the coverage is probably a significant influence factor to the performance of perovskite solar cells. Pinholes in the hole transport layer will increase the possibility of forming direct contact between perovskite and AZO, which probably cuts down the effective electron blocking and increases carrier recombination [163]. As shown in Figure 4.14 of SEM images of Cu_2O sample made by the wet chemical approach, the Cu_2O films have a nanoparticle structure surface, which provides a large interfacial area with perovskite and offers effective extraction of holes from the perovskite.

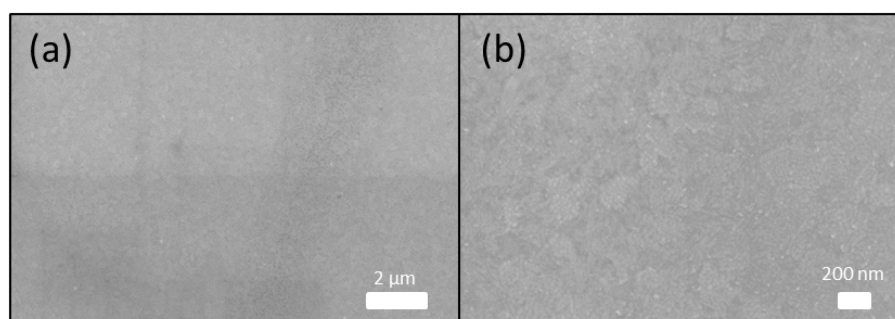


Figure 4.14 SEM images of Cu_2O sample made by the wet chemical approach at a magnification of (a) 20K X; (b) 100K X.

4.2.4 PVK cells

Figure 4.15 shows the J-V curves and external quantum efficiency (EQE) characteristics of single junction perovskite solar cells using Cu_2O as hole transport material with different annealing temperatures and $\text{CH}_3\text{NH}_3\text{PbI}_3$ as absorber. Table 4.1 shows the detailed performance parameters of these solar cells. 80°C , 100°C and 120°C are used as subsequent evaporation temperatures (detailed experimental description see chapter 2.1.1). As the temperature increases, open-circuit voltage and short-circuit current are both improved. The best efficiency with 9.66% and 0.93V open-circuit voltage and $16.6\text{mA}/\text{cm}^2$ short-circuit current density is achieved

by increasing the evaporation temperature to 120°C. These results indicate that Cu₂O indeed is suitable in perovskite solar cells as hole transport material, which is the first step for applying Cu₂O in perovskite-CIGSe tandem solar cells.

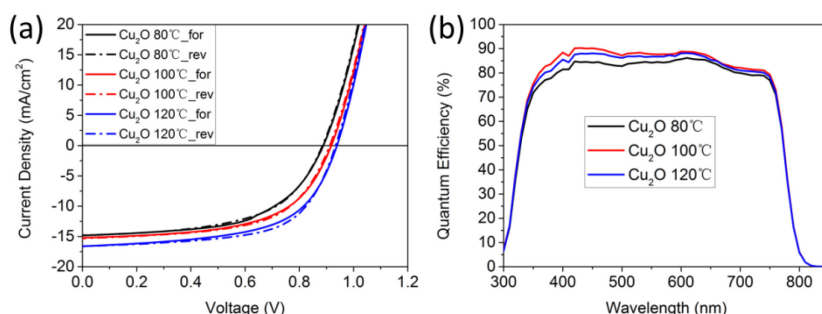


Figure 4.15 (a) The J-V curves and (b) external quantum efficiency characteristics of the single junction perovskite solar cells using Cu₂O as hole transport material with different annealing temperatures.

Table 4.1 Comparison of Open-Circuit Photovoltage (V_{oc}), Short-Circuit Photocurrent Density (J_{sc}), Fill Factor (FF), and Photoconversion Efficiency (η) for samples with different annealing temperature.

| Cells | V_{oc} (V) | J_{sc} (mA/cm ²) | FF (%) | η (%) |
|-----------------------------|--------------|--------------------------------|--------|------------|
| Cu ₂ O 80°C_for | 0.89 | 14.8 | 56.9 | 7.50 |
| Cu ₂ O 80°C_rev | 0.89 | 14.8 | 56.2 | 7.40 |
| Cu ₂ O 100°C_for | 0.92 | 15.2 | 57.9 | 8.08 |
| Cu ₂ O 100°C_rev | 0.91 | 15.3 | 59.2 | 8.27 |
| Cu ₂ O 120°C_for | 0.94 | 16.6 | 58.8 | 9.17 |
| Cu ₂ O 120°C_rev | 0.93 | 16.6 | 62.2 | 9.66 |

Considering that the process with which Cu₂O was deposited in a wet chemical approach still has room for improvement, some experimental operations were modified to make the sample surface cleaner and more homogeneous. As described in the experiment chapter, some samples were spin coated by 10 mg/mL aqueous NaOH solution and distilled water at 4000 rpm for 60 s three times, respectively, instead of being immersed in NaOH solution and rinsed with distilled water. Then the substrate was heated at 100°C for 20 min. The 100°C sample is taken as an example, J-V curves and external quantum efficiency are shown in Figure 4.16. Apparently, the short-circuit current density increases from 15.3 to 17.8 mA/cm² after improving the experimental process. The photoconversion efficiency was enhanced by 15% from 8.27% to 9.52% as shown in Table 4.2. These results demonstrate that Cu₂O is a promising material to achieve better efficiency and higher short-circuit current density, which are significant for current matching of the sub-cells in tandem solar cells.

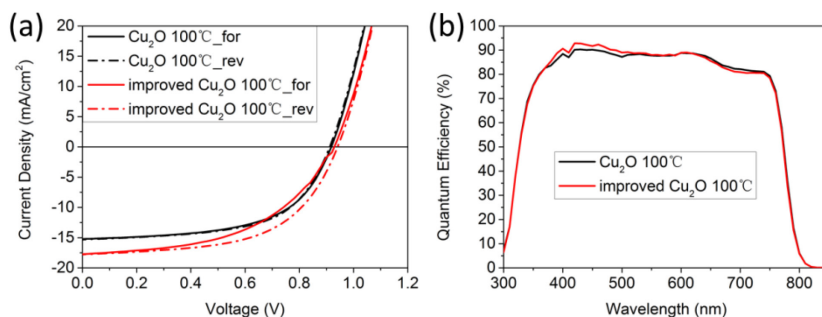


Figure 4.16 (a) The J-V curves and (b) external quantum efficiency characteristics of the single junction perovskite solar cells using Cu₂O as hole transport material with improved surface cleaning.

Table 4.2 Comparison of Open-Circuit Photovoltage (V_{oc}), Short-Circuit Photocurrent Density (J_{sc}), Fill Factor (FF), and Photoconversion Efficiency (η) for samples with improved surface cleaning and reference samples with PTAA.

| Cells | V_{oc} (V) | J_{sc} (mA/cm ²) | FF (%) | η (%) |
|--------------------------------------|--------------|--------------------------------|--------|------------|
| Cu ₂ O 100°C_for | 0.92 | 15.2 | 57.9 | 8.08 |
| Cu ₂ O 100°C_rev | 0.91 | 15.3 | 59.2 | 8.27 |
| Improved Cu ₂ O 100°C_for | 0.93 | 17.7 | 49.9 | 8.22 |
| Improved Cu ₂ O 100°C_rev | 0.94 | 17.8 | 56.9 | 9.52 |
| Reference cell | 1.08 | 19.2 | 78.3 | 16.21 |

4.3 Summary and outlook

P-type Cu₂O films were prepared at room temperature by magnetron sputtering using nitrogen doping, leading to high transparency and good conductivity. The electronic structure of Cu₂O was calculated and the energy levels of a monolithic perovskite-CIGSe tandem solar cell were investigated. Because of the bad wetting behavior and high degradation at the interface of the sputtered Cu₂O sample and perovskite layer, Cu₂O with extreme high transparency was prepared using a wet chemical approach to single junction perovskite solar cells and achieved over 9% photoconversion efficiency, indicating that the Cu₂O film opens new avenues for monolithic perovskite-CIGSe tandem solar cells as one component of the intermediate tunnel junction and that it also has the potential to achieve high efficiency photovoltaics devices.

A wet chemical method was tried, which works well with perovskite solar cells. Although the cell with over 9% of PCE prepared with the wet chemical technique shows that Cu₂O is a promising material as hole transport layer and intermediate tunnel junction component in the perovskite-CIGSe tandem solar cells, we still need to look for better preparation methods, which are easily operated. Wet chemical or spin-coating techniques usually have shortcomings, such as low-throughput,

individual errors, requiring truly soluble precursors and also forming low conductivity films. On the other hand, the reactive rf magnetron sputtering approach is established as the process of choice for the deposition of industrial coatings, which are wear-resistant, corrosion-resistant, have low friction, and good optical and electrical properties [164, 165]. Sputter-deposition also meets the requirement that we need to deposit the intermediate layer of tandem solar cells at low temperature in order not to destroy the bottom CIGSe solar cells. As a consequence, searching for other p-type semiconductors as hole transport layer and tunnel junction component by simple preparation techniques is a significant topic for perovskite-CIGSe tandem solar cells. Therefore, p-type CuGaO_2 is investigated in the next chapter.

5 P-type CuGaO_2 as an intermediate transparent conducting layer for monolithic perovskite-CIGSe tandem solar cells

5.1 Background

As we introduced in the last chapter, the fundamental performance limit of single junction photovoltaic devices was presented by Shockley and Queisser in 1961 [13, 14]. So far, silicon (Si) solar cells have reached 26.6% efficiency [6] and a 23.35% efficiency of $\text{Cu}(\text{In,Ga})(\text{Se,S})_2$ (CIGSe) has been achieved [7]. After the rapid development of perovskite solar cells (PVK), the record efficiency of PVK devices is now beyond 22% [8].

In order to approach or even surpass the S-Q theoretical limitation, monolithic perovskite-CIGSe tandem solar cells are becoming a promising option to be fabricated with low cost and achieve higher photovoltaic performance with fewer electrodes and interconnects such as transparent conducting layers and electric wires compared with four terminal tandem photovoltaic structures [18].

However, the development of monolithic perovskite-CIGSe tandem solar cells is still limited because of the absence of suitable band alignment of the top perovskite cell and the bottom CIGSe cell and the complicated designing requirements such as current matching and optical management. Especially an intermediate p-type semiconductor serving as hole conducting material for the top perovskite cell and as one component of the connecting tunnel junction plays an important role in successfully fabricating tandem devices with high photovoltaic performance.

As shown in figure 4.1, two terminal or monolithic tandem solar cells only consist of one anode and one cathode and the entire tandem device is deposited layer by layer [18], which allows to obtain high photovoltaic performance. However, in general monolithic tandem solar cells are more complicated to realize than four terminal devices due to the complex structures requiring process compatibility with all layers and a sophisticated band line-up that guarantees charge carriers transport effectively [16], which will be discussed in detail in the next chapter.

In the last chapter, Cu_2O was discussed as a promising candidate for the intermediate layer of monolithic perovskite-CIGSe tandem solar cells and it shows potential application with wide band gap and superior electrical properties. Except Cu_2O , several inorganic materials meet the requirements for being hole conductors and tunnel junction component in monolithic perovskite-CIGSe tandem solar cells, such as copper gallium oxide (CuGaO_2).

The reason why CuGaO_2 as potential intermediate layer for perovskite-CIGSe tandem solar cells was chosen is that CuGaO_2 exhibits excellent properties, such as wide band

gap (≈ 3.6 eV), high hole mobility (10^{-2} – 10^1 $\text{cm}^2\text{V}^{-1}\text{s}^{-1}$) and a low-lying valence band maximum (≈ -5.3 eV relative to the vacuum level), well matched with the energy levels of perovskite layers [166-168]. However, as a hole transport material, CuGaO_2 has not become a hot research topic in the PVK field, unlike NiO_x and other copper based p-type materials, which have been studied extensively as HTM for PVK devices. For a long time, CuGaO_2 was utilized as p-type photocathode in dye sensitized solar cells (DSCs) and organic photovoltaic devices (OPV) [169-177]. It belongs to the delafossite class of materials, which in general consists of a copper metal oxide compound with the formula $\text{Cu}^{+1}\text{M}^{+3}\text{O}_2$, where the trivalent M atom can be B, Al, Ga, In, Sc, Y, Cr, Fe, Co or Ni. Figure 5.1 shows the hexagonal unit cell of the $\text{Cu}^{+1}\text{M}^{+3}\text{O}_2$ delafossite.

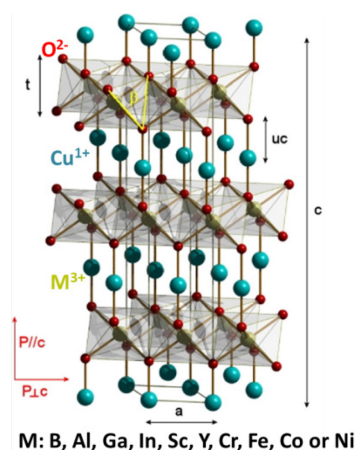


Figure 5.1 Hexagonal unit cell of the $\text{Cu}^{+1}\text{M}^{+3}\text{O}_2$ delafossite. Reproduced with permission [178]. Copyright 2013, IOP PUBLISHING.

In 2015, J. Wang and co-workers [179] prepared CuGaO_2 crystalline nanoplates by a microwave-assisted approach and applied it as HTM in OPV devices, which suppressed recombination at the anode and improved the OPV device performance. Given that CuGaO_2 works for OPV and achieved a PCE of 3.2%, it is also supposed to be appropriate for perovskite solar cells at various points. Therefore, H. Zhang *et al.*[111] published their work on the utilization of hydrothermal synthesis-processed inorganic nanoplates of CuGaO_2 as HTM in the n–i–p configuration PVK devices, where they achieved an optimized efficiency of 18.51%, which surpassed the device based on typical spiro-OMeTAD as organic HTM and improved long-term stability as well.

These studies indicate that CuGaO_2 is a promising candidate for inorganic HTM to replace organic materials to fabricate highly efficient and air stable perovskite solar cells, which consequently also makes them suitable to be utilized as intermediate layer for monolithic perovskite-CIGSe tandem solar cells. In this chapter, firstly, CuGaO_2 films were deposited at room temperature by magnetron sputtering using a CuGaO_2 target. However, the quantitative analysis of XPS data indicated that the oxygen content was insufficient to reach the stoichiometric atomic ratio of the compound. Therefore, further CuGaO_2 films were prepared by sputtering in an

oxygen-containing gas mixture. However, the conductivity was not sufficient and the valence band edge of the resulting CuGaO₂ films did not match with the HOMO level of CH₃NH₃PbI₃, respectively. Therefore, varying the distance between the target and the sample substrate was tried, which slightly improved the valence band maximum of the resulting CuGaO₂. In order to enhance the conductivity of the CuGaO₂ film and make it a highly doped p-type semiconductor, sodium doping on the surface of sputtered CuGaO₂ samples was tried.

5.2 Results and discussion

5.2.1 Sputtering method

The thickness of hole conducting semiconductors in PVK devices has an influence on the photovoltaic performance due to their exciton or diffusion lengths for charge carriers [180]. In order to investigate the thickness of the sputtered CuGaO₂ film, X-ray reflectometry (XRR) was used. As shown in figure 5.2 and table 5.1, the XRR fitting spectra matched with measured data very well. The measured CuGaO₂ film was sputtered for 2 min with 7.5 cm distance (between the target and the substrate) on the glass substrate, 125 mm diameter target with 60 W sputtering power and 4×10⁻³ mbar pressure. Fitting of the XRR measurements showed that the CuGaO₂ film sputtered for 2 min is 33.1 nm thick, which means the deposition rate at 7.5 cm distance is 16.55 nm/min. The acquisition of the deposition rate is important for other characterizations and device fabrication of perovskite-CIGSe tandem solar cells.

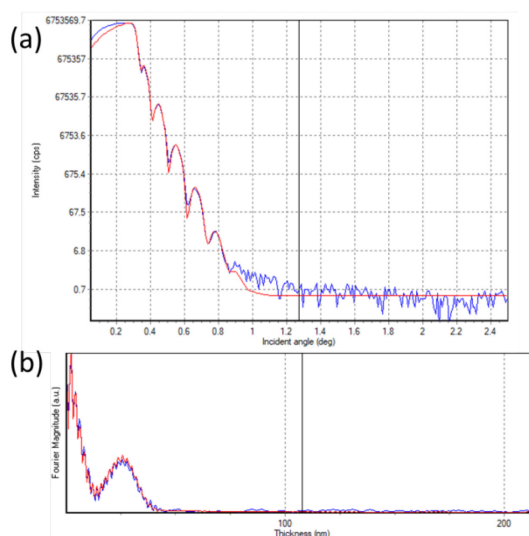


Figure 5.2 The X-ray reflectometry curves with curve fits of sputtered CuGaO₂ on a glass substrate.

TABLE ON NEW PAGE

Table 5.1 The table of X-ray reflectometry fitting results, including film thickness and roughness.

| Layer | Layer Description | Density (g/cm ³) | Thickness (nm) | Roughness (nm) |
|-----------|--------------------|------------------------------|----------------|----------------|
| 1, 0 | CuGaO ₂ | 5.174 | 33.101 | 2.779 |
| Substrate | SiO ₂ | 2.969 | 600000 | 2.09 |

Figure 5.3a shows UV-Vis transmission, reflection, and absorption spectra of the sputtered CuGaO₂ sample with 2 min deposition and 16.55 nm thickness. It shows around 80% transparency in a large wavelength range (500-1500 nm), low reflection and absorption, indicating that as intermediate layer in tandem devices it could let low energy photons pass through to the CIGSe bottom cell. Figure 5.3b shows the optical constants n and k of the sputtered CuGaO₂ sample extracted from the measured reflection and transmission data and calculated by the in house software RefDex which is based on the transfer matrix method [104]. It shows a high refractive index and low optical absorption. The optical absorption coefficients can be calculated by [157]:

$$\alpha = 4\pi k/\lambda \quad (5.1)$$

The plot of α^2 versus the photon energy is shown in figure 5.3c. The band gap E_g of the sputtered CuGaO₂ sample is $3.25 \text{ eV} \pm 0.03 \text{ eV}$, calculated by the relationship [158]:

$$\alpha^2 = hv - E_g \quad (5.2)$$

where hv is the incident photon energy. As discussed in the introduction chapter, in the tandem devices the band gaps of the window layers and the intermediate layers should be selected such that the absorptive losses do not affect parts of the spectrum accessible to the absorber(s) below. Therefore, in principle, a larger band gap of the intermediate layer is preferable, allowing more light to pass through to the bottom CIGSe cells than narrow-band gap materials. The sputtered CuGaO₂ film with a wide band gap of 3.25 eV is a rather suitable semiconductor as intermediate layer for perovskite-CIGSe tandem solar cells.

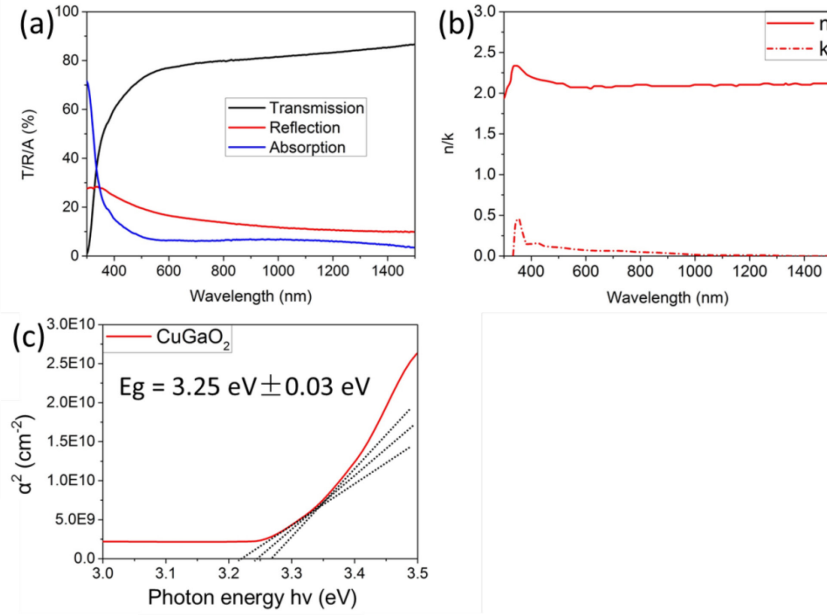


Figure 5.3 (a) UV-Vis transmission spectra, reflection spectra and absorption spectra; (b) refractive index n and extinction coefficient k ; (c) relationship of $\alpha^2 \propto (h\nu - E_g)$ of the sputtered CuGaO₂ sample.

In order to investigate the chemical composition of the sputtered CuGaO₂ sample and assign their chemical states, XPS measurement and quantitate analysis were carried out as shown in figure 5.4. Quantitate analysis is an important method to determine the relative concentrations of the various constituents by utilizing peak area and peak height. For a homogenous sample, the number of photoelectrons per second in a specific spectra peak is given by:

$$I = nf\sigma\theta\gamma\lambda AT \quad (5.3)$$

where n is the number of atoms of the element per cm³ of the sample, f is the x-ray flux, σ is the photoelectric cross-section for the atomic orbital of the interest, θ is an angular efficiency factor for the instrumental arrangement based on the angle between the photon path and detected electron, γ is the efficiency in the photoelectric process for formation of photoelectrons of the normal photoelectron energy, λ is the mean free path of the photoelectrons in the sample, A is the area of the sample from which photoelectrons are detected, and T is the detection efficiency for electrons emitted from the sample [122]. If $S=f\sigma\theta\gamma\lambda AT$ is defined as a sensitivity factor, the concentration ration of two elements can be written by:

$$\frac{n_1}{n_2} = \frac{I_1/S_1}{I_2/S_2} = \frac{I_1 S_2}{I_2 S_1} \quad (5.4)$$

Therefore, quantitate analysis can be used to determine the relative chemical compositions of samples. The Cu oxidation state of the sputtered CuGaO₂ sample is shown in figure 5.4 a, where the Cu 2p_{3/2} peak is located at 932.2 eV, corresponding to the Cu⁺ cation and there is no Cu²⁺ peak observed, which would be located

around 933.5–934.4 eV [98, 181]. Figure 5.4 b shows the Ga 2p_{3/2} peak located at 1117.8 eV, corresponding to the Ga³⁺ [182]. The O 1s peak (figure 5.4 c) for the sputtered CuGaO₂ film is located at 530.5 eV and corresponds to the O²⁻ anion [183]. The oxygen interstitials are the main source for hole carriers in CuGaO₂ films based on first-principle calculations [179, 184]. According to the quantitative analysis of the sputtered CuGaO₂ sample, the atomic concentration result is shown in figure 5.4 d, which is 27% Cu, 31% Ga and 42% O. It indicates that surface oxygen is deficient.

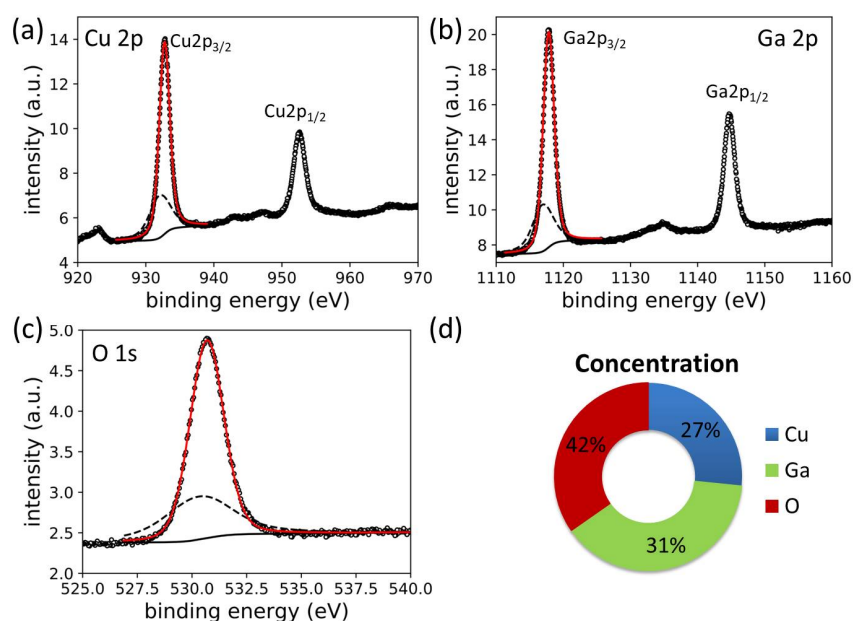


Figure 5.4 Sputtered CuGaO₂ sample: (a) high resolution XPS spectra of Cu 2p; (b) high resolution XPS spectra of Ga 2p; (c) high resolution XPS spectra of O 1s; (d) elemental concentration by quantitative analysis.

5.2.2 Sputtering with additional oxygen supply

In order to increase the ratio of oxygen to cations in CuGaO₂, an additional oxygen supply was added as working gas together with argon during sputtering. Figure 5.5 shows the XPS spectra measured after deposition without breaking vacuum, avoiding the oxidation and contamination from air and their quantitative analysis. Next to the Cu 2p peak, an obvious satellite at 942–945 eV appears, indicating the presence of a Cu²⁺ species [183]. The Ga 2p_{3/2} peak is located at 1117.8 eV corresponding to Ga³⁺ [182] and the O 1s peak for the sputtered CuGaO₂ film with additional oxygen supply is located at 530.5 eV corresponding to the O²⁻ anion, which are identical to the originally sputtered CuGaO₂ sample without additional oxygen. From the quantitative analysis as shown in figure 5.5 d, the oxygen concentration increases compared with the originally sputtered CuGaO₂ sample, suggesting that an additional oxygen supply works for increasing the oxygen concentration in CuGaO₂ samples and the atomic concentration is approximately Cu:Ga:O=1:1:2.

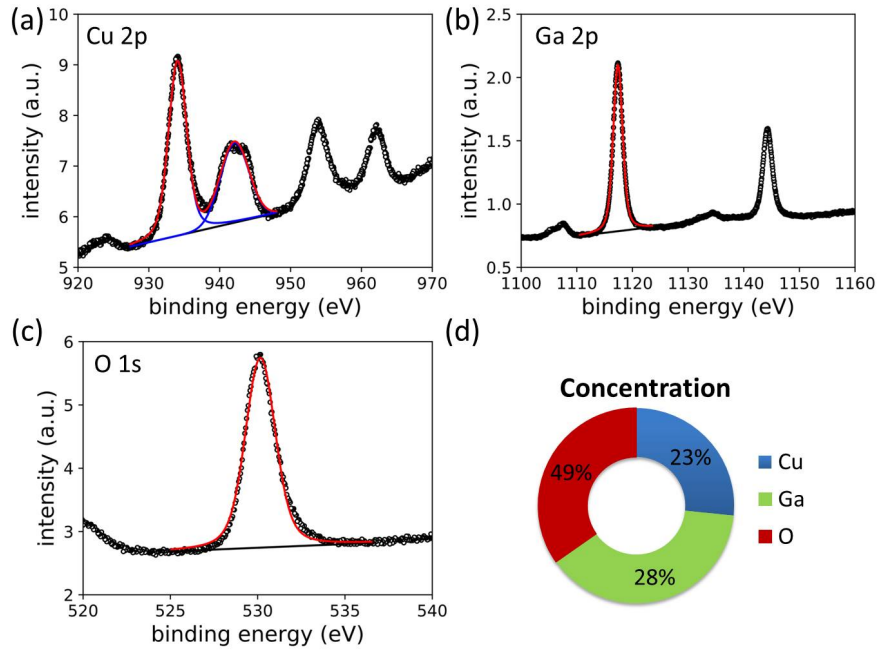


Figure 5.5 Sputtered CuGaO₂ sample by additional oxygen supply: (a) high resolution XPS spectra of Cu 2p; (b) high resolution XPS spectra of Ga 2p; (c) high resolution XPS spectra of O 1s; (d) element concentration by quantitative analysis.

Since the compounds consisted of Cu⁺ or Cu²⁺, Ga³⁺ and O²⁻ irrespective of atomic concentration, band structures of these compounds should be determined in order to find out if they are compatible with the energy level of perovskite layers for the integration in monolithic perovskite-CIGSe tandem solar cells. Therefore, UPS measurements using He I (21.22 eV) and He II (40.81 eV) emissions were carried out. In figure 5.6 the comparison of UPS results of the sputtered CuGaO₂ sample with and without additional oxygen supply is shown. The valance band maximum (VBM) relative to the Fermi level was determined by extrapolating the leading edge linearly to the baseline. The value of the intersection is the VBM position of the material, which is 0.93 eV for the original sample and 1.35 eV for the oxygen sample, respectively. Because the valance band edge spectra are not sharp and linear, an error margin of 0.05 eV for the VBM values is assumed. This error increases when using He I as excitation energy. Therefore, the VBM determination for CuGaO₂ samples used He II. The secondary electron edge was measured with He I radiation and by finding the intersection between the secondary cut-off edge with the baseline the work function was determined according to:

$$\Phi = h\nu - (cutoff - E_F) \quad (5.5)$$

where Φ is the work function of the measured material, the cutoff is the point of intersection and E_F is the Fermi-level of the Au reference after calibration. Since the work function and VBM are determined by UPS and the band gap E_g was obtained by optical measurements as shown in figure 5.3, the band structures of the oxygen-free sputtered CuGaO₂ sample and the sample with additional oxygen can be calculated. They are shown in figure 5.6 d. The VBM of the sample without additional oxygen

supply is higher than that of the sample with additional oxygen supply, which higher VBM is more compatible with perovskite layer.

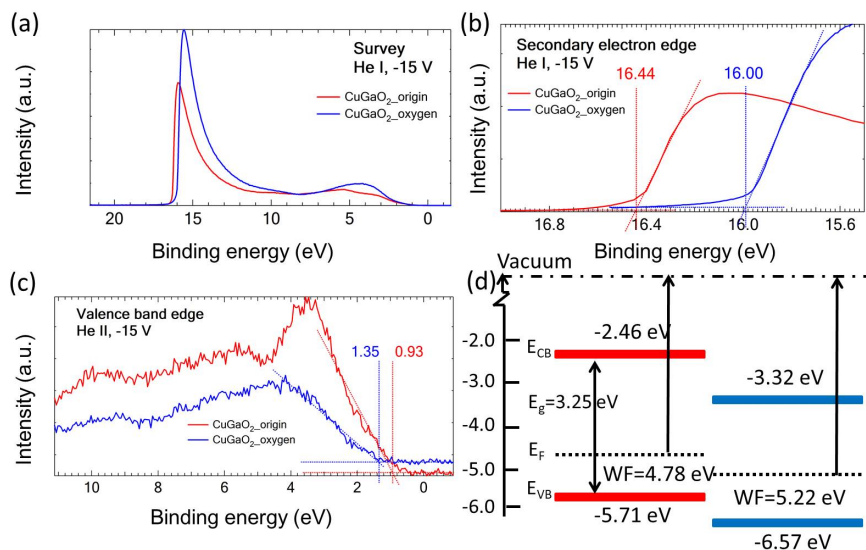


Figure 5.6 Original sputtered CuGaO_2 sample without additional oxygen supply (red curves and lines) and sputtered CuGaO_2 sample with additional oxygen supply (blue curves and lines): (a) UPS survey spectra; (b) secondary electron edge; (c) valence band maximum; (d) energy diagram relative to the vacuum level.

5.2.3 Sputtering with varied distance

As discussed in the last section, the originally sputtered CuGaO_2 sample shows an oxygen deficit. The oxygen content increases by adding additional oxygen together with argon during sputtering. However, it also leads to a deeper valence band (larger work function), which is not compatible with the perovskite layer for the application in perovskite-CIGSe tandem solar cells. Therefore, more parameters should be optimized to achieve better band alignment and good quality CuGaO_2 films.

The original CuGaO_2 sample described before was sputtered at a target-to-substrate distance (D_{ts}) of 7.5 cm ($D_{ts}=7.5$ cm, time=2 min, diameter=125 mm, Power=60 W, Pressure= 4×10^{-3} mbar). Varying D_{ts} has a great influence on structural, electrical and optical properties of the films prepared by RF magnetron sputtering, including the electrical resistivity, the atomic ratio of Ga to O, the transmittance and the optical band gap [185]. So a D_{ts} variation impact on sputtered CuGaO_2 sample was investigated from D_{ts} values of 7.5 cm to 5.0 cm. The substrate was sputtered at 7.5 cm for 2 min (around 33 nm as calculated in table 5.1) first, afterwards it was immediately transferred to the analysis chamber of the CISSY system for XPS and UPS measurements without breaking vacuum. The process was repeated another three times, at D_{ts} values of 7.0 cm, 6.0 cm and 5.0 cm for each 2min. The entire deposition process and measurements were done under vacuum all the time, avoiding extra oxidation and contamination from air.

The comparison of XPS results for the samples with different D_{ts} is shown in figure

5.7. The Cu $2p_{3/2}$ and $2p_{1/2}$ peaks are located at 932.2 eV and 952.5 eV, respectively, corresponding to the Cu^+ cation and no Cu^{2+} peak is observed located around 933.5–934.4 eV [98, 181, 186]. The O 1s peak (figure 5.7 c) for the sputtered CuGaO_2 film is located at 530.5 eV; it corresponds to the O^{2-} anion [183]. As shown in figure 5.7 d, the Ga $2p_{3/2}$ and Ga $2p_{1/2}$ peaks are located at 1117.8 eV and 1144.9 eV, corresponding to the Ga^{3+} [182]. It can be concluded that the peak positions of Cu^+ , Ga^{3+} and O^{2-} are not changed by sputtering with different D_{ts} .

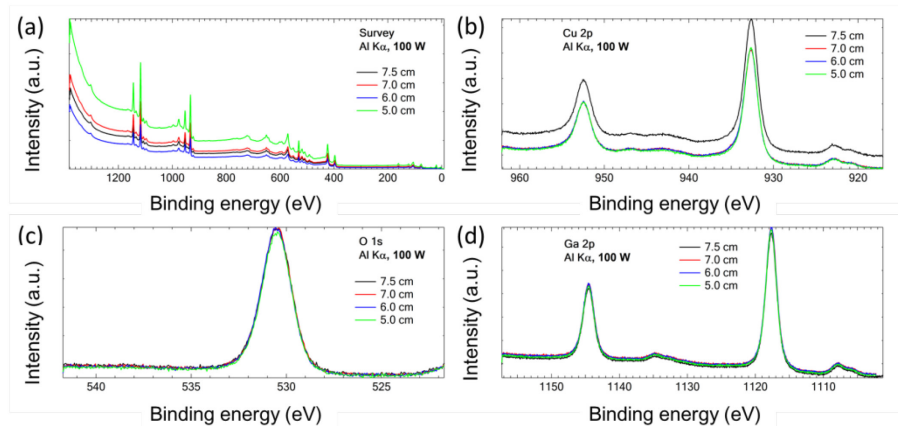


Figure 5.7 Sputtered CuGaO_2 samples at varying target-sample distance: (a) XPS survey spectra; (b) high resolution XPS spectra of Cu 2p; (c) high resolution XPS spectra of Ga 2p; (d) high resolution XPS spectra of O 1s.

In order to investigate the band structures of samples with different D_{ts} , UPS was used to measure VBM and work function with excitation energies from He I (21.22 eV) and He II (40.81 eV). Figure 5.8 shows the UPS spectra of the sample with D_{ts} _5.0 cm and the comparison of the band structures of sample D_{ts} _7.5 cm (VBM and work function are calculated in figure 5.6) and D_{ts} _5.0 cm. For sample D_{ts} _5.0 cm, as described in the previous section about VBM and work function calculation based on the measured valence band edge and secondary electron edge spectra, the value of the intersection between the leading edge and the base line is 0.84 eV (He II radiation was used for a more linear curve). The work function of sample D_{ts} _5.0 cm determined by the formula 5.5 is 4.69 eV. The resulting band structure of sample D_{ts} _5.0 cm is shown in figure 5.8 d. The VBM of sample D_{ts} _5.0 cm is slightly higher than that of sample D_{ts} _7.5 cm, indicating that decreasing the target-to-substrate distance can improve the band structure of a CuGaO_2 sample, resulting in a better match with the perovskite layer.

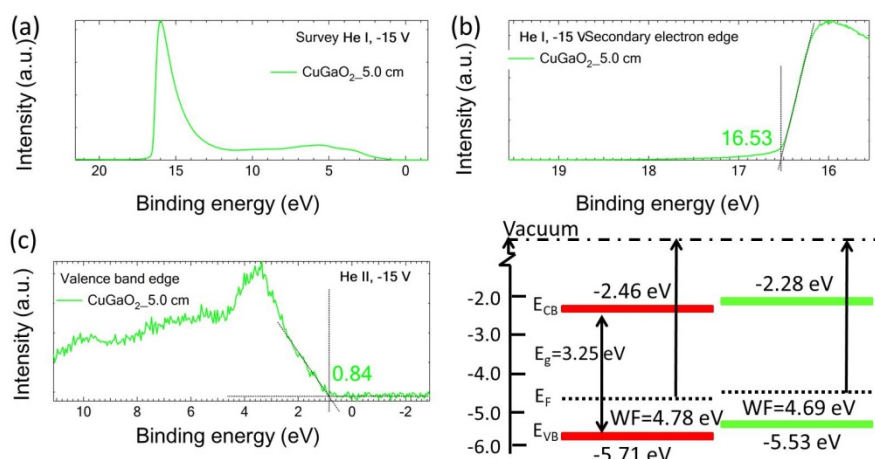


Figure 5.8 Sputtered CuGaO_2 sample at 5.0 cm distance (green curves and lines): (a) UPS survey spectra; (b) secondary electron edge; (c) valence band maximum; (d) energy diagram relative to the vacuum level compared with a CuGaO_2 sample at 7.5 cm distance (red lines).

5.2.4 Sodium doping

The structure of a monolithic perovskite-CIGSe tandem solar cell was illustrated in the introduction chapter, consisting of a perovskite top cell, a CIGSe bottom cell and an intermediate tunnel junction. The p-type semiconductors such as Cu_2O and CuGaO_2 are combined with the n-type transparent conducting oxide (TCO) on top of CIGSe, such as aluminum doped zinc oxide (AZO), to form the intermediate tunnel junction, which requires highly doped materials to align the bands. Therefore, sodium as a dopant was considered to make CuGaO_2 become a p^{++} semiconductor.

The samples were sputtered at a distance of 7.5 cm for 2 min without addition of oxygen as working gas ($D_{ts}=7.5$ cm, time=2 min, diameter=125 mm, Power=60 W, Pressure= 4×10^{-3} mbar). Afterwards they were transferred to the MBE chamber of the CISSY system (shown in figure 2.7) for sodium doping without breaking vacuum. A sodium metal dispenser was used as source of sodium doping on the sputtered CuGaO_2 sample. The details of the process of the sodium doping is described in chapter 2.

As shown in figure 5.9, the XPS measurements were conducted on the bare sputtered CuGaO_2 sample, after 6 min Na deposition, after 7 days under vacuum and after another 7 days in air, respectively. Oxidation of Cu and Ga would lead to shoulders at the Cu 2p and Ga 2p peaks at 932.2 eV and 1119.0 eV, respectively [98, 181, 186, 187]. Only the sample exposed to air for 7 days has two obvious satellites or shake-up lines at 942–945 eV and 960–965 eV, indicating the presence of Cu(II) species due to the oxidation by air [183, 188]. The O 1s peak for all the vacuum CuGaO_2 samples is located at 530.5 eV, corresponding to the O^{2-} anion [183], while there is a 0.5 eV shift for the air sample. However, the Na 1s peak appears at 1071.8 eV after 6 min of Na deposition [189]. After 7 days under vacuum, the XPS spectrum of Na 1s still shows a strong peak at the same binding energy position, but the

intensity decreases slightly after exposure to air, indicating that the sodium diffuses from the surface to the bulk material, reducing the signal intensity.

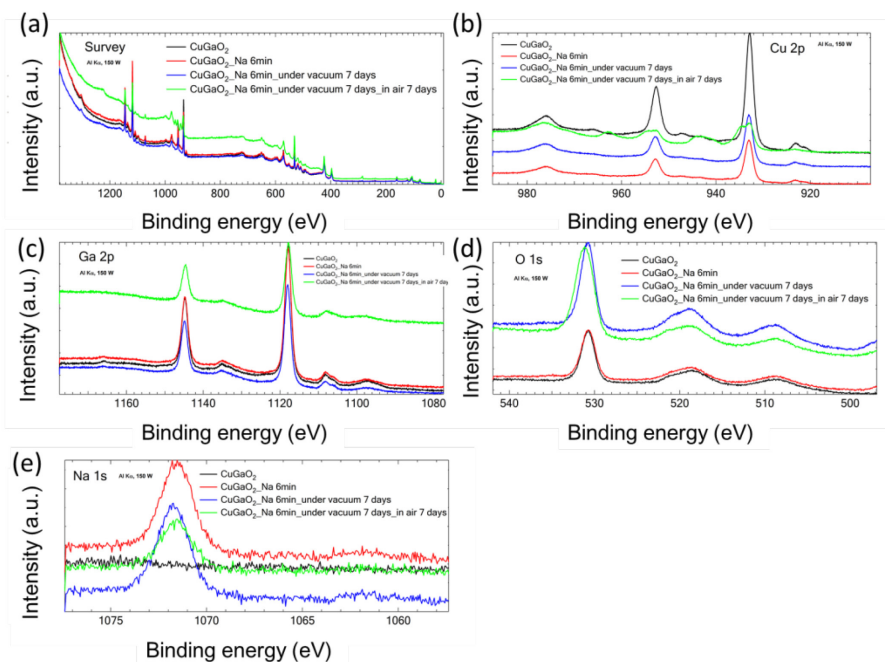


Figure 5.9 Sputtered CuGaO_2 samples with sodium doping: (a) XPS survey spectra; (b) high resolution XPS spectra of Cu 2p; (c) high resolution XPS spectra of Ga 2p; (d) high resolution XPS spectra of O 1s; (e) high resolution XPS spectra of Na 1s.

According to the UPS measurements and calculations, figure 5.10 shows the band structures of samples without and with sodium doping. Shown are a bare sputtered CuGaO_2 sample, after 6 min Na deposition, after 7 days under vacuum and after another 7 days in air, respectively. He I (21.22 eV) and He II (40.81 eV) were used to measure work function and VBM of samples, respectively. As described in the previous section about VBM and work function calculation based on the measured valence band edge and secondary electron edge spectra, the value of the intersection between the leading edge and the base line is 0.99 eV for the bare sputtered CuGaO_2 sample, 1.08 eV for the Na doping sample, 1.86 eV for the sample under vacuum for 7 days and 1.49 eV for the sample in air for another 7 days. The work functions of samples determined by the formula 5.5 are 5.05 eV, 3.82 eV, 4.08 eV and 4.44 eV, respectively. The figure 5.10 d shows the band structures of samples. After 6 min Na doping, the VBM of sample increases greatly from -6.04 eV to -4.90 eV relative to the vacuum level. After 7 days for Na diffusion from the surface to the bulk under vacuum and in air, the VBMs of the sample drop to -5.94 eV and -5.93 eV relative to the vacuum level, still higher than the VBM of the bare sputtered CuGaO_2 sample. This shows that sodium doping on the surface of samples can directly improve the VBM and still has a positive influence on band alignment with the perovskite layer after diffusion.

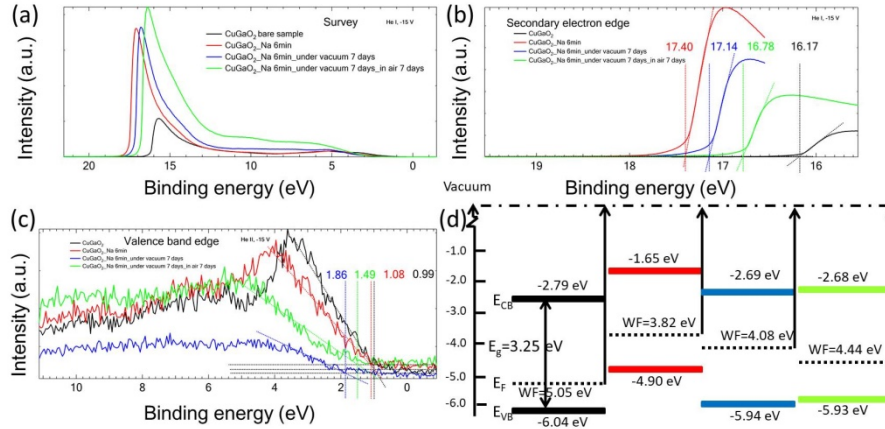


Figure 5.10 Sputtered CuGaO_2 samples with sodium doping: (a) UPS survey spectra; (b) secondary electron edge; (c) valence band maximum; (d) energy diagram relative to vacuum level.

5.3 Summary and outlook

In this chapter, CuGaO_2 films were deposited at room temperature by magnetron sputtering using a CuGaO_2 target. However, from the quantitative analysis of XPS, it showed that the layer is oxygen is deficient. Therefore, oxygen was added to the argon as a working gas during the CuGaO_2 sputter process. The valence band maximum of the resulting CuGaO_2 sample didn't match with the HOMO level of $\text{CH}_3\text{NH}_3\text{PbI}_3$ well, not matching with the original design and intention of monolithic perovskite-CIGSe solar cells. More parameters optimizations were conducted to improve the CuGaO_2 films. Varying the distance between the target and the sample substrate slightly improved the valence band maximum of the resulting CuGaO_2 . Sodium doping by evaporation sodium metal on the surface of the sputtered CuGaO_2 sample has directly improved the VBM position and still has positive influence on band alignment with the perovskite layer after sodium diffusion.

As described in the introduction chapter, inorganic hole transport materials are promising candidates in replacing organic HTM in PVK devices and monolithic perovskite-CIGSe tandem solar cells. As this intermediate layer serves not only as the p-contact of the top PVK, but also as one of the components of the intermediate tunnel junction consisting of a highly p doped semiconductor and a highly n doped semiconductor in monolithic perovskite-CIGSe tandem solar cells, this intermediate layer should meet some requirements, such as transparency, good conductivity, stability, low-temperature preparation, and band positions. In order to enhance the properties of CuGaO_2 films including the conductivity, adding other dopants can be a direction of future research work. For instance, some groups studied the effect of magnesium doping on the hole conductivity of CuGaO_2 and the conductivity increased by one order of magnitude after Mg doping [190, 191].

6 Optical and electrical simulations for monolithic perovskite-CIGSe tandem solar cells

6.1 Background

Theoretical analysis using device simulation is intensively performed for solar cells to understand device operation mechanism and to design optimum layer configuration to reach the maximum efficiency [192]. In order to fully exploit the opportunity offered by the monolithic perovskite-CIGSe tandem solar cells, optical and electrical simulations are used to predict the photovoltaic efficiency and explain device mechanism.

As described in the introduction chapter, current matching between the top and bottom cell is a big challenge to better utilize the broad solar spectrum and fabricate efficient monolithic tandem solar cells [17]. In order to achieve the highest matched current density J_{matchsc} and the best power conversion efficiency of tandem devices, an elaborate optical design of the integrated configuration and accurate control of absorption layer thicknesses is needed. In order to predict the matched current density J_{matchsc} and optical losses theoretically, it is necessary to optimize experimentally proven material stacks and thickness combinations by means of optical simulations [193]. Figure 6.1 shows an optical simulation of monolithic planar perovskite-silicon tandem solar cells under current matching conditions.

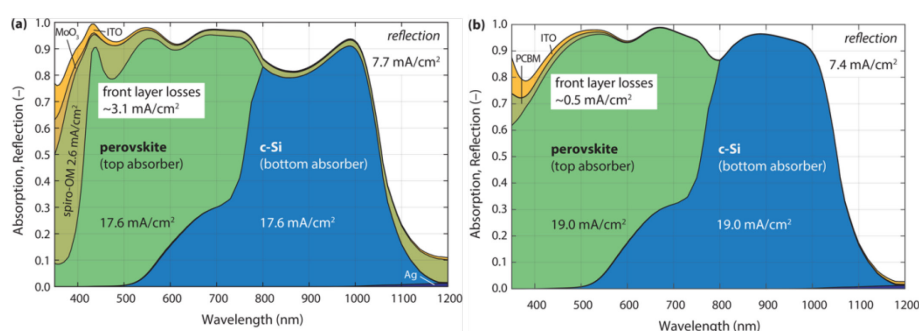


Figure 6.1 Optical absorption profiles of optimized devices for (a) the regular architecture, and (b) the inverted architecture of monolithic planar perovskite-silicon tandem solar cells. Adapted with permission from ref [193]. Copyright 2017, Optical Society of America.

Electrical simulation by SCAPS is a useful tool to analyze the conventional solar cells such as silicon [194], CdTe [195, 196] and CIGSe [40, 197, 198]. However, only few theoretical analyses of the single junction perovskite solar cells are available. As this intermediate p-type semiconductor serving as one of the components of the tunnel junction and also hole transport layer for the top perovskite cell, it is necessary to optimize its electrical properties for achieving high efficiency. Additionally, the planar structure of the perovskite solar cells is similar to thin film solar cells, such as CIGSe. Therefore, the electrical simulation by SCAPS is applicable to the single junction

perovskite solar cells with p-type semiconductors as hole transport materials. Optimizing the properties of the intermediate layer such as Cu_2O and CuGaO_2 as hole conductors in the top perovskite cell is the first step and very important for simulating the photovoltaic performance of the entire monolithic perovskite-CIGSe tandem solar cells.

In this chapter, a model of monolithic perovskite-CIGSe tandem solar cell is described using Cu_2O and CuGaO_2 as intermediate layers. The in-house software RefDex [104, 124, 199] was applied to illustrate the impact of Cu_2O and CuGaO_2 on the performance of a tandem device and the reflection, transmission and absorption (R/T/Abs) of the individual layers under the condition of current matching were calculated. The highest matched current density was achieved by varying the thickness of the perovskite layer. In addition, a series of calculations for the equivalent electrical circuit of the monolithic tandem solar cell was carried out to estimate the total power conversion efficiency of the perovskite-CIGSe tandem solar cells based on the matched current which was optimized by the optical simulation.

6.2 Results and discussion

6.2.1 Optical simulation

The optical simulation was performed by the in-house software RefDex and described in chapter 2. A model of perovskite-CIGSe tandem solar cells consists of Mo/CIGSe/CdS/i-ZnO/AZO/ Cu_2O or $\text{CuGaO}_2/\text{CH}_3\text{NH}_3\text{PbI}_3/\text{PCBM}/\text{ITO}$, with CIGSe as absorber of the bottom cell, CdS as buffer layer, i-ZnO and AZO as window layers, the sputtered Cu_2O as intermediate hole transport material, $\text{CH}_3\text{NH}_3\text{PbI}_3$ as absorber layer of the top cell, PCBM as electron transport material. The optical constants and thickness of the individual layers are listed in the table 6.1. As described in the chapter 4, figure 4.7 shows the refractive index n and extinction coefficient k of the sputtered Cu_2O sample calculated by RefDex based on the measured transmission and reflection data by UV-Vis measurement.

Table 6.1 Layer thickness of the perovskite-CIGSe tandem solar cells and references to the refractive indices of individual layers. All the n k values are shown in Appendix.

| Layers | Molybdenum coated glass | CIGSe absorber | CdS | i-ZnO | AZO | Cu_2O | Perovskite | PCBM |
|----------------|-------------------------|----------------|-------|-------|-------|-----------------------|------------|-------|
| Thickness (nm) | 2000000 | 3000 | 50 | 130 | 5 | 20 | 100-600 | 25 |
| n, k source | [104] | [104] | [104] | [104] | [104] | This work | [156] | [200] |

The optical constants of each layer are imported to the software. Interface roughness is not taken into account. As described in the introduction chapter, the best performance of tandem device is achieved by matching the short circuit current density between the top (J_{topsc}) and bottom cell (J_{botsc}). The matched current density

(J_{match}) is integrated from the absorption in the perovskite and CIGSe layer without collection loss under AM 1.5G illumination [104]. In order to better utilize the broad solar spectrum and simplify the calculation, the thickness of CIGSe layer is fixed to 3 μm , which is the thickness of the CIGSe layer in chalcopyrite thin film solar cells for absorbing most of the long-wavelength light. Increasing the thickness of CIGSe layer higher than 3 μm does not increase the J_{match} , while lower than 2 μm will decrease the J_{match} and the performance of the tandem cell. Therefore, the thickness of the perovskite layer is varied under the condition of the fixed 3 μm CIGSe layer. The other layers' thicknesses are shown in table 6.1. Figure 6.2 shows the short circuit current density of perovskite and CIGSe absorbers in the tandem as a function of the perovskite layer thickness. Increasing the thickness of the perovskite layer will lead to the improvement of J_{topsc} and the reduction of J_{botsc} because the perovskite layer absorbs short-wavelength incident light and the CIGSe layer absorbs the rest of the light. The current density of two absorbers will be compatible when the optimization of incident light utilization achieves a balance. As shown in figure 6.2, the thickness of the perovskite layer is 435 nm to reach the match point.

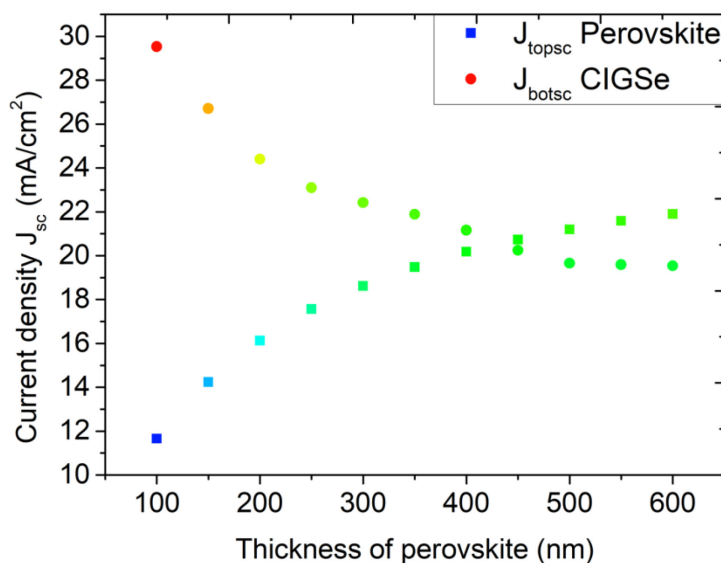


Figure 6.2 Calculated current density of perovskite and CIGSe absorbers in the tandem as a function of the perovskite layer thickness with a fixed CIGSe thickness of 3 μm .

Figure 6.3 shows the schematic architecture of the Cu_2O based monolithic perovskite-CIGSe tandem device and the optical losses of the entire tandem solar cells. In principle, the optical losses of the entire tandem device under the condition of current matching can be divided into four parts: reflection (R), parasitic absorption in the Cu_2O film ($\text{Abs}_{\text{Cu}_2\text{O}}$), parasitic absorption in the CIGSe absorber ($\text{Abs}_{\text{CIGSe}}$), and parasitic absorption in the perovskite layer ($\text{Abs}_{\text{perovskite}}$). As shown in figure 6.3, the highest matched current density of 20.5 mA/cm^2 is achieved when the thickness of the perovskite layer is 435 nm and Cu_2O is 20 nm. The parasitic absorption in the Cu_2O film is negligible, corresponding to a current of 0.4 mA/cm^2 , indicating that the

sputtered Cu_2O film weakly absorbs the incident light. In addition, the absorption in the PCBM layer is corresponding to the current of 1.0 mA/cm^2 , higher than that of Cu_2O film.

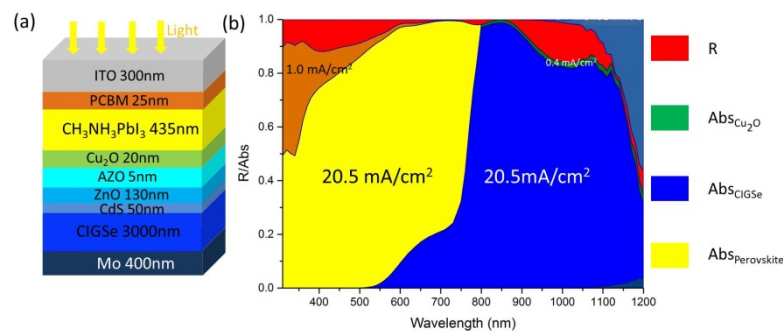


Figure 6.3 Monolithic perovskite-CIGSe tandem solar cell with Cu_2O as intermediate layer (a) schematic of the device architecture and thickness for individual layer; (c) reflection and absorption of the entire tandem device under the condition of matched current density between top perovskite and bottom CIGSe cell.

In order to investigate the optical losses of the tandem based on the sputtered CuGaO_2 film, a similar process is carried out by using the software RefDex. First, the optical constants of the sputtered CuGaO_2 film are calculated based on the measured transmission and reflection data as shown in figure 5.3. The thickness variation of the perovskite layer is done to achieve the highest matched current density. As shown in figure 6.4 a, the optimal thickness of the perovskite layer is 450 nm, the CIGSe absorber and the CuGaO_2 film are fixed at $3 \mu\text{m}$ and 20 nm, respectively. As a result, the highest matched current density of the entire tandem structure based on CuGaO_2 is 20.8 mA/cm^2 as shown in figure 6.4 b, which is slightly higher than the Cu_2O -based tandem device (20.5 mA/cm^2). The CuGaO_2 film absorbs less incident light, corresponding to only 0.2 mA/cm^2 , compared to the Cu_2O film. From optical simulation, the sputtered CuGaO_2 film shows better properties than Cu_2O film as intermediate hole transport layer in the monolithic perovskite-CIGSe tandem solar cells.

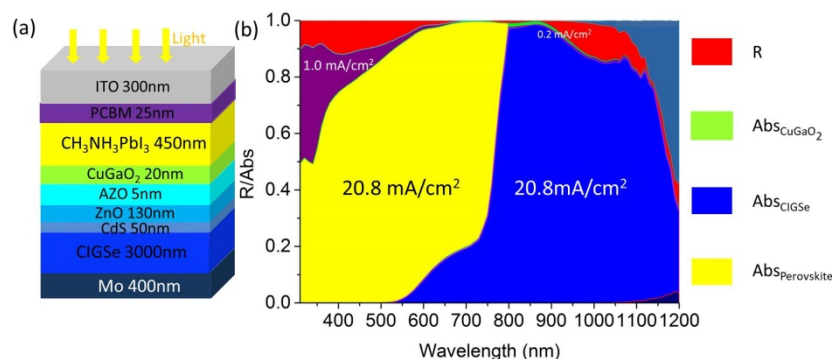


Figure 6.4 Monolithic perovskite-CIGSe tandem solar cell with CuGaO_2 as intermediate layer (a) schematic of the device architecture and thickness for individual layer; (c) reflection and absorption of the entire tandem device under the condition of matched current density between top perovskite and bottom CIGSe cell.

6.2.2 Electrical simulation

In order to know the photovoltaic performance of the entire tandem device with a short circuit current density of 20.8 mA/cm^2 , the power conversion efficiency of the tandem cell is calculated. The equivalent circuit of the monolithic tandem solar cells is shown in figure 6.5. The diode 1 (D1) and diode 2 (D2) represent the top cell perovskite and the bottom cell CIGSe, respectively. Due to the lateral transportation of current through the ITO electrode series resistance R_s is taken into account. The J-V parameters for the single junction perovskite and CIGSe solar cells are taken from the real devices, with efficiencies of 19.3% [129] for perovskite solar cells and 21.7% [201] for CIGSe solar cells. The diode parameters and J-V parameters of these two cells are listed in table 6.2. When the single junction perovskite and CIGSe cells are applied to the tandem, it can be assumed that their qualities are maintained in the tandem. Therefore, the quality factor of 1.5 for the perovskite cell and 1.38 for the CIGSe are used for the equivalent circuit parameters of the tandem.

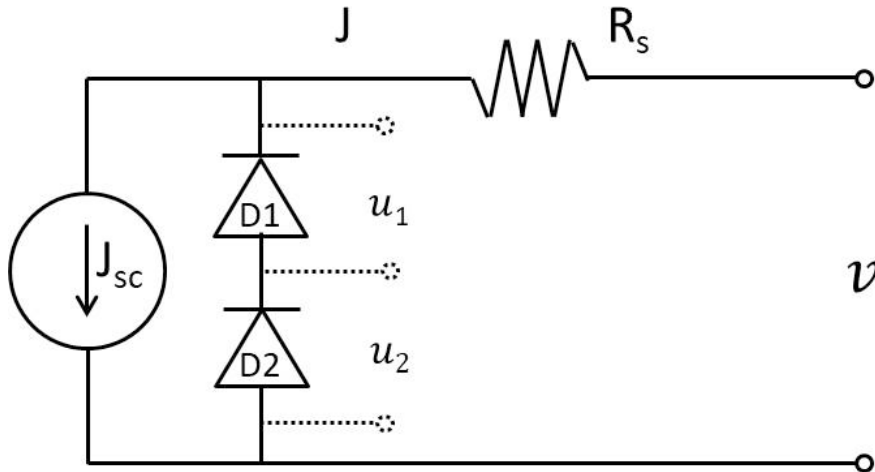


Figure 6.5 Equivalent circuit of the monolithic tandem solar cell.

Table 6.2 Diode and J-V parameters for the single junction perovskite and CIGSe solar cells.

| | Saturation current density J_0 (mA/cm^2) | Quality factor A | Efficiency in lab scale | V_{oc} (V) | J_{sc} (mA/cm^2) | FF (%) |
|------------------|---|------------------|-------------------------|--------------|-------------------------------|--------|
| Perovskite [129] | | | | | | |
| D1 | 2.8×10^{-11} | 1.5 | 19.3% | 1.13 | 22.75 | 75.01 |
| CIGSe [201] | | | | | | |
| D2 | 2.4×10^{-8} | 1.38 | 21.7% | 0.746 | 36.6 | 79.3 |

Based on the equivalent circuit of the monolithic tandem as shown in figure 6.5, several equations are derived as follows:

$$J = J_{sc} - J_{01} \left[\exp\left(\frac{qu_1}{A_1 k_0 T}\right) - 1 \right] \quad 6.1$$

$$J_{01} \left[\exp\left(\frac{qu_1}{A_1 k_0 T}\right) - 1 \right] = J_{02} \left[\exp\left(\frac{qu_2}{A_2 k_0 T}\right) - 1 \right] \quad 6.2$$

$$u_1 + u_2 = v + IR_s \quad 6.3$$

Where J_{sc} is the short circuit current density for the case of no serial resistance, which is taken from figure 6.4 (20.8 mA/cm²). J_{01} and J_{02} are the saturation current densities, A_1 and A_2 are the quality factors for diode 1 and diode 2, respectively, which are listed in table 6.2. T is the room temperature in Kelvin, q is the elemental charge, k_0 is the Boltzman constant. R_s is related to the lateral transport of current through the ITO electrode. I is the current through R_s , u_1 and u_2 are the voltage drops at the diode 1 and diode 2, respectively.

The open circuit voltage (V_{oc}) of the device, which is estimated according to the well-known relationship [202]:

$$V_{oc} = \frac{nkT}{q} \ln \left[\frac{J_{ph}}{J_0} + 1 \right] \quad 6.4$$

Where J_{ph} is the photocurrent density, which is generally equal to the short-circuit current density (J_{sc}). Because J_0 is quite small compared to J_{sc} , the value of J_{sc}/J_0 will be extremely large. Therefore, the exponential part (J_{ph}/J_0+1) can be simplified as J_{ph}/J_0 for calculation.

The series resistance R_s can be considered to be due to the current through ITO on the top of the tandem. As shown in figure 6.6, the length (L) of the ITO strips is assumed to be 10 mm and the width is represented by the symbol W . In the realistic module, numerous strips of the tandem cell are connected monolithically to transport the current through the entire tandem.



Figure 6.6 Illustration of lateral transport of current through ITO strips.

Therefore, the equation 6.3 mentioned above can be transformed as follows:

$$IR_s = \int_0^L J W R_s(x) dx = \int_0^L \frac{J W \rho(L-x)}{2d_{ITO} W} dx = \frac{J \rho L^2}{2d_{ITO}} \quad 6.5$$

$$u_1 + u_2 = v + \frac{J \rho L^2}{2d_{ITO}} \quad 6.6$$

Where the size of one stripe of the solar cell is $L \times W$ (L is 10 mm), thickness of ITO

(d_{ITO}) is assuming equal to 300 nm, and resistivity of ITO (ρ) is 15 Ω/sq .

From the equation 6.1, 6.2, and 6.6, a Matlab code can be written and programmed. The simulated J-V curve of the perovskite-CIGSe tandem solar cells is shown in figure 6.7. The short circuit current density is 20.8 mA/cm^2 , which was calculated previously by the optical simulation under the condition of current matching. The open circuit voltage is 1.75 V, which is approximately the sum of the voltage of the two individual single cells and also verifies that the V_{oc} value of the monolithic tandem solar cells is the V_{oc} of top cell plus the V_{oc} of bottom cell. The eventual power conversion efficiency of the perovskite-CIGSe tandem is 30.3% with a fill factor of 0.83. This result is estimated on the basis of existing perovskite and CIGSe single devices, which is a more realistic prediction of the performance for the perovskite-CIGSe tandem compared to the maximum efficiency simulated for a two junction tandem described in the introduction chapter.

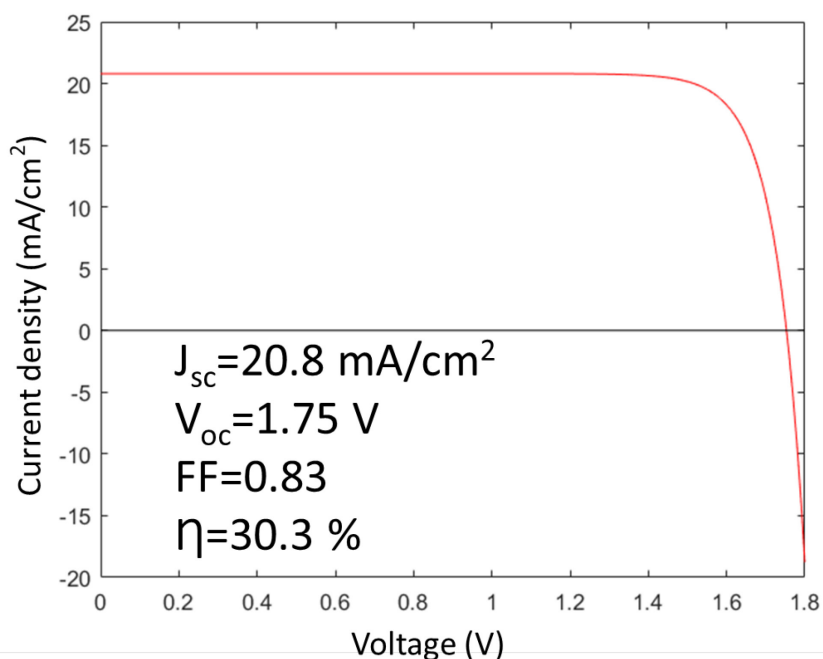


Figure 6.7 J-V curves of the monolithic perovskite-CIGSe tandem solar cells using CuGaO_2 as intermediate layer.

6.3 Summary and outlook

In this chapter, a model for monolithic perovskite-CIGSe tandem solar cells using Cu_2O and CuGaO_2 as intermediate layers was built for optical and electrical simulation. For the optical simulation, a thickness variation was done to calculate the reflection, transmission and absorption of individual layers to reach current matching, which is the necessary condition to achieve the best performance of tandem devices. The highest matched current of 20.8 mA/cm^2 was obtained by a CuGaO_2 -based perovskite-CIGSe tandem device. In order to estimate the photovoltaic performance

of a tandem device with 20.8 mA/cm^2 current density, a series of calculations for the equivalent circuit of the monolithic tandem solar cells was carried out and the optimal power conversion efficiency was 30.3% with a V_{oc} of 1.75 V and a fill factor of 0.83. The V_{oc} value was approximately the sum of the voltage of the two individual single cells.

The optical simulation and electrical simulation are important characterization methods to predict the photovoltaic performance and analyze the recombination losses of monolithic tandem solar cells. As shown in this chapter, Cu_2O and CuGaO_2 are promising candidates as intermediate layers for the monolithic perovskite-CIGSe tandem solar cells.

7 Summary

The objective of this thesis was to construct and investigate monolithic perovskite-CIGSe tandem solar cells, including a low band gap chalcopyrite solar cell as bottom cell and p-type semiconductors Cu_2O and CuGaO_2 as intermediate layers, serving as hole transport material and as one component of the tunnel junction. In addition, using the optical and electrical simulations, the photovoltaic performance of the monolithic perovskite-CIGSe tandem device was predicted and the suitability of Cu_2O and CuGaO_2 over organic hole transport materials in single junction perovskite solar cells was shown.

Several experiments were done to understand the properties of the monolithic perovskite-CIGSe tandem solar cells and to find suitable ways to fabricate high efficient tandem devices.

First, a non-vacuum simple direct solution coating approach for $\text{CuIn}(\text{S}, \text{Se})_2$ absorber thin film solar cell was developed, which is described in **Chapter 3**, introducing a low cost and environmentally friendly molecular ink containing copper chloride, indium chloride, thiourea as precursors, and ethanol, ethylene glycol and ethylene glycol butyl ether as solvents. On the one hand, the ethylene glycol butyl ether as solvent contributed to improve the homogeneity of the absorber film. On the other hand, thiourea from the molecular ink can introduce sulfur into CIGSe solar cell by replacing Se with S without using toxic and hazardous H_2S gas. By means of varying the thickness of the absorber, it can directly increase the short circuit current density. Adding sodium was tried to improve champion cell efficiency, but the effect was not prominent. Finally, a low band gap (1.02 eV) $\text{CuIn}(\text{S}, \text{Se})_2$ thin film solar cell was fabricated using the absorber film prepared by this route, which exhibited an efficiency of 9.5% under AM 1.5 illumination. The dominant recombination mechanism in the solar cell was the absorber bulk recombination.

Secondly, looking for suitable p-type semiconductor as intermediate layer is also a key factor to fabricate efficient tandem device. Therefore, p-type Cu_2O films were fabricated at room temperature by magnetron sputtering using nitrogen doping, leading to high transparency and good conductivity. This is subject of **Chapter 4**. The electronic structure of Cu_2O was calculated and the energy levels of a monolithic perovskite-CIGSe tandem solar cell were shown. However, because of the bad wetting behavior and visible degradation at the interface of the sputtered Cu_2O sample and the spin-coated perovskite layer, a Cu_2O film with extremely high transparency was prepared by a wet chemical approach and applied to single junction perovskite solar cells. These achieved over 9% photoconversion efficiency, indicating that the Cu_2O film opens new avenues for monolithic perovskite-CIGSe tandem solar cells as one component of the intermediate tunnel junction and that it also has the potential to achieve high efficiency photovoltaics devices.

Considering the wet chemical approach for depositing Cu_2O film is inefficient for large scale production and the quality of the films is quite inhomogeneous, therefore

looking for another appropriate p-type semiconductor prepared by a simple and repeatable method was the next task. In **Chapter 5**, CuGaO₂ films were deposited at room temperature by magnetron sputtering using a CuGaO₂ target. However, the quantitative analysis of XPS showed that the samples were deficient in oxygen compared to both copper and gallium. Therefore, oxygen was added to the argon working gas during the CuGaO₂ sputter process. The valence band maximum of the resulting CuGaO₂ sample didn't match well with the HOMO level of CH₃NH₃PbI₃. More optimizations of sputter parameters were conducted to improve the properties of the CuGaO₂ films. Varying the distance between the target and the sample substrate slightly improved the valence band maximum of the resulting CuGaO₂. Sodium doping by evaporation of sodium metal on the surface of the sputtered CuGaO₂ sample directly improved the VBM position and still had positive influence on the band alignment with the perovskite layer. CuGaO₂ as a p-type semiconductor was prepared at room temperature by sputtering to be the hole conductor in the top perovskite cell and one of components of the intermediate tunnel junction. It exhibited good transparency at long wavelengths and an appropriate band gap. Reducing the distance between the target and the sample substrate and adding sodium as dopant optimized the band structure of CuGaO₂ films to make them compatible with the perovskite layer.

At this point, both the low band gap bottom cell and suitable p-type semiconductors as intermediate layer for the monolithic perovskite-CIGSe tandem solar cells were investigated. Thus, in **Chapter 6**, a theoretical model of monolithic perovskite-CIGSe tandem solar cells based on Cu₂O and CuGaO₂ as intermediate layers was constructed for optical and electrical simulations. For the optical simulation, a thickness variation was done to calculate the reflection, transmission and absorption of individual layers to reach a current matching between top and bottom cells, which is the necessary condition to achieve the best performance of a monolithic tandem device. The highest matched current of 20.8 mA/cm² was calculated with a CuGaO₂-based perovskite-CIGSe tandem device. In order to find the maximum photovoltaic performance of a tandem device with 20.8 mA/cm² current density, a series of calculations based on the equivalent circuit of the monolithic tandem solar cells was carried out and the optimal power conversion efficiency was estimated to be 30.3% with a V_{oc} of 1.75 V and a fill factor of 0.83. Optical and electrical simulations are important to predict the photovoltaic performance and analyze the recombination losses of monolithic tandem solar cells. As shown in this chapter, Cu₂O and CuGaO₂ are promising candidates as intermediate layers for the monolithic perovskite-CIGSe tandem solar cells.

In conclusion, an intensive study of the monolithic perovskite-CIGSe tandem solar cells was done, especially on the part of the low band gap chalcopyrite solar cell as bottom cell prepared by molecular ink with a non-vacuum, simple direct approach, p-type semiconductors Cu₂O and CuGaO₂ as intermediate layers serving as hole transport material and one component of the tunnel junction, and also the potential performance of tandem device was predicted by the optical simulation. The potential

of Cu_2O and CuGaO_2 over organic materials was shown by the electrical simulation. The experimental work presented in chapters 3, 4 and 5 show the key factors of fabricating the monolithic perovskite-CIGSe tandem solar cells. The theoretical simulation in chapter 6 is done to predict the promising efficiency of tandem devices and the use of Cu_2O and CuGaO_2 as intermediate layer compared with organic materials.

8 Outlook

According to the above conclusions, future research should focus on the following topics:

First, as possible bottom cell material for tandem devices, $\text{CuIn}(\text{S}, \text{Se})_2$ prepared from a molecular ink exhibits an appropriately narrow band gap, and can be prepared with a low cost and simple fabricating process. However, the photoconversion efficiency is insufficient to match with a perovskite top cell which has a PCE above 15%. In order to reach a higher efficiency, improvements of the absorber quality are necessary, which can of course be achieved by using the standard co-evaporation or sequential process. If wet processing methods are preferred, a spin-coating process involving pre-heating and repeating deposition cycles several times was used. During every step, more impurities can be introduced by the handling, which can have a negative influence on the quality of absorber films. On the other hand, using an inkjet printing method can reduce this source of contamination and also lead to more homogeneous absorber films, leading to higher efficiency and decreasing the production time [33]. Another possibility to improve the device performance is the optimization of the precursor properties like composition and structure. In the preparation described here, the copper-to-indium ratio was fixed at 0.9, which makes the absorber copper poor compared to the stoichiometric compound. The atomic ratio of $\text{CuIn}(\text{S}, \text{Se})_2$ has a significant impact on the device performance as described in the introduction section [139], and varying this can improve the absorber quality. Adjusting the annealing steps is also one way to enhance the photovoltaic efficiency. The grain growth and defects generation are strongly influenced by annealing steps. A higher temperature annealing step was added to grow large grains, while a more complicated multistage annealing process can be applied to the fabrication according to the need of grain growth model. Therefore, there is still room for improving the solar cell efficiency by optimizing the CIGSe absorber to match the performance with the top cell perovskite of the monolithic perovskite-CIGSe tandem solar cells.

Secondly, for the p-type semiconductor as an intermediate layer, our original intention was to prepare Cu_2O thin films with appropriate band gap and good conductivity by a simple sputtering approach, however, the subsequently deposited perovskite degraded and showed a bad wetting behavior on the sputtered Cu_2O samples. Therefore, a wet chemical method was tried, which works well with perovskite solar cells. Although the working cell with over 9% of PCE prepared with the wet chemical technique shows that Cu_2O is a promising material as hole transport layer and intermediate tunnel junction component in the perovskite-CIGSe tandem solar cells, looking for better preparation methods is still needed, which are easily operated and not influenced by human factors. Wet chemical or spin-coating techniques usually have shortcomings, such as low-throughput, individual errors, requiring truly soluble precursors and also forming low conductivity films. On the other hand, the reactive rf magnetron sputtering approach is established as the process of choice for the deposition of industrial coatings, which are wear-resistant,

corrosion-resistant, have low friction, and good optical and electrical properties [164, 165]. Sputter-deposition also meets the requirement for the intermediate layer of tandem solar cells to be deposited at low temperatures in order not to destroy the bottom CIGSe solar cells. As a consequence, searching for other p-type semiconductors as hole transport layer and tunnel junction component by simple preparation techniques is a significant topic for perovskite-CIGSe tandem solar cells.

Thirdly, as described in the induction chapter, inorganic hole transport materials are promising candidates in replacing organic HTM in PVK devices and monolithic perovskite-CIGSe tandem solar cells. As this intermediate layer serves not only as the p-contact of the top PVK, but also as one of the components of the intermediate tunnel junction consisting of a highly p doped semiconductor and a highly n doped semiconductor in monolithic perovskite-CIGSe tandem solar cells, this intermediate layer should meet some requirements, such as transparency, good conductivity, stability, low-temperature preparation, and suitable band positions. In order to enhance the properties of CuGaO_2 films including the conductivity, adding other dopants can be a direction of future research work. Although sodium doping was tried to improve the properties of CuGaO_2 films, the effect was not obvious. Some research studied the effect of magnesium doping on the hole conductivity of CuGaO_2 and the conductivity increased by one order of magnitude after Mg doping [190, 191]. So doping with Mg should be tried in the future. In addition, the research on the intermediate tunnel junction which is a decisive factor for efficient charge carrier transport in tandem solar cell needs more attention. The matched band alignment between CuGaO_2 and perovskite layer has been taken into account, while the interface of highly doped n-type TCO of bottom cell and CuGaO_2 also need to be investigated to achieve a high photovoltaic efficiency.

Finally, the electrical simulation for the entire perovskite-CIGSe tandem solar cells is a very intuitive analysis tool to study the limiting factors of tandem devices and effects of individual interfaces on the overall performance. However, it is not contained in this thesis, because the SCAPS program used for electrical simulation cannot simulate the complicated structures of tandem devices, especially the tunnel junction consisting of highly doped p-type and n-type semiconductors between top and bottom cell. SCAPS has no algorithm for a charge transfer through this junction. To optimize parameters for allowing charge carriers through the tunnel junction is a difficult part of the electrical simulation for the perovskite-CIGSe tandem solar cells. Therefore, additional work is required to complete the theoretical analysis of the monolithic perovskite-CIGSe tandem solar cell using inorganic p-type semiconductors as intermediate and hole transport layers.

In general, the crucial parts of the monolithic perovskite-CIGSe tandem solar cells have been investigated and discussed. Owing to the new-development of perovskite-CIGSe multi-junction devices, much work remains to be done to understand the fundamental properties and to achieve high performance. Additionally, improved long-term stability, reproducibility and large-scale production also need to be examined.

9 Appendix

9.1 The refractive indices of individual layers

Figure 9.1 shows the optical constants n and k of individual layers of the monolithic perovskite-CIGSe tandem solar cells, which are applied to the optical simulation of tandem devices.

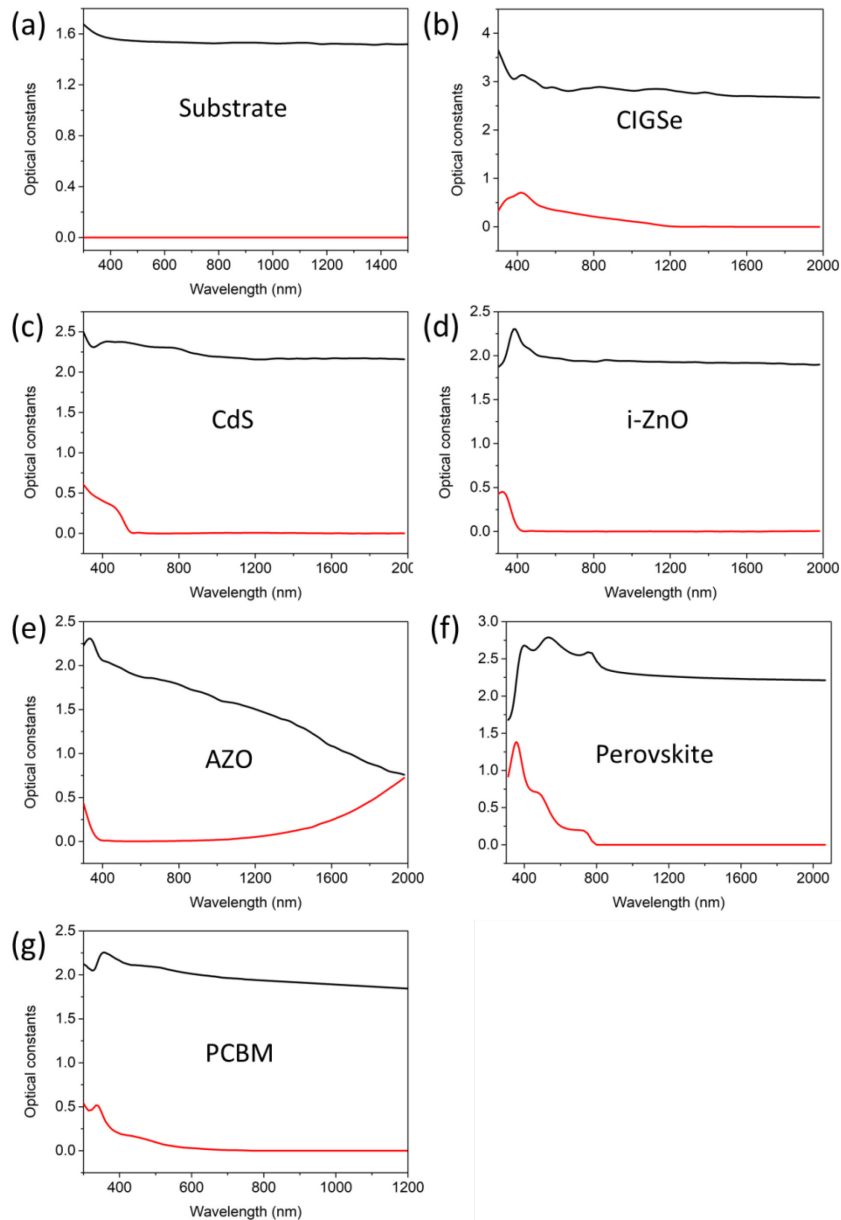


Figure 9.1 The optical constants of individual layers of the monolithic perovskite-CIGSe tandem solar cells, n : black lines; k : red lines. (a) substrate [104]; (b) CIGSe [104]; (c) CdS [104]; (d) i-ZnO [104]; (e) ZnO:Al (AZO) [104]; (f) $\text{CH}_3\text{NH}_3\text{PbI}_3$ [156]; (g) PCBM [200].

9.2 Simulation by SCAPS of single junction perovskite solar cells

The electrical simulation of solar cell is performed by SCAPS, which is a computer-based software tool and is applicable to the analysis of homo- and heterojunctions, multi-junctions and Schottky barrier photovoltaic devices [203, 204]. In order to understand the effect of an inorganic material as an intermediate hole transport layer for the perovskite-CIGSe tandem solar cells, various parameters are optimized, such as absorber thickness, the defect densities of absorber layer.

A single junction perovskite solar cell model is illustrated in figure 9.2, with Cu_2O as an example hole transport material, perovskite ($\text{CH}_3\text{NH}_3\text{PbI}_3$) as an active layer, PCBM as electron transport material. As designed previously, the perovskite-CIGSe tandem consists of a reverse standard structure of perovskite solar cell, which means the ETM is facing the incident light and the HTM is deposited first. The band structure of Cu_2O is taken from the sputtered sample, discussed in the chapter 4. The valence band maximum of the Cu_2O film is -5.05 eV, higher than the HOMO energy level of the $\text{CH}_3\text{NH}_3\text{PbI}_3$ layer (-5.5 eV), thus leading to the extraction of holes at the interface between the Cu_2O and the $\text{CH}_3\text{NH}_3\text{PbI}_3$ film. In addition, the conduction band edge of the Cu_2O film (-2.60 eV) is much higher than the LUMO level of the $\text{CH}_3\text{NH}_3\text{PbI}_3$ layer (-3.9 eV), which prevents electrons from the perovskite reaching the Cu_2O layer effectively. On the other side, the HOMO level of PCBM is lower than that of the perovskite layer and PCBM exhibits slight deeper LUMO level than perovskite layer, insuring the electrons and holes drifted to the contacts successfully.

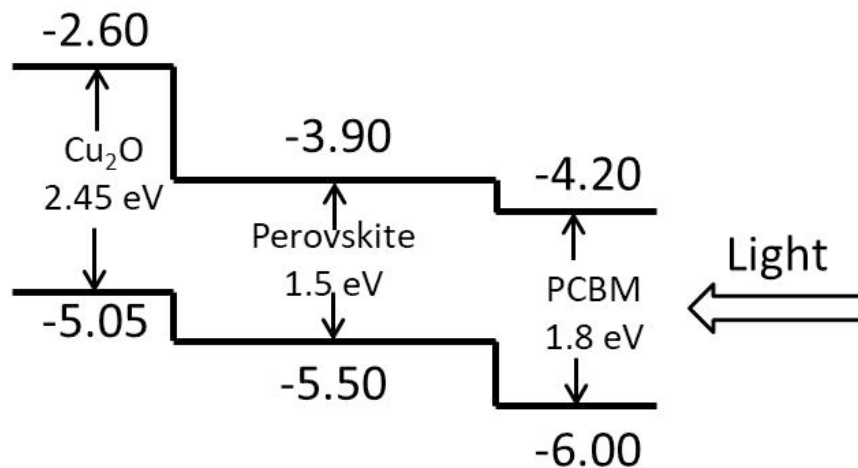


Figure 9.2 Illustration of device structure in simulation: Cu_2O as an example hole transport material.

After the single junction perovskite solar cell model is built, various electrical parameters are input to the program, i.e. thickness, band gap (E_g), electron affinity (χ), dielectric permittivity (ϵ), CB effective density of states (N_C), VB effective density of states (N_V), electron thermal velocity (v_{thn}), hole thermal velocity (v_{thp}), electron mobility (μ_n), hole mobility (μ_p), acceptor density (N_A), donor density (N_D), all traps

(defects) (N_t). The detailed parameters of Cu_2O , PEDOT:PSS, MAPI_3 and PCBM are listed in table 9.1. In order to compare the influence of different HTM on the performance of PVK devices, the parameters of MAPI_3 and PCBM are fixed and the thickness of Cu_2O and PEDOT:PSS are the same. All the values and references of the relevant parameters are presented in the table 9.1.

Table 9.1 Parameters of single junction perovskite solar cells with Cu_2O as HTM for the electrical simulation by SCAPS.

| Parameters | Cu_2O | ref | PEDOT:PSS | ref | MAPI_3 | ref | PCBM | ref |
|---|-----------------------|----------------|-----------|------------|-------------------|-------|------|-------|
| Thickness (nm) | 20 | | 20 | | 450 (variable) | | 25 | |
| Band gap (eV) | 2.45 | | 1.5 | [205, 206] | 1.5 | [207] | 1.8 | [180] |
| Electron affinity (eV) | 2.6 | | 3.6 | [205, 206] | 3.9 | [207] | 4.2 | [180] |
| Dielectric permittivity relative | 7.11 | [208] | 10 | [205] | 6.5 | [204] | 3.9 | [204] |
| CB effective density of states (cm^{-3}) | 2.02E17 | [208] | 1E21 | [205] | 2.75E18 | [209] | 1E21 | [210] |
| VB effective density of states (cm^{-3}) | 1.10E19 | [208] | 1E21 | [205] | 3.9E18 | [209] | 1E21 | [210] |
| Electron thermal velocity (cm/s) | 1E7 | | 1E7 | | 1E7 | | 1E7 | |
| Hole thermal velocity (cm/s) | 1E7 | | 1E7 | | 1E7 | | 1E7 | |
| Electron mobility (cm^2/Vs) | 200 | [211] | 1 | [205] | 10 | [212] | 1E-3 | [204] |
| Hole mobility (cm^2/Vs) | 80 | [213] | 40 | [205] | 10 | [212] | 2E-3 | [204] |
| N_D | 0 | | 0 | | 1E13 | [214] | 1E18 | |
| N_A | 1E18 | [158, 215-217] | 1E19 | [205] | 1E13 | [214] | 0 | |

As in the procedure shown previously, the working condition is set at 300 K under

AM1.5G solar illumination conditions (100 mW/cm^2) and the I-V measurement is chosen from 0 to 1.5 V. The J-V curves of PEDOT:PSS-based and Cu_2O -based perovskite solar cells are shown in figure 9.3 and the comparison of PV parameters (J_{sc} , V_{oc} , FF and PCE) is presented in table 9.2. The power conversion efficiency of the Cu_2O -based PVK device is 28.7%, which is much higher than that of the PEDOT:PSS-based device. The Cu_2O -based PVK device exhibits a very high open circuit voltage of 1.37 V, similar to the band gap of the $\text{CH}_3\text{NH}_3\text{PbI}_3$ layer and higher than that of the PEDOT:PSS-based device of 0.95 V. According to the equation 6.4, the open circuit voltage V_{oc} is dependent on the short circuit current density J_{sc} and saturation current density J_0 . Since the Cu_2O -based device shows similar J_{sc} to the PEDOT:PSS-based device, the difference of V_{oc} depends on the J_0 , which is a measure of the "leakage" of carriers across the p-n junction in reverse bias. This leakage is a result of charge carrier recombination in the neutral regions on either side of the junction. The hole mobility of Cu_2O ($80 \text{ cm}^2/\text{Vs}$) is higher than PEDOT:PSS ($40 \text{ cm}^2/\text{Vs}$), indicating that Cu_2O facilitates hole transportation much more efficiently than PEDOT:PSS, which is one of the strengths of inorganic HTM replacing organic HTM. Therefore, the charge carrier recombination in the Cu_2O -based device could be suppressed much more effectively compared with the PEDOT:PSS-based device, resulting in a lower saturation current density in the Cu_2O -based cell. From the dark J-V curve shown in figure 9.3 b, the J_0 of the Cu_2O cell is significantly lower than that of the PEDOT:PSS-based device, thereby leading to a larger V_{oc} of the Cu_2O -based device. Eventually, the power conversion efficiency of Cu_2O -based PVK device outperforms the PEDOT:PSS-based device, demonstrating that the inorganic Cu_2O as hole transport material for PVK devices has more favourable properties compared to the organic material PEDOT:PSS and shows much promise to be an intermediate layer for the monolithic perovskite-CIGSe tandem solar cells. In addition, the larger band gap of Cu_2O is more suitable for tandem devices, allowing more incident light to pass through the bottom cell.

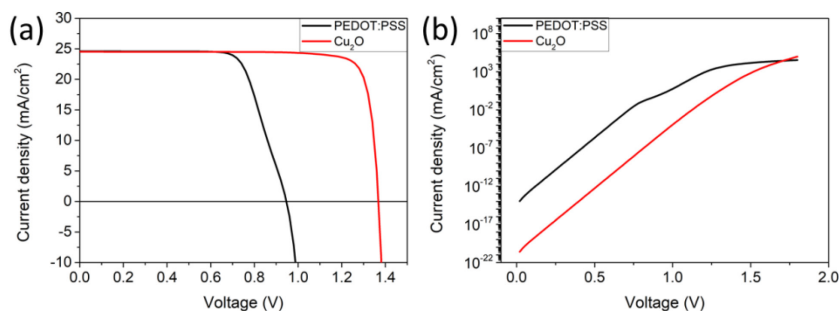


Figure 9.3 The simulated J-V curves of PEDOT:PSS-based and Cu_2O -based perovskite solar cells (a) under illumination; (b) in the dark.

TABLE ON NEW PAGE

Table 9.2 Comparison of Open-Circuit Photovoltage (V_{oc}), Short-Circuit Photocurrent Density (J_{sc}), Fill Factor (FF), and Photoconversion Efficiency (η) for PEDOT:PSS-based and Cu_2O -based perovskite solar cells.

| Performance | J_{sc} (mA/cm ²) | V_{oc} (V) | FF | η (%) |
|-------------|--------------------------------|--------------|------|------------|
| PEDOT:PSS | 24.6 | 0.95 | 0.73 | 16.9 |
| Cu_2O | 24.5 | 1.37 | 0.85 | 28.7 |

The thickness of the perovskite layer is varied from 100 nm to 800 nm as shown in figure 9.4. The simulation device is based on the structure of $Cu_2O/CH_3NH_3PbI_3/PCBM$. The thicker the absorber layer is, the better efficiency is achieved. By tuning the thickness of the absorber layer, the maximum power conversion efficiency is predicted to be 30.8% at 800 nm, J_{sc} is 26.2 mA/cm², V_{oc} is 1.37 V, and the fill factor is 85.68%. However, the rate of increment of efficiency slows down after 400 nm. In real device fabrication, the thickness of the perovskite layer is normally limited to below 1 μ m, no matter if it is a vapour-deposited film or a solution-processed film. If the perovskite film is too thin, then it will not absorb sufficient incident light. In addition, the absence of material in some regions such as pinholes will result in direct contact of the p-type and n-type materials, leading to a shunt or lower fill factor and open circuit voltage of the device [218, 219]. If the film is too thick, there is a significant chance that the electrons and holes (or excitons) diffusion length will be shorter than the film thickness, and that the charge will therefore not be collected at the p-type and n-type heterojunctions [55]. As described in the optical simulation part, the thickness of the perovskite layer has great influence on the current matching and photovoltaic performance of the tandem solar cells. Hence, the thickness of the perovskite layer can be determined in a certain range. For the optical simulation, the best efficiency and current matching of a Cu_2O -based tandem device are achieved at 435 nm of perovskite film. For the electrical simulation, the efficiency of 450 nm thick film is 28.7% with a J_{sc} of 24.5 mA/cm², a V_{oc} of 1.37 V and a fill factor of 85.46%.

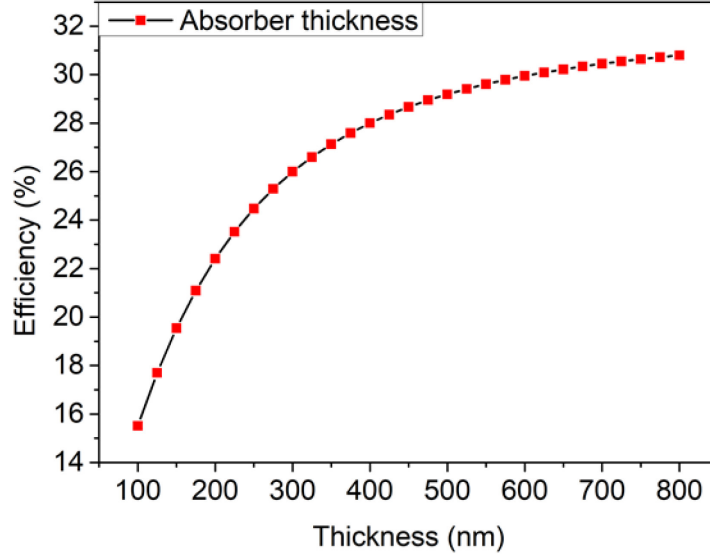


Figure 9.4 Variation of photovoltaic performance by varying the thickness of perovskite layer.

Table 9.3 and figure 9.5 represent the detailed parameters of defects in single junction perovskite solar cells with Cu_2O as HTM and the variation of PV parameters with the defect densities. In the absorber layer, charge carriers generation and recombination have a great influence on the performance of the device. Therefore, the defect densities of the perovskite layer deserve a discussion on device performance. The process of doping in the absorber layer is the main reason to form the defects [204]. The energetic distribution of defects can be described by single, uniform and Gaussian model in the simulation program. Among them, the Gaussian-distribution model is good to explain the defects levels of an absorber layer. The Shockley-Read Hall non-radiative center model (SRH model) is known to clearly explain the defect density of absorber layer, which is the recombination centers appearing at deep energy levels [220]. The equation of the SRH model is:

$$R = \frac{np - n_i^2}{\tau_p \left(n + N_c e^{\frac{(E_g - E_t)}{kT}} \right) + \tau_n \left(p + N_v e^{\frac{E_t}{kT}} \right)} \quad 9.1$$

Where n and p are the concentration of electrons and holes, n_i^2 will be neglected when $qV > kT$. τ_n and τ_p are the life time of electron and hole. From this equation, the recombination resistance decreases by increasing the defect densities. Therefore, a large number of defects existing in the low-quality perovskite layer will lead to an increase of recombination and the reduction of diffusion length of charge carriers. As a result, the life time of charge carriers will be decreased. Eventually, the defect density has a great effect on the performance of a device. The detailed parameters of the considered defects are listed in the table 9.3. The defect density is varied between 10^{12} cm^{-3} and 10^{17} cm^{-3} . From figure 9.5, the PV parameters are shown by increasing the defect density from 10^{12} cm^{-3} to 10^{17} cm^{-3} , including the open circuit

voltage, short circuit current density, fill factor and power conversion efficiency. The V_{oc} and fill factor drop dramatically when the defect density is increasing. However, the J_{sc} remains around 24 mA/cm² first, and then decreases to 12 mA/cm². The total efficiency decreases from 28% to 6% by varying the defect density from 10¹² cm⁻³ to 10¹⁷ cm⁻³. In order to achieve good efficiency, it is necessary to improve the quality of the perovskite layer and decrease the defect density of the absorber layer.

Table 9.3 Parameters of defects in single junction perovskite solar cells with Cu₂O as HTM.

| Parameters | Defects |
|--|--------------------------|
| Defect type | Single donor or acceptor |
| Capture cross section electrons (cm ²) | 1E-17 |
| Capture cross section holes (cm ²) | 1E-15 |
| Energetic distribution | Gaussian |
| Reference for defect energy level E_t | Above EV |
| Energy level with respect to Reference (eV) | 0.6 |
| N_t total (1/cm ³) | 1E13 (variable) |

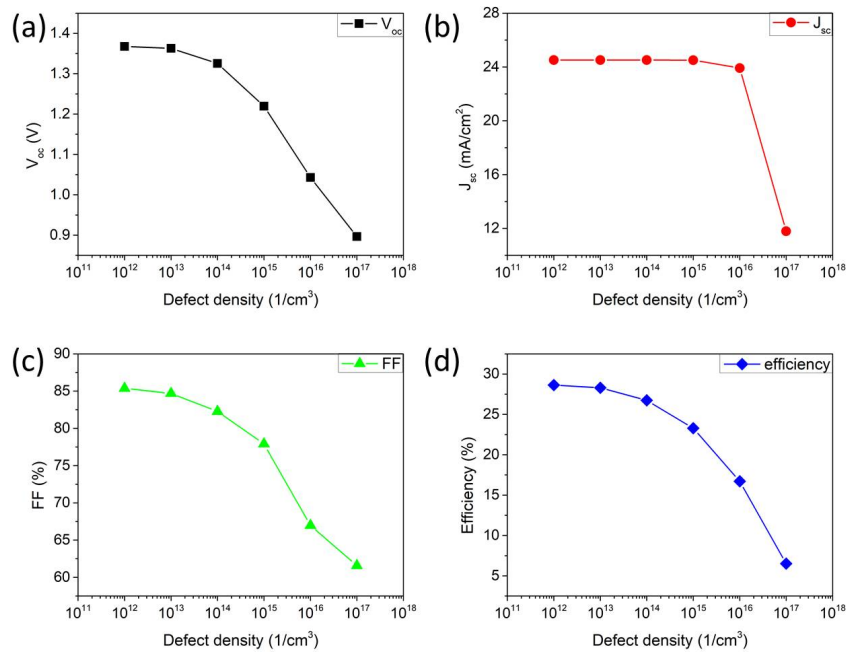


Figure 9.5 Variation of PV parameters by varying the defect density.

List of Acronyms

| | |
|----------------------------|--|
| Si | Silicon |
| CIGSe | $\text{Cu}(\text{In,Ga})(\text{S, Se})_2$ |
| PVK | Perovskite solar cells |
| V_{oc} | Open circuit voltage |
| J_{sc} | Short circuit current density |
| FF | Fill Factor |
| η | Photoconversion Efficiency |
| S-Q | Shockley and Queisser |
| CdTe | Cadmium telluride |
| i-ZnO | Intrinsic ZnO |
| AZO | Al doped ZnO |
| E_g | Band gap |
| SCR | Space charge region |
| CBD | Chemical bath deposition |
| RTP | Rapid thermal processing |
| E_a | Activation energy |
| CH_3NH_3^+ | Methylammonium cation |
| DSCs | Dye sensitized solar cells |
| ETM | Electron transport materials |
| HTM | Hole transport materials |
| MBE | Molecular beam epitaxy |
| MOCVD | Metalorganic chemical vapor deposition |
| CZTS | $\text{Cu}_2\text{ZnSn}(\text{S, Se})_4$ |
| PCBM | [6,6]-phenyl-C61-butyric acid methyl ester |
| HOMO | Highest occupied molecular orbital |
| LUMO | Lowest unoccupied molecular orbital |
| J_{topsc} | Short circuit current density of the top cell |
| J_{botsc} | Short circuit current density of the bottom cell |

| | |
|----------------------|--|
| J_{matchsc} | Highest matched current density |
| IIHTM | Intermediate inorganic hole transport material |
| XRD | X-ray diffraction |
| SEM | Scanning electron microscopy |
| 4PP | Four point probe resistivity measurements |
| XPS | X-ray photoelectron spectroscopy |
| UPS | Ultraviolet photoelectron spectroscopy |
| SCAPS | A Solar Cell Capacitance Simulator |
| χ | Electron affinity |
| ϵ | Dielectric permittivity |
| N_C | CB effective density of states |
| N_V | VB effective density of states |
| v_{thn} | Electron thermal velocity |
| v_{thp} | Hole thermal velocity |
| μ_n | Electron mobility |
| μ_p | Hole mobility |
| N_A | Acceptor density |
| N_D | Donor density |
| N_t | Defects |
| SPV | Surface photovoltage |
| MBE | Molecular beam epitaxy |
| VBM | Valance band maximum |
| DMSO | Dimethyl sulfoxide |
| EGBE | Ethylene glycol butyl ether |
| EQE | External quantum efficiency |
| WF | Work function |
| VB | Valence band |
| CB | Conduction band |
| BE | Binding energy |
| OPV | Organic photovoltaic devices |

| | |
|------------|---|
| XRR | X-ray reflectometry |
| TCO | Transparent conducting oxide |
| R/T/Abs | Reflection, transmission and absorption |
| d | Thickness |
| E_c | Conduction band minimum |
| E_F | Fermi level |
| E_{kin} | Kinetic energy level |
| E_{pass} | Pass energy |
| E_V | Valence band maximum |
| h | Planck constant |
| $h\nu$ | Photon energy |
| k | Boltzmann constant |

Reference

- [1] A. Rockett, R.W. Birkmire, Cuinse₂ for Photovoltaic Applications, *J Appl Phys*, 70 (1991) R81-R97.
- [2] A. Shah, P. Torres, R. Tscharnner, N. Wyrsh, H. Keppner, Photovoltaic technology: The case for thin-film solar cells, *Science*, 285 (1999) 692-698.
- [3] H. Azimi, Y. Hou, C.J. Brabec, Towards low-cost, environmentally friendly printed chalcopyrite and kesterite solar cells, *Energ Environ Sci*, 7 (2014) 1829-1849.
- [4] B. Parida, S. Iniyar, R. Goic, A review of solar photovoltaic technologies, *Renewable and sustainable energy reviews*, 15 (2011) 1625-1636.
- [5] K. Masuko, M. Shigematsu, T. Hashiguchi, D. Fujishima, M. Kai, N. Yoshimura, T. Yamaguchi, Y. Ichihashi, T. Mishima, N. Matsubara, T. Yamanishi, T. Takahama, M. Taguchi, E. Maruyama, S. Okamoto, Achievement of More Than 25% Conversion Efficiency With Crystalline Silicon Heterojunction Solar Cell, *Ieee J Photovolt*, 4 (2014) 1433-1435.
- [6] K. Yoshikawa, H. Kawasaki, W. Yoshida, T. Irie, K. Konishi, K. Nakano, T. Uto, D. Adachi, M. Kanematsu, H. Uzu, K. Yamamoto, Silicon heterojunction solar cell with interdigitated back contacts for a photoconversion efficiency over 26%, *Nat Energy*, 2 (2017).
- [7] S.F. K.K., http://www.solar-frontier.com/eng/news/2019/0117_press.html.
- [8] W.S. Yang, B.W. Park, E.H. Jung, N.J. Jeon, Y.C. Kim, D.U. Lee, S.S. Shin, J. Seo, E.K. Kim, J.H. Noh, S.I. Seok, Iodide management in formamidinium-lead-halide-based perovskite layers for efficient solar cells, *Science*, 356 (2017) 1376-+.
- [9] M. Becquerel, Mémoire sur les effets électriques produits sous l'influence des rayons solaires, *Comptes rendus hebdomadaires des séances de l'Académie des Sciences*, 9 (1839) 561-567.
- [10] A. Goetzberger, C. Hebling, H.-W. Schock, Photovoltaic materials, history, status and outlook, *Materials Science and Engineering: R: Reports*, 40 (2003) 1-46.
- [11] A. Goetzberger, J. Knobloch, B. Voss, *Crystalline silicon solar cells*, Wiley Online Library, 1998.
- [12] M.A. Green, *Silicon solar cells: advanced principles & practice*, Centre for photovoltaic devices and systems, University of New South Wales, 1995.
- [13] A. Polman, M. Knight, E.C. Garnett, B. Ehrler, W.C. Sinke, Photovoltaic materials: Present efficiencies and future challenges, *Science*, 352 (2016) 307-+.
- [14] W. Shockley, H.J. Queisser, Detailed Balance Limit of Efficiency of P-N Junction Solar Cells, *J Appl Phys*, 32 (1961) 510-&.

- [15] A. Devos, Detailed Balance Limit of the Efficiency of Tandem Solar-Cells, *J Phys D Appl Phys*, 13 (1980) 839-846.
- [16] J.W. Lee, Y.T. Hsieh, N. De Marco, S.H. Bae, Q. Han, Y. Yang, Halide Perovskites for Tandem Solar Cells, *J Phys Chem Lett*, 8 (2017) 1999-2011.
- [17] N.N. Lal, Y. Dkhissi, W. Li, Q. Hou, Y.B. Cheng, U. Bach, Perovskite Tandem Solar Cells, *Adv Energy Mater*, (2017).
- [18] T. Todorov, T. Gershon, O. Gunawan, Y.S. Lee, C. Sturdevant, L.Y. Chang, S. Guha, Monolithic Perovskite-CIGS Tandem Solar Cells via In Situ Band Gap Engineering, *Adv Energy Mater*, 5 (2015).
- [19] Y. Wang, R. Wenisch, R. Schlatmann, I. Laueremann, Inorganic Materials as Hole Selective Contacts and Intermediate Tunnel Junction Layer for Monolithic Perovskite-CIGSe Tandem Solar Cells, *Adv Energy Mater*, 8 (2018) 1801692.
- [20] S. Albrecht, B. Rech, Perovskite solar cells: On top of commercial photovoltaics, *Nat Energy*, 2 (2017) 16196.
- [21] I. Celik, A.B. Phillips, Z.N. Song, Y.F. Yan, R.J. Ellingson, M.J. Heben, D. Apul, Environmental analysis of perovskites and other relevant solar cell technologies in a tandem configuration, *Energ Environ Sci*, 10 (2017) 1874-1884.
- [22] J. Ramanujam, U.P. Singh, Copper indium gallium selenide based solar cells—a review, *Energ Environ Sci*, 10 (2017) 1306-1319.
- [23] A.S. Brown, M.A. Green, Detailed balance limit for the series constrained two terminal tandem solar cell, *Physica E: Low-dimensional Systems and Nanostructures*, 14 (2002) 96-100.
- [24] C. Honsberg, S. Bowden, <http://www.pveducation.org/pvcdrom/tandem-cells>.
- [25] J. Poortmans, V. Arkhipov, *Thin film solar cells: fabrication, characterization and applications*, John Wiley & Sons, 2006.
- [26] A. Chirila, S. Buecheler, F. Pianezzi, P. Bloesch, C. Gretener, A.R. Uhl, C. Fella, L. Kranz, J. Perrenoud, S. Seyrling, R. Verma, S. Nishiwaki, Y.E. Romanyuk, G. Bilger, A.N. Tiwari, Highly efficient Cu(In,Ga)Se₂ solar cells grown on flexible polymer films, *Nat Mater*, 10 (2011) 857-861.
- [27] R. Caballero, C. Kaufmann, V. Efimova, T. Rissom, V. Hoffmann, H. Schock, Investigation of Cu (In, Ga) Se₂ thin - film formation during the multi - stage co - evaporation process, *Progress in Photovoltaics: Research and Applications*, 21 (2013) 30-46.
- [28] J. Lindahl, U. Zimmermann, P. Szaniawski, T. Törndahl, A. Hultqvist, P. Salomé, C. Platzer-Björkman, M. Edoff, Inline Cu (In, Ga) Se₂ Co-evaporation for High-Efficiency Solar

Cells and Modules, *Ieee J Photovolt*, 3 (2013) 1100-1105.

[29] C.-H. Huang, C.-P. Lin, Y.-L. Jan, Characteristics of CIGS photovoltaic devices co-evaporated with various Se flux rates at low temperatures, *Semicond Sci Tech*, 31 (2016) 085004.

[30] Y. Aida, V. Depredurand, J.K. Larsen, H. Arai, D. Tanaka, M. Kurihara, S. Siebentritt, Cu - rich CuInSe_2 solar cells with a Cu - poor surface, *Progress in photovoltaics: Research and Applications*, 23 (2015) 754-764.

[31] M. Turcu, O. Pakma, U. Rau, Interdependence of absorber composition and recombination mechanism in Cu (In, Ga)(Se, S)₂ heterojunction solar cells, *Appl Phys Lett*, 80 (2002) 2598-2600.

[32] K. Siemer, J. Klaer, I. Luck, J. Bruns, R. Klenk, D. Bräunig, Efficient CuInS_2 solar cells from a rapid thermal process (RTP), *Sol Energ Mat Sol C*, 67 (2001) 159-166.

[33] X. Lin, R. Klenk, L. Wang, T. Köhler, J. Albert, S. Fiechter, A. Ennaoui, M.C. Lux-Steiner, 11.3% efficiency Cu(In,Ga)(S,Se)_2 thin film solar cells via drop-on-demand inkjet printing, *Energy Environ. Sci.*, 9 (2016) 2037-2043.

[34] Y. Wang, X. Lin, L. Wang, T. Köhler, M.C. Lux - Steiner, R. Klenk, Low band - gap CuIn (S, Se)_2 thin film solar cells using molecular ink with 9.5% efficiency, *physica status solidi (c)*, (2017).

[35] D. Tiwari, T. Koehler, X. Lin, A. Sarua, R. Harniman, L. Wang, R. Klenk, D.J. Fermin, Single Molecular Precursor Solution for CuIn (S, Se)_2 Thin Films Photovoltaic Cells: Structure and Device Characteristics, *ACS applied materials & interfaces*, 9 (2017) 2301-2308.

[36] A.R. Uhl, J.K. Katahara, H.W. Hillhouse, Molecular-ink route to 13.0% efficient low-bandgap CuIn(S,Se)_2 and 14.7% efficient Cu(In,Ga)(S,Se)_2 solar cells, *Energy Environ. Sci.*, 9 (2016) 130-134.

[37] I. Repins, M.A. Contreras, B. Egaas, C. DeHart, J. Scharf, C.L. Perkins, B. To, R. Noufi, 19.9% - efficient $\text{ZnO/CdS/CuInGaSe}_2$ solar cell with 81.2% fill factor, *Progress in Photovoltaics: Research and applications*, 16 (2008) 235-239.

[38] S. Jung, S. Ahn, J.H. Yun, J. Gwak, D. Kim, K. Yoon, Effects of Ga contents on properties of CIGS thin films and solar cells fabricated by co-evaporation technique, *Curr Appl Phys*, 10 (2010) 990-996.

[39] J.H. Werner, J. Mattheis, U. Rau, Efficiency limitations of polycrystalline thin film solar cells: case of Cu (In, Ga) Se_2 , *Thin Solid Films*, 480 (2005) 399-409.

[40] R. Klenk, Characterisation and modelling of chalcopyrite solar cells, *Thin solid films*, 387 (2001) 135-140.

- [41] V. Nadenau, U. Rau, A. Jasenek, H.W. Schock, Electronic properties of CuGaSe₂-based heterojunction solar cells. Part I. Transport analysis, *J Appl Phys*, 87 (2000) 584-593.
- [42] X.Z. Lin, J. Kavalakkatt, A. Ennaoui, M.C. Lux-Steiner, Cu₂ZnSn(S, Se)₄ thin film absorbers based on ZnS, SnS and Cu₃SnS₄ nanoparticle inks: Enhanced solar cells performance by using a two-step annealing process, *Sol Energ Mat Sol C*, 132 (2015) 221-229.
- [43] H.L. Wells, ART. XVI.--On the Coesium-and the Potassium-Lead Halides, *American Journal of Science (1880-1910)*, 45 (1893) 121.
- [44] D. Weber, CH₃NH₃PbX₃, ein Pb (II)-system mit kubischer perowskitstruktur/CH₃NH₃PbX₃, a Pb (II)-system with cubic perovskite structure, *Zeitschrift für Naturforschung B*, 33 (1978) 1443-1445.
- [45] D. Weber, CH₃NH₃SnBr_xI_{3-x} (x= 0-3), ein Sn (II)-System mit kubischer Perowskitstruktur/CH₃NH₃SnBr_xI_{3-x} (x= 0-3), a Sn (II)-System with Cubic Perovskite Structure, *Zeitschrift für Naturforschung B*, 33 (1978) 862-865.
- [46] G. Xing, N. Mathews, S.S. Lim, N. Yantara, X. Liu, D. Sabba, M. Grätzel, S. Mhaisalkar, T.C. Sum, Low-temperature solution-processed wavelength-tunable perovskites for lasing, *Nat Mater*, 13 (2014) 476.
- [47] A. Kojima, K. Teshima, Y. Shirai, T. Miyasaka, Organometal halide perovskites as visible-light sensitizers for photovoltaic cells, *J Am Chem Soc*, 131 (2009) 6050-6051.
- [48] J.-H. Im, C.-R. Lee, J.-W. Lee, S.-W. Park, N.-G. Park, 6.5% efficient perovskite quantum-dot-sensitized solar cell, *Nanoscale*, 3 (2011) 4088-4093.
- [49] Y. Bai, H. Yu, Z. Zhu, K. Jiang, T. Zhang, N. Zhao, S. Yang, H. Yan, High performance inverted structure perovskite solar cells based on a PCBM: polystyrene blend electron transport layer, *J Mater Chem A*, 3 (2015) 9098-9102.
- [50] L. Meng, J. You, T.-F. Guo, Y. Yang, Recent advances in the inverted planar structure of perovskite solar cells, *Accounts of chemical research*, 49 (2015) 155-165.
- [51] H.S. Jung, N.G. Park, Perovskite solar cells: from materials to devices, *Small*, 11 (2015) 10-25.
- [52] J. Chen, N.-G. Park, Inorganic Hole Transporting Materials for Stable and High Efficiency Perovskite Solar Cells, *The Journal of Physical Chemistry C*, (2018).
- [53] I. Chung, B. Lee, J. He, R.P. Chang, M.G. Kanatzidis, All-solid-state dye-sensitized solar cells with high efficiency, *Nature*, 485 (2012) 486.
- [54] H.-S. Kim, C.-R. Lee, J.-H. Im, K.-B. Lee, T. Moehl, A. Marchioro, S.-J. Moon, R. Humphry-Baker, J.-H. Yum, J.E. Moser, Lead iodide perovskite sensitized all-solid-state submicron thin film mesoscopic solar cell with efficiency exceeding 9%, *Scientific reports*, 2

(2012).

[55] M.Z. Liu, M.B. Johnston, H.J. Snaith, Efficient planar heterojunction perovskite solar cells by vapour deposition, *Nature*, 501 (2013) 395-+.

[56] Q. Chen, H.P. Zhou, Z.R. Hong, S. Luo, H.S. Duan, H.H. Wang, Y.S. Liu, G. Li, Y. Yang, Planar Heterojunction Perovskite Solar Cells via Vapor-Assisted Solution Process, *J Am Chem Soc*, 136 (2014) 622-625.

[57] J. Burschka, N. Pellet, S.J. Moon, R. Humphry-Baker, P. Gao, M.K. Nazeeruddin, M. Gratzel, Sequential deposition as a route to high-performance perovskite-sensitized solar cells, *Nature*, 499 (2013) 316-+.

[58] M.M. Lee, J. Teuscher, T. Miyasaka, T.N. Murakami, H.J. Snaith, Efficient hybrid solar cells based on meso-superstructured organometal halide perovskites, *Science*, 338 (2012) 643-647.

[59] J.W. Lee, D.J. Seol, A.N. Cho, N.G. Park, High - Efficiency Perovskite Solar Cells Based on the Black Polymorph of $\text{HC}(\text{NH}_2)_2\text{PbI}_3$, *Adv Mater*, 26 (2014) 4991-4998.

[60] G.E. Eperon, S.D. Stranks, C. Menelaou, M.B. Johnston, L.M. Herz, H.J. Snaith, Formamidinium lead trihalide: a broadly tunable perovskite for efficient planar heterojunction solar cells, *Energ Environ Sci*, 7 (2014) 982-988.

[61] M.H. Kumar, S. Dharani, W.L. Leong, P.P. Boix, R.R. Prabhakar, T. Baikie, C. Shi, H. Ding, R. Ramesh, M. Asta, Lead - free halide perovskite solar cells with high photocurrents realized through vacancy modulation, *Adv Mater*, 26 (2014) 7122-7127.

[62] N.J. Jeon, J.H. Noh, W.S. Yang, Y.C. Kim, S. Ryu, J. Seo, S.I. Seok, Compositional engineering of perovskite materials for high-performance solar cells, *Nature*, 517 (2015) 476.

[63] Y. Yang, Q. Chen, Y.T. Hsieh, T.B. Song, N. De Marco, H.P. Zhou, Y. Yang, Multilayer Transparent Top Electrode for Solution Processed Perovskite/Cu(In,Ga) (Se,S)₂ Four Terminal Tandem Solar Cells, *Acs Nano*, 9 (2015) 7714-7721.

[64] Q. Chen, H. Zhou, Z. Hong, S. Luo, H.-S. Duan, H.-H. Wang, Y. Liu, G. Li, Y. Yang, Planar heterojunction perovskite solar cells via vapor-assisted solution process, *J Am Chem Soc*, 136 (2013) 622-625.

[65] T.L. Amu, Performance Optimization of tin halide Perovskite solar cells via Numerical Simulation, in, 2014.

[66] A.M. Bagher, M.M.A. Vahid, M. Mohsen, Types of solar cells and application, *American Journal of optics and Photonics*, 3 (2015) 94-113.

[67] N. Kour, R. Mehra, Recent Advances in Photovoltaic Technology based on Perovskite Solar Cell-A Review, *International Research Journal of Engineering and Technology*, 4 (2017)

1284-1296.

[68] M. Yamaguchi, S. Wakamatsu, Super-high efficiency solar cell R&D program in Japan, in: Photovoltaic Specialists Conference, 1996., Conference Record of the Twenty Fifth IEEE, IEEE, 1996, pp. 9-11.

[69] G.M. A., H. Yoshihiro, D.E. D., L.D. H., H.E. Jochen, H.B.A. W.Y., Solar cell efficiency tables (version 51), *Progress in Photovoltaics: Research and Applications*, 26 (2018) 3-12.

[70] A. Luque, S. Hegedus, *Handbook of photovoltaic science and engineering*, John Wiley & Sons, 2011.

[71] P. Gao, M. Grätzel, M.K. Nazeeruddin, Organohalide lead perovskites for photovoltaic applications, *Energ Environ Sci*, 7 (2014) 2448-2463.

[72] C.D. Bailie, M.G. Christoforo, J.P. Mailoa, A.R. Bowring, E.L. Unger, W.H. Nguyen, J. Burschka, N. Pellet, J.Z. Lee, M. Gratzel, R. Noufi, T. Buonassisi, A. Salleo, M.D. McGehee, Semi-transparent perovskite solar cells for tandems with silicon and CIGS, *Energ Environ Sci*, 8 (2015) 956-963.

[73] S. Albrecht, M. Saliba, J.P.C. Baena, F. Lang, L. Kegelmann, M. Mews, L. Steier, A. Abate, J. Rappich, L. Korte, Monolithic perovskite/silicon-heterojunction tandem solar cells processed at low temperature, *Energ Environ Sci*, 9 (2016) 81-88.

[74] B. Chen, Y. Bai, Z. Yu, T. Li, X. Zheng, Q. Dong, L. Shen, M. Boccard, A. Gruverman, Z. Holman, Efficient Semitransparent Perovskite Solar Cells for 23.0% - Efficiency Perovskite/Silicon Four - Terminal Tandem Cells, *Adv Energy Mater*, 6 (2016).

[75] J. Werner, C.-H. Weng, A. Walter, L. Fesquet, J.P. Seif, S. De Wolf, B. Niesen, C. Ballif, Efficient monolithic perovskite/silicon tandem solar cell with cell area > 1 cm², *The journal of physical chemistry letters*, 7 (2015) 161-166.

[76] D.P. McMeekin, G. Sadoughi, W. Rehman, G.E. Eperon, M. Saliba, M.T. Horantner, A. Haghighirad, N. Sakai, L. Korte, B. Rech, M.B. Johnston, L.M. Herz, H.J. Snaith, A mixed-cation lead mixed-halide perovskite absorber for tandem solar cells, *Science*, 351 (2016) 151-155.

[77] J. Werner, L. Barraud, A. Walter, M. Bräuninger, F. Sahli, D. Sacchetto, N. Tétreault, B. Paviet-Salomon, S.-J. Moon, C. Allebé, Efficient near-infrared-transparent perovskite solar cells enabling direct comparison of 4-terminal and monolithic perovskite/silicon tandem cells, *ACS Energy Letters*, 1 (2016) 474-480.

[78] K.A. Bush, A.F. Palmstrom, J.Y. Zhengshan, M. Boccard, R. Cheacharoen, J.P. Mailoa, D.P. McMeekin, R.L. Hoyer, C.D. Bailie, T. Leijtens, 23.6%-efficient monolithic perovskite/silicon tandem solar cells with improved stability, *Nat Energy*, 2 (2017) 17009.

[79] F. Fu, T. Feurer, T. Jäger, E. Avancini, B. Bissig, S. Yoon, S. Buecheler, A.N. Tiwari, Low-temperature-processed efficient semi-transparent planar perovskite solar cells for

bifacial and tandem applications, *Nat Commun*, 6 (2015).

[80] L. Kranz, A. Abate, T. Feurer, F. Fu, E. Avancini, J. Löckinger, P. Reinhard, S.M. Zakeeruddin, M. Grätzel, S. Buecheler, High-efficiency polycrystalline thin film tandem solar cells, *The journal of physical chemistry letters*, 6 (2015) 2676-2681.

[81] T. Todorov, T. Gershon, O. Gunawan, Y.S. Lee, C. Sturdevant, L.Y. Chang, S. Guha, Monolithic Perovskite - CIGS Tandem Solar Cells via In Situ Band Gap Engineering, *Adv Energy Mater*, 5 (2015).

[82] T. Todorov, T. Gershon, O. Gunawan, C. Sturdevant, S. Guha, Perovskite-kesterite monolithic tandem solar cells with high open-circuit voltage, *Appl Phys Lett*, 105 (2014) 173902.

[83] C.C. Chen, S.H. Bae, W.H. Chang, Z.R. Hong, G. Li, Q. Chen, H.P. Zhou, Y. Yang, Perovskite/polymer monolithic hybrid tandem solar cells utilizing a low-temperature, full solution process, *Mater Horiz*, 2 (2015) 203-211.

[84] Y. Liu, L.A. Renna, M. Bag, Z.A. Page, P. Kim, J. Choi, T. Emrick, D. Venkataraman, T.P. Russell, High Efficiency Tandem Thin-Perovskite/Polymer Solar Cells with a Graded Recombination Layer, *ACS applied materials & interfaces*, 8 (2016) 7070-7076.

[85] G.E. Eperon, T. Leijtens, K.A. Bush, R. Prasanna, T. Green, J.T.-W. Wang, D.P. McMeekin, G. Volonakis, R.L. Milot, R. May, Perovskite-perovskite tandem photovoltaics with optimized band gaps, *Science*, 354 (2016) 861-865.

[86] A. Rajagopal, Z. Yang, S.B. Jo, I.L. Braly, P.W. Liang, H.W. Hillhouse, A.K.Y. Jen, Highly Efficient Perovskite-Perovskite Tandem Solar Cells Reaching 80% of the Theoretical Limit in Photovoltage, *Adv Mater*, 29 (2017).

[87] D. Zhao, Y. Yu, C. Wang, W. Liao, N. Shrestha, C.R. Grice, A.J. Cimaroli, L. Guan, R.J. Ellingson, K. Zhu, Low-bandgap mixed tin-lead iodide perovskite absorbers with long carrier lifetimes for all-perovskite tandem solar cells, *Nat Energy*, 2 (2017) 17018.

[88] J.H. Heo, S.H. Im, $\text{CH}_3\text{NH}_3\text{PbBr}_3\text{-CH}_3\text{NH}_3\text{PbI}_3$ perovskite-perovskite tandem solar cells with exceeding 2.2 V open circuit voltage, *Adv Mater*, 28 (2016) 5121-5125.

[89] F. Jiang, T. Liu, B. Luo, J. Tong, F. Qin, S. Xiong, Z. Li, Y. Zhou, A two-terminal perovskite/perovskite tandem solar cell, *J Mater Chem A*, 4 (2016) 1208-1213.

[90] R. Sheng, M.T. Hörantner, Z. Wang, Y. Jiang, W. Zhang, A. Agosti, S. Huang, X. Hao, A. Ho-Baillie, M. Green, Monolithic Wide Band Gap Perovskite/Perovskite Tandem Solar Cells with Organic Recombination Layers, *The Journal of Physical Chemistry C*, 121 (2017) 27256-27262.

[91] A.D. Sheikh, A. Bera, M.A. Haque, R.B. Rakhi, S. Del Gobbo, H.N. Alshareef, T. Wu, Atmospheric effects on the photovoltaic performance of hybrid perovskite solar cells, *Sol*

Energ Mat Sol C, 137 (2015) 6-14.

[92] H. Wang, A.D. Sheikh, Q. Feng, F. Li, Y. Chen, W. Yu, E. Alarousu, C. Ma, M.A. Haque, D. Shi, Facile synthesis and high performance of a new carbazole-based hole-transporting material for hybrid perovskite solar cells, ACS Photonics, 2 (2015) 849-855.

[93] M.A. Haque, A.D. Sheikh, X. Guan, T. Wu, Metal oxides as efficient charge transporters in perovskite solar cells, Adv Energy Mater, (2017).

[94] J. Seo, S. Park, Y.C. Kim, N.J. Jeon, J.H. Noh, S.C. Yoon, S.I. Seok, Benefits of very thin PCBM and LiF layers for solution-processed p-i-n perovskite solar cells, Energ Environ Sci, 7 (2014) 2642-2646.

[95] F. Fu, T. Feurer, T.P. Weiss, S. Pisoni, E. Avancini, C. Andres, S. Buecheler, A.N. Tiwari, High-efficiency inverted semi-transparent planar perovskite solar cells in substrate configuration, Nat Energy, 2 (2017) 16190.

[96] M.A. Contreras, B. Egaas, K. Ramanathan, J. Hiltner, A. Swartzlander, F. Hasoon, R. Noufi, Progress toward 20% efficiency in Cu (In, Ga) Se₂ polycrystalline thin - film solar cells, Progress in Photovoltaics: Research and applications, 7 (1999) 311-316.

[97] K. Chopra, P. Paulson, V. Dutta, Thin - film solar cells: an overview, Progress in Photovoltaics: Research and Applications, 12 (2004) 69-92.

[98] W.H. Sun, Y.L. Li, S.Y. Ye, H.X. Rao, W.B. Yan, H.T. Peng, Y. Li, Z.W. Liu, S.F. Wang, Z.J. Chen, L.X. Xiao, Z.Q. Bian, C.H. Huang, High-performance inverted planar heterojunction perovskite solar cells based on a solution-processed CuO_x hole transport layer, Nanoscale, 8 (2016) 10806-10813.

[99] T. Dullweber, U. Rau, H. Schock, A new approach to high-efficiency solar cells by band gap grading in Cu (In, Ga) Se₂ chalcopyrite semiconductors, Sol Energ Mat Sol C, 67 (2001) 145-150.

[100] J.S. Wellings, A.P. Samantilleke, P. Warren, S.N. Heavens, I.M. Dharmadasa, Comparison of electrodeposited and sputtered intrinsic and aluminium-doped zinc oxide thin films, Semicond Sci Tech, 23 (2008).

[101] N. Naghavi, D. Abou-Ras, N. Allsop, N. Barreau, S. Bucheler, A. Ennaoui, C.H. Fischer, C. Guillen, D. Hariskos, J. Herrero, R. Klenk, K. Kushiya, D. Lincot, R. Menner, T. Nakada, C. Platzer-Bjorkman, S. Spiering, A.N. Tiwari, T. Torndahl, Buffer layers and transparent conducting oxides for chalcopyrite Cu(In,Ga)(S,Se)₂ based thin film photovoltaics: present status and current developments, Prog Photovoltaics, 18 (2010) 411-433.

[102] M.A. Green, A. Ho-Baillie, H.J. Snaith, The emergence of perovskite solar cells, Nat Photonics, 8 (2014) 506-514.

[103] Y. Wang, A. Steigert, G. Yin, V. Parvan, R. Klenk, R. Schlatmann, I. Laueremann, Cu₂O as a

Potential Intermediate Transparent Conducting Oxide Layer for Monolithic Perovskite - CIGSe Tandem Solar Cells, *physica status solidi (c)*, 14 (2017).

[104] G.C. Yin, A. Steigert, P. Manley, R. Klenk, M. Schmid, Enhanced absorption in tandem solar cells by applying hydrogenated In_2O_3 as electrode, *Appl Phys Lett*, 107 (2015).

[105] J. Werner, L. Barraud, A. Walter, M. Bräuninger, F. Sahli, D. Sacchetto, N. Tétreault, B. Paviet-Salomon, S.-J. Moon, C. Allebé, Efficient NIR-Transparent Perovskite Solar Cells Enabling Direct Comparison of 4-Terminal and Monolithic Perovskite/Silicon Tandem Cells, *ACS Energy Letters*, (2016).

[106] G.E. Eperon, T. Leijtens, K.A. Bush, R. Prasanna, T. Green, J.T.-W. Wang, D.P. McMeekin, G. Volonakis, R.L. Milot, R. May, Perovskite-perovskite tandem photovoltaics with optimized bandgaps, *Science*, (2016) aaf9717.

[107] K. Chopra, S. Major, D. Pandya, Transparent conductors—A status review, *Thin solid films*, 102 (1983) 1-46.

[108] S.S. Mali, C.K. Hong, pin/nip type planar hybrid structure of highly efficient perovskite solar cells towards improved air stability: synthetic strategies and the role of p-type hole transport layer (HTL) and n-type electron transport layer (ETL) metal oxides, *Nanoscale*, 8 (2016) 10528-10540.

[109] C.-C. Chueh, C.-Z. Li, A.K.-Y. Jen, Recent progress and perspective in solution-processed interfacial materials for efficient and stable polymer and organometal perovskite solar cells, *Energ Environ Sci*, 8 (2015) 1160-1189.

[110] Q. Xi, G. Gao, H. Zhou, Y. Zhao, C. Wu, L. Wang, P. Guo, J. Xu, Highly efficient inverted solar cells based on perovskite grown nanostructures mediated by CuSCN, *Nanoscale*, 9 (2017) 6136-6144.

[111] H. Zhang, H. Wang, W. Chen, A.K.Y. Jen, CuGaO_2 : A Promising Inorganic Hole - Transporting Material for Highly Efficient and Stable Perovskite Solar Cells, *Adv Mater*, 29 (2017).

[112] V. Shrotriya, G. Li, Y. Yao, C.-W. Chu, Y. Yang, Transition metal oxides as the buffer layer for polymer photovoltaic cells, *Appl Phys Lett*, 88 (2006) 073508.

[113] M. Buffiere, G. Brammertz, S. Sahayaraj, M. Batuk, S. Khelifi, D. Mangin, A.A. El Mel, L. Arzel, J. Hadermann, M. Meuris, J. Poortmans, KCN Chemical Etch for Interface Engineering in $\text{Cu}_2\text{ZnSnSe}_4$ Solar Cells, *ACS applied materials & interfaces*, 7 (2015) 14690-14698.

[114] M.A. Contreras, M.J. Romero, B. To, F. Hasoon, R. Noufi, S. Ward, K. Ramanathan, Optimization of CBD CdS process in high-efficiency Cu (In, Ga) Se_2 -based solar cells, *Thin Solid Films*, 403 (2002) 204-211.

[115] T. Minami, H. Nanto, S. Takata, Highly conductive and transparent aluminum doped

zinc oxide thin films prepared by RF magnetron sputtering, *Jpn J Appl Phys*, 23 (1984) L280.

[116] J.C. Lee, K.H. Kang, S.K. Kim, K.H. Yoon, I.J. Park, J. Song, RF sputter deposition of the high-quality intrinsic and n-type ZnO window layers for Cu (In, Ga) Se₂-based solar cell applications, *Sol Energ Mat Sol C*, 64 (2000) 185-195.

[117] K. Ramanathan, M.A. Contreras, C.L. Perkins, S. Asher, F.S. Hasoon, J. Keane, D. Young, M. Romero, W. Metzger, R. Noufi, Properties of 19.2% efficiency ZnO/CdS/CuInGaSe₂ thin - film solar cells, *Progress in Photovoltaics: research and applications*, 11 (2003) 225-230.

[118] C.T. Zuo, L.M. Ding, Solution-Processed Cu₂O and CuO as Hole Transport Materials for Efficient Perovskite Solar Cells, *Small*, 11 (2015) 5528-5532.

[119] I. Lauermann, A. Steigert, CISSY: A station for preparation and surface/interface analysis of thin film materials and devices, *Journal of large-scale research facilities JLSRF*, 2 (2016).

[120] V. Holy, J. Kubena, I. Ohli, K. Lischka, W. Plotz, X-ray reflection from rough layered systems, *Phys Rev B*, 47 (1993) 15896.

[121] L.G. Parratt, Surface studies of solids by total reflection of X-rays, *Physical review*, 95 (1954) 359.

[122] J. Chastain, R.C. King, J. Moulder, Handbook of X-ray photoelectron spectroscopy: a reference book of standard spectra for identification and interpretation of XPS data, Physical Electronics Division, Perkin-Elmer Corporation Eden Prairie, Minnesota, 1992.

[123] A. Einstein, Generation and conversion of light with regard to a heuristic point of view, *Annalen Der Physik*, 17 (1905) 132-148.

[124] M. Schmid,
http://www.helmholtz-berlin.de/forschung/oe/ee/archives/nanooptix/refdex/index_en.html
.

[125] M. Burgelman, Simulation programme SCAPS-1D for thin film solar cells developed at ELIS, University of Gent, <http://scaps.elis.ugent.be/>.

[126] M. Burgelman, P. Nollet, S. Degraeve, Modelling polycrystalline semiconductor solar cells, *Thin Solid Films*, 361 (2000) 527-532.

[127] S.F. K.K., http://www.solar-frontier.com/eng/news/2017/1220_press.html.

[128] F. Meillaud, A. Shah, C. Droz, E. Vallat-Sauvain, C. Miazza, Efficiency limits for single junction and tandem solar cells, *Sol Energ Mat Sol C*, 90 (2006) 2952-2959.

[129] H.P. Zhou, Q. Chen, G. Li, S. Luo, T.B. Song, H.S. Duan, Z.R. Hong, J.B. You, Y.S. Liu, Y. Yang, Interface engineering of highly efficient perovskite solar cells, *Science*, 345 (2014) 542-546.

- [130] M. Bar, W. Bohne, J. Rohrich, E. Strub, S. Lindner, M.C. Lux-Steiner, C.H. Fischer, T.P. Niesen, F. Karg, Determination of the band gap depth profile of the pentenary $\text{Cu}(\text{In}_{1-x}\text{Ga}_x)(\text{S}_y\text{Se}_{1-y})_2$ chalcopyrite from its composition gradient, *J Appl Phys*, 96 (2004) 3857-3860.
- [131] S. Ahn, T.H. Son, A. Cho, J. Gwak, J.H. Yun, K. Shin, S.K. Ahn, S.H. Park, K. Yoon, CuInSe_2 Thin-Film Solar Cells with 7.72% Efficiency Prepared via Direct Coating of a Metal Salts/Alcohol-Based Precursor Solution, *Chemoschem*, 5 (2012) 1773-1777.
- [132] Y. Oh, W. Yang, J. Kim, K. Woo, J. Moon, Aqueous Solution-Phase Selenized $\text{CuIn}(\text{S},\text{Se})_2$ Thin Film Solar Cells Annealed under Inert Atmosphere, *ACS applied materials & interfaces*, 7 (2015) 22570-22577.
- [133] O. Lundberg, M. Bodegård, J. Malmström, L. Stolt, Influence of the Cu (In, Ga) Se_2 thickness and Ga grading on solar cell performance, *Progress in Photovoltaics: Research and Applications*, 11 (2003) 77-88.
- [134] L. Kronik, D. Cahen, H.W. Schock, Effects of Sodium on Polycrystalline $\text{Cu}(\text{In},\text{Ga})\text{Se}_2$ and Its Solar Cell Performance, *Adv Mater*, 10 (1998) 31-36.
- [135] N. Tokio, I. Daisuke, O. Hiroki, K. Akio, Effects of Sodium on $\text{Cu}(\text{In}, \text{Ga})\text{Se}_2$ -Based Thin Films and Solar Cells, *Jpn J Appl Phys*, 36 (1997) 732.
- [136] P.T. Erslev, J.W. Lee, W.N. Shafarman, J.D. Cohen, The influence of Na on metastable defect kinetics in CIGS materials, *Thin Solid Films*, 517 (2009) 2277-2281.
- [137] A. Rockett, The effect of Na in polycrystalline and epitaxial single-crystal $\text{CuIn}_{1-x}\text{Ga}_x\text{Se}_2$, *Thin Solid Films*, 480-481 (2005) 2-7.
- [138] D. Rudmann, D. Brémaud, A.F. da Cunha, G. Bilger, A. Strohm, M. Kaelin, H. Zogg, A.N. Tiwari, Sodium incorporation strategies for CIGS growth at different temperatures, *Thin Solid Films*, 480-481 (2005) 55-60.
- [139] D. Lincot, J.-F. Guillemoles, S. Taunier, D. Guimard, J. Sicx-Kurdi, A. Chaumont, O. Roussel, O. Ramdani, C. Hubert, J. Fauvarque, Chalcopyrite thin film solar cells by electrodeposition, *Sol Energy*, 77 (2004) 725-737.
- [140] S. Pillai, K. Catchpole, T. Trupke, M. Green, Surface plasmon enhanced silicon solar cells, *J Appl Phys*, 101 (2007) 093105.
- [141] M.A. Green, *Solar cells: operating principles, technology, and system applications*, Englewood Cliffs, NJ, Prentice-Hall, Inc., 1982. 288 p., (1982).
- [142] P. Jackson, R. Wuerz, D. Hariskos, E. Lotter, W. Witte, M. Powalla, Effects of heavy alkali elements in $\text{Cu}(\text{In},\text{Ga})\text{Se}_2$ solar cells with efficiencies up to 22.6%, *Phys Status Solidi-R*, 10 (2016) 583-586.

- [143] I. Repins, M.A. Contreras, B. Egaas, C. DeHart, J. Scharf, C.L. Perkins, B. To, R. Noufi, 19.9%-efficient ZnO/CdS/CuInGaSe₂ solar cell with 81.2% fill factor, *Prog Photovoltaics*, 16 (2008) 235-239.
- [144] M. Saliba, T. Matsui, J.Y. Seo, K. Domanski, J.P. Correa-Baena, M.K. Nazeeruddin, S.M. Zakeeruddin, W. Tress, A. Abate, A. Hagfeldt, M. Gratzel, Cesium-containing triple cation perovskite solar cells: improved stability, reproducibility and high efficiency, *Energy Environ Sci*, 9 (2016) 1989-1997.
- [145] M.A. Green, K. Emery, Y. Hishikawa, W. Warta, E.D. Dunlop, Solar cell efficiency tables (version 46), *Prog Photovoltaics*, 23 (2015) 805-812.
- [146] S.S. Shin, E.J. Yeom, W.S. Yang, S. Hur, M.G. Kim, J. Im, J. Seo, J.H. Noh, S. Il Seok, Colloidally prepared La-doped BaSnO₃ electrodes for efficient, photostable perovskite solar cells, *Science*, 356 (2017) 167-171.
- [147] A. Roos, T. Chibuye, B. Karlsson, Properties of Oxidized Copper Surfaces for Solar Applications .1., *Sol Energ Mater*, 7 (1983) 453-465.
- [148] J. Ghijsen, L.H. Tjeng, J. Vanelp, H. Eskes, J. Westerink, G.A. Sawatzky, M.T. Czyzyk, Electronic-Structure of Cu₂O and CuO, *Phys Rev B*, 38 (1988) 11322-11330.
- [149] K. Matsuzaki, K. Nomura, H. Yanagi, T. Kamiya, M. Hirano, H. Hosono, Epitaxial growth of high mobility Cu₂O thin films and application to p-channel thin film transistor, *Appl Phys Lett*, 93 (2008).
- [150] W.B. Yan, S.Y. Ye, Y.L. Li, W.H. Sun, H.X. Rao, Z.W. Liu, Z.Q. Bian, C. Huang, Hole-Transporting Materials in Inverted Planar Perovskite Solar Cells, *Adv Energy Mater*, 6 (2016).
- [151] H. Rao, S. Ye, W. Sun, W. Yan, Y. Li, H. Peng, Z. Liu, Z. Bian, Y. Li, C. Huang, A 19.0% efficiency achieved in CuO_x-based inverted CH₃NH₃PbI_{3-x}Cl_x solar cells by an effective Cl doping method, *Nano Energy*, 27 (2016) 51-57.
- [152] B.A. Nejad, V. Ahmadi, S. Gharibzadeh, H.R. Shahverdi, Cuprous Oxide as a Potential Low-Cost Hole-Transport Material for Stable Perovskite Solar Cells, *Chemsuschem*, 9 (2016) 302-313.
- [153] M.I. Hossain, F.H. Alharbi, N. Tabet, Copper oxide as inorganic hole transport material for lead halide perovskite based solar cells, *Sol Energy*, 120 (2015) 370-380.
- [154] F.M. Li, R. Waddingham, W.I. Milne, A.J. Flewitt, S. Speakman, J. Dutson, S. Wakeham, M. Thwaites, Low temperature (< 100° C) deposited P-type cuprous oxide thin films: Importance of controlled oxygen and deposition energy, *Thin Solid Films*, 520 (2011) 1278-1284.
- [155] C. Malerba, F. Biccari, C.L.A. Ricardo, M. D'Incau, P. Scardi, A. Mittiga, Absorption

coefficient of bulk and thin film Cu_2O , *Sol Energ Mat Sol C*, 95 (2011) 2848-2854.

[156] P. Loper, M. Stuckelberger, B. Niesen, J. Werner, M. Filipic, S.J. Moon, J.H. Yum, M. Topic, S. De Wolf, C. Ballif, Complex Refractive Index Spectra of $\text{CH}_3\text{NH}_3\text{PbI}_3$ Perovskite Thin Films Determined by Spectroscopic Ellipsometry and Spectrophotometry, *J Phys Chem Lett*, 6 (2015) 66-71.

[157] G.Z. Lai, Y.W. Wu, L.M. Lin, Y. Qu, F.C. Lai, OPTICAL PROPERTIES OF N-DOPED Cu_2O THIN FILMS DEPOSITED BY RF-MAGNETRON SPUTTERING Cu_2O TARGET, *Surf Rev Lett*, 21 (2014).

[158] H.J. Li, C.Y. Pu, C.Y. Ma, S. Li, W.J. Dong, S.Y. Bao, Q.Y. Zhang, Growth behavior and optical properties of N-doped Cu_2O films, *Thin Solid Films*, 520 (2011) 212-216.

[159] R. Asahi, T. Morikawa, T. Ohwaki, K. Aoki, Y. Taga, Visible-light photocatalysis in nitrogen-doped titanium oxides, *Science*, 293 (2001) 269-271.

[160] G.Z. Lai, Y.W. Wu, L.M. Lin, Y. Qu, F.C. Lai, Low resistivity of N-doped Cu_2O thin films deposited by rf-magnetron sputtering, *Appl Surf Sci*, 285 (2013) 755-758.

[161] T. Dullweber, U. Rau, H. Schock, A new approach to high-efficiency solar cells by band gap grading in Cu (In, Ga) Se_2 chalcopyrite semiconductors, *Sol Energ Mat Sol C*, 67 (2001) 145-150.

[162] J. Seo, S. Park, Y.C. Kim, N.J. Jeon, J.H. Noh, S.C. Yoon, S.I. Sang, Benefits of very thin PCBM and LiF layers for solution-processed p-i-n perovskite solar cells, *Energ Environ Sci*, 7 (2014) 2642-2646.

[163] H. Zhang, J.Q. Cheng, F. Lin, H.X. He, J. Mao, K.S. Wong, A.K.Y. Jen, W.C.H. Choy, Pinhole-Free and Surface-Nanostructured NiO_x Film by Room-Temperature Solution Process for High-Performance Flexible Perovskite Solar Cells with Good Stability and Reproducibility, *Acs Nano*, 10 (2016) 1503-1511.

[164] P. Kelly, R. Arnell, Magnetron sputtering: a review of recent developments and applications, *Vacuum*, 56 (2000) 159-172.

[165] W.D. Sproul, K.O. Legg, Opportunities for innovation: advanced surface engineering, Technomic Publishing Company, 1995.

[166] X. Nie, S.-H. Wei, S. Zhang, Bipolar doping and band-gap anomalies in delafossite transparent conductive oxides, *Phys Rev Lett*, 88 (2002) 066405.

[167] R. Gillen, J. Robertson, Band structure calculations of CuAlO_2 , CuGaO_2 , CuInO_2 , and CuCrO_2 by screened exchange, *Phys Rev B*, 84 (2011) 035125.

[168] M. Yu, T.I. Draskovic, Y. Wu, Understanding the crystallization mechanism of delafossite CuGaO_2 for controlled hydrothermal synthesis of nanoparticles and nanoplates, *Inorg Chem*, 53 (2014) 5845-5851.

- [169] J. Bandara, J. Yasomanee, P-type oxide semiconductors as hole collectors in dye-sensitized solid-state solar cells, *Semicond Sci Tech*, 22 (2006) 20.
- [170] A. Nattestad, X. Zhang, U. Bach, Y.-B. Cheng, Dye-sensitized CuAlO₂ photocathodes for tandem solar cell applications, *Journal of Photonics for Energy*, 1 (2011) 011103-011103-011109.
- [171] M.Z. Yu, G. Natu, Z.Q. Ji, Y.Y. Wu, p-Type Dye-Sensitized Solar Cells Based on Delafossite CuGaO₂ Nanoplates with Saturation Photovoltages Exceeding 460 mV, *J Phys Chem Lett*, 3 (2012) 1074-1078.
- [172] A. Renaud, B. Chavillon, L. Le Pleux, Y. Pellegrin, E. Blart, M. Boujtita, T. Pauporte, L. Cario, S. Jobic, F. Odobel, CuGaO₂: a promising alternative for NiO in p-type dye solar cells, *J Mater Chem*, 22 (2012) 14353-14356.
- [173] D. Xiong, Z. Xu, X. Zeng, W. Zhang, W. Chen, X. Xu, M. Wang, Y.-B. Cheng, Hydrothermal synthesis of ultrasmall CuCrO₂ nanocrystal alternatives to NiO nanoparticles in efficient p-type dye-sensitized solar cells, *J Mater Chem*, 22 (2012) 24760-24768.
- [174] X. Xu, B. Zhang, J. Cui, D. Xiong, Y. Shen, W. Chen, L. Sun, Y. Cheng, M. Wang, Efficient p-type dye-sensitized solar cells based on disulfide/thiolate electrolytes, *Nanoscale*, 5 (2013) 7963-7969.
- [175] Z. Xu, D.H. Xiong, H. Wang, W.J. Zhang, X.W. Zeng, L.Q. Ming, W. Chen, X.B. Xu, J. Cui, M.K. Wang, S. Powar, U. Bach, Y.B. Cheng, Remarkable photocurrent of p-type dye-sensitized solar cell achieved by size controlled CuGaO₂ nanoplates, *J Mater Chem A*, 2 (2014) 2968-2976.
- [176] W.C. Sheets, E. Mugnier, A. Barnabé, T.J. Marks, K.R. Poeppelmeier, Hydrothermal synthesis of delafossite-type oxides, *Chem Mater*, 18 (2006) 7-20.
- [177] M.Z. Yu, T.I. Draskovic, Y.Y. Wu, Cu(I)-based delafossite compounds as photocathodes in p-type dye-sensitized solar cells, *Phys Chem Chem Phys*, 16 (2014) 5026-5033.
- [178] J. Pellicer-Porres, A. Segura, C. Ferrer-Roca, A. Polian, P. Munsch, D. Kim, XRD and XAS structural study of CuAlO₂ under high pressure, *Journal of Physics: Condensed Matter*, 25 (2013) 115406.
- [179] J. Wang, V. Ibarra, D. Barrera, L. Xu, Y.J. Lee, J.L.W.P. Hsu, Solution Synthesized p-Type Copper Gallium Oxide Nanoplates as Hole Transport Layer for Organic Photovoltaic Devices, *J Phys Chem Lett*, 6 (2015) 1071-1075.
- [180] G. Xing, N. Mathews, S. Sun, S.S. Lim, Y.M. Lam, M. Grätzel, S. Mhaisalkar, T.C. Sum, Long-range balanced electron-and hole-transport lengths in organic-inorganic CH₃NH₃PbI₃, *Science*, 342 (2013) 344-347.
- [181] C. Wagner, W. Riggs, L. Davis, J. Moulder, G. Muilenberg, *Handbook of X-ray*

Photoelectron Spectroscopy, Perkin-Elmer, Corporation Physical Electronics Division, Eden Prairie, Minnesota, USA, 472 (1979).

[182] G. Schön, Auger and direct electron spectra in X-ray photoelectron studies of zinc, zinc oxide, gallium and gallium oxide, *Journal of Electron Spectroscopy and Related Phenomena*, 2 (1973) 75-86.

[183] M. Han, K. Jiang, J. Zhang, W. Yu, Y. Li, Z. Hu, J. Chu, Structural, electronic band transition and optoelectronic properties of delafossite $\text{CuGa}_{1-x}\text{Cr}_x\text{O}_2$ ($0 \leq x \leq 1$) solid solution films grown by the sol-gel method, *J Mater Chem*, 22 (2012) 18463-18470.

[184] F. Zhi-Jie, F. Cheng, S. Li-Jie, L. Yong-Hui, H. Man-Chao, First-principles study of defects in CuGaO_2 , *Chinese Physics Letters*, 25 (2008) 2997.

[185] S. Jeong, J. Boo, Influence of target-to-substrate distance on the properties of AZO films grown by RF magnetron sputtering, *Thin Solid Films*, 447 (2004) 105-110.

[186] J.G. Jolley, G.G. Geesey, M.R. Hankins, R.B. Wright, P.L. Wichlacz, Auger electron and X-ray photoelectron spectroscopic study of the biocorrosion of copper by alginic acid polysaccharide, *Appl Surf Sci*, 37 (1989) 469-480.

[187] G. Cossu, G.M. Ingo, G. Mattocono, G. Padeletti, G. Proietti, XPS investigation on vacuum thermal desorption of UV/ozone treated GaAs (100) surfaces, *Appl Surf Sci*, 56 (1992) 81-88.

[188] N. McIntyre, M. Cook, X-ray photoelectron studies on some oxides and hydroxides of cobalt, nickel, and copper, *Analytical chemistry*, 47 (1975) 2208-2213.

[189] A. Barrie, F. Street, An Auger and X-ray photoelectron spectroscopic study of sodium metal and sodium oxide, *Journal of Electron Spectroscopy and Related Phenomena*, 7 (1975) 1-31.

[190] I. Herraiz-Cardona, F. Fabregat-Santiago, A. Renaud, B. Julián-López, F. Odobel, L. Cario, S. Jobic, S. Giménez, Hole conductivity and acceptor density of p-type CuGaO_2 nanoparticles determined by impedance spectroscopy: the effect of Mg doping, *Electrochim Acta*, 113 (2013) 570-574.

[191] A.I. Renaud, L. Cario, P. Deniard, E. Gautron, X. Rocquefelte, Y. Pellegrin, E. Blart, F. Odobel, S.p. Jobic, Impact of Mg doping on performances of CuGaO_2 based p-type dye-sensitized solar cells, *The Journal of Physical Chemistry C*, 118 (2013) 54-59.

[192] T. Minemoto, M. Murata, Theoretical analysis on effect of band offsets in perovskite solar cells, *Sol Energ Mat Sol C*, 133 (2015) 8-14.

[193] K. Jäger, L. Korte, B. Rech, S. Albrecht, Numerical optical optimization of monolithic planar perovskite-silicon tandem solar cells with regular and inverted device architectures, *Optics Express*, 25 (2017) A473-A482.

- [194] P.A. Basore, Numerical modeling of textured silicon solar cells using PC-1D, IEEE Transactions on electron devices, 37 (1990) 337-343.
- [195] A. Niemegeers, M. Burgelman, Effects of the Au/CdTe back contact on IV and CV characteristics of Au/CdTe/CdS/TCO solar cells, J Appl Phys, 81 (1997) 2881-2886.
- [196] P. Nollet, M. Köntges, M. Burgelman, S. Degraeve, R. Reineke-Koch, Indications for presence and importance of interface states in CdTe/CdS solar cells, Thin Solid Films, 431 (2003) 414-420.
- [197] T. Dullweber, O. Lundberg, J. Malmström, M. Bodegård, L. Stolt, U. Rau, H.-W. Schock, J.H. Werner, Back surface band gap gradings in Cu (In, Ga) Se₂ solar cells, Thin Solid Films, 387 (2001) 11-13.
- [198] M. Murata, D. Hironiwa, N. Ashida, J. Chantana, K. Aoyagi, N. Kataoka, T. Minemoto, Optimum bandgap profile analysis of Cu (In, Ga) Se₂ solar cells with various defect densities by SCAPS, Jpn J Appl Phys, 53 (2014) 04ER14.
- [199] G. Yin, C. Merschjann, M. Schmid, The effect of surface roughness on the determination of optical constants of CuInSe₂ and CuGaSe₂ thin films, J Appl Phys, 113 (2013).
- [200] M. Campoy-Quiles, C. Muller, M. Garriga, E. Wang, O. Inganäs, M.I. Alonso, On the complex refractive index of polymer:fullerene photovoltaic blends, Thin Solid Films, 571 (2014) 371-376.
- [201] P. Jackson, D. Hariskos, R. Wuerz, O. Kiowski, A. Bauer, T.M. Friedlmeier, M. Powalla, Properties of Cu (In, Ga) Se₂ solar cells with new record efficiencies up to 21.7%, physica status solidi (RRL)-Rapid Research Letters, 9 (2015) 28-31.
- [202] G. Wetzelaer, M. Kuik, M. Lenes, P. Blom, Origin of the dark-current ideality factor in polymer: fullerene bulk heterojunction solar cells, Appl Phys Lett, 99 (2011) 153506.
- [203] M. Burgelman, K. Decock, A. Niemegeers, J. Verschraegen, S. Degraeve, SCAPS manual, in, February, 2016.
- [204] U. Mandadapu, S.V. Vedanayakam, K. Thyagarajan, Simulation and Analysis of Lead based Perovskite Solar Cell using SCAPS-1D, Indian Journal of Science and Technology, 10 (2017).
- [205] E. Karimi, S. Ghorashi, Investigation of the influence of different hole-transporting materials on the performance of perovskite solar cells, Optik-International Journal for Light and Electron Optics, 130 (2017) 650-658.
- [206] K.A. Nagamatsu, S. Avasthi, J. Jhaveri, J.C. Sturm, A 12% efficient silicon/PEDOT: PSS heterojunction solar cell fabricated at < 100 C, IEEE J Photovolt, 4 (2014) 260-264.

- [207] J.-Y. Jeng, Y.-F. Chiang, M.-H. Lee, S.-R. Peng, T.-F. Guo, P. Chen, T.-C. Wen, Methylammonium lead iodide perovskite/fullerene-based hybrid solar cells, SPIE Newsroom, 10 (2014) 005033.
- [208] L. Zhu, G. Shao, J. Luo, Numerical study of metal oxide heterojunction solar cells, *Semicond Sci Tech*, 26 (2011) 085026.
- [209] G. Giorgi, J.-I. Fujisawa, H. Segawa, K. Yamashita, Small photocarrier effective masses featuring ambipolar transport in methylammonium lead iodide perovskite: A density functional analysis, *The journal of physical chemistry letters*, 4 (2013) 4213-4216.
- [210] K. Akaike, K. Kanai, H. Yoshida, J.y. Tsutsumi, T. Nishi, N. Sato, Y. Ouchi, K. Seki, Ultraviolet photoelectron spectroscopy and inverse photoemission spectroscopy of [6, 6]-phenyl-C 61-butylric acid methyl ester in gas and solid phases, *J Appl Phys*, 104 (2008) 023710.
- [211] P.A. Korzhavyi, B. Johansson, Literature review on the properties of cuprous oxide Cu_2O and the process of copper oxidation, Swedish Nuclear Fuel and Waste Management Company, 2011.
- [212] C. Wehrenfennig, G.E. Eperon, M.B. Johnston, H.J. Snaith, L.M. Herz, High charge carrier mobilities and lifetimes in organolead trihalide perovskites, *Adv Mater*, 26 (2014) 1584-1589.
- [213] H. Matsumura, A. Fujii, T. Kitatani, Properties of high-mobility Cu_2O films prepared by thermal oxidation of Cu at low temperatures, *Jpn J Appl Phys*, 35 (1996) 5631.
- [214] Q. Zhou, D. Jiao, K. Fu, X. Wu, Y. Chen, J. Lu, S.-e. Yang, Two-dimensional device modeling of $\text{CH}_3\text{NH}_3\text{PbI}_3$ based planar heterojunction perovskite solar cells, *Sol Energy*, 123 (2016) 51-56.
- [215] Y.S. Lee, J. Heo, M.T. Winkler, S.C. Siah, S.B. Kim, R.G. Gordon, T. Buonassisi, Nitrogen-doped cuprous oxide as a p-type hole-transporting layer in thin-film solar cells, *J Mater Chem A*, 1 (2013) 15416-15422.
- [216] S.H. Lee, S.J. Yun, J.W. Lim, The Characteristics of Cu_2O Thin Films Deposited Using RF-Magnetron Sputtering Method with Nitrogen-Ambient, *Etri Journal*, 35 (2013) 1156-1159.
- [217] B. Li, L. Lin, H. Shen, F. Boafu, Z. Chen, B. Liu, R. Zhang, Effect of N doping on hole density of Cu_2O : N films prepared by the reactive magnetron sputtering method, *The European Physical Journal-Applied Physics*, 58 (2012).
- [218] J.M. Ball, M.M. Lee, A. Hey, H.J. Snaith, Low-temperature processed meso-superstructured to thin-film perovskite solar cells, *Energ Environ Sci*, 6 (2013) 1739-1743.
- [219] H.J. Snaith, N.C. Greenham, R.H. Friend, The Origin of Collected Charge and Open -

Circuit Voltage in Blended Polyfluorene Photovoltaic Devices, *Adv Mater*, 16 (2004) 1640-1645.

[220] U. Mandapū, S.V. Vedanayakam, K. Thyagarajan, Numerical Simulation of $\text{CH}_3\text{NH}_3\text{PbI}_{3-x}\text{Cl}_x$ Perovskite solar cell using SCAPS-1D.

List of publications

PUBLICATIONS

1. **Wang, Y.**, Wenisch, R., Schlatmann, R., & Lauermann, I. (2018). Inorganic Materials as Hole Selective Contacts and Intermediate Tunnel Junction Layer for Monolithic Perovskite-CIGSe Tandem Solar Cells. *Advanced Energy Materials*, 8(30), 1801692.
2. Ren, J., Weber, F., Weigert, F., **Wang, Y.**, Choudhury, S., Xiao, J., Lauermann, I., Resch-Genger, U., Bande, A., & Petit, T. (2019). Effect of surface chemistry on optical, chemical and electronic properties of blue luminescent carbon dots. *Nanoscale*.
3. **Wang, Y.**, Steigert, A., Yin, G., Parvan, V., Klenk, R., Schlatmann, R., & Lauermann, I. (2017). Cu₂O as a Potential Intermediate Transparent Conducting Oxide Layer for Monolithic Perovskite-CIGSe Tandem Solar Cells. *physica status solidi (c)*, 14(10).
4. **Wang, Y.**, Lin, X., Wang, L., Köhler, T., Lux-Steiner, M. C., & Klenk, R. (2017). Low band-gap CuIn (S, Se)₂ thin film solar cells using molecular ink with 9.5% efficiency. *physica status solidi (c)*, 14(6).

PRESENTATION

1. **Wang, Y.**, Lin, X., Wang, L., Köhler, T., Lux-Steiner, M. C., & Klenk, R. Low band gap CuIn(S,Se)₂ thin film solar cells prepared using a stable molecular ink. Poster session, 20th International Conference on Ternary and Multinary Compounds (ICTMC 20), Halle (Saale), Germany. 2016.
2. **Wang, Y.**, Steigert, A., Yin, G., Parvan, V., Klenk, R., Schlatmann, R., & Lauermann, I. Cu₂O as a potential intermediate transparent conducting oxide layer for perovskite-CIGSe Tandem Solar Cells. Poster session, E-MRS Spring meeting, Strasbourg, France. 2017.

Acknowledgements

I would like to acknowledge all of those who helped and contributed to my work and during the writing of this thesis:

- Dr. Iver Lauermann, as my research supervisor, for accepting me in the CISSY group, for his patient guidance, consistent and illuminating instruction on my experiments, for his instructive suggestions and valuable comments on the writing of this thesis. Without his insightful criticism and expert guidance, I cannot continue my PhD study and finish this thesis.
- Prof. Dr. rer. nat. Bernd Szyszka, as my first supervisor, for giving me the opportunity to perform my thesis at his department at the Technische Universität Berlin as a PhD student, for his instructive advice and useful suggestions on my thesis. I am deeply grateful of his help in the completion of this thesis.
- Prof. Dr. Rutger Schlatmann, as my second supervisor and the head of PVcomB institute, for accepting me continuing my experimental work in his institute and offering me such a potential research topic in a major project, for providing me with valuable advice and suggestions on my thesis.
- Dr. Reiner Klenk, for introducing me into the chalcopyrite thin film solar cells field and explaining all the basic knowledge to me who was a beginner in this field every Tuesday of my first year, for teaching me electrical simulation by SCAPS. And Dr. Christian Kaufmann, for giving me suggestions about work, project, and life, for many times useful discussions and inspiring advice.
- The current and the former colleagues of the CISSY group and EE-IH institute: Dr. Robert Wensch, Dr. Natalia Maticiuc, Isheta Majumdar, Binoy Chacko, Alexander Steigert, Dr. Tetiana Olar, Dr. Vladimir Parvan, Dr. Xianzhong Lin, Lan Wang, Tristan Köhler, Dr. Guanchao Yin, Carola Ferber, Michael Kirsch, Jürgen Albert, and Qin Tan for creating a pleasant work atmosphere and all their contributions to my work. Especially Dr. Robert Wensch, for working with me for a long time to prepare samples and for the fruitful discussions many times, even helping me analyzing XPS data and figures.
- Chinese Scholarship Council (CSC) for the financial support during my PhD.
- My parents, my husband Peng Xu, for their continuous support and unlimited love.
- Last but not least my baby Yibo (Lukas) Xu, for his constant companion without any complaint, for obediently staying in my belly and growing up healthily during my entire pregnancy. This thesis is our first joint work, Lukas. Mom loves you.

